Université Paris-Saclay
Università degli studi dell'insubria
Prepared at Université Paris-Sud
École Doctorale n°576 PHENIICS
Particules hadrons energie et noyau : instrumentation, image, cosmos et simulation

Doctoral Thesis in Particle Physics

Development and optimization of scintillating bolometers and innovative light detectors for the search for neutrinoless double beta decay

Author:
Michele Mancuso

Supervisor:
Dr. Andrea Giuliani
Prof. Michela Prest

Condensed matter Physics Group
Centre de Sciences Nucléaires et de Sciences de la Matière (CSNSM)

Orsay - 25 February 2016

Committee:

M. Laurent TASSAN GOT - Institut de Physique Nucléaire Orsay, Research Director - President

M. Andrea GIULIANI - CSNSM, Research Director - Supervisor

Mme Michela PREST - Università degli studi dell'Insubria, Professor - Supervisor

M. Alessandro MONFARDINI - Institut Neel, Researcher - Referee

M. Fabio BELLINI - Sapienza Università di Roma, Professor - Referee

M. Massimo CACCIA - Università degli studi dell'Insubria, Professor

NNT:2016SACLS083

Université Paris-Saclay
Università degli studi dell'insubria

Abstract

Particules, Hadrons, Energie et Noyau: Instrumentation, Imagerie, Cosmos et Simulation (PHENIICS)
Centre de Sciences Nucléaires et de Sciences de la Matière (CSNSM)

Doctor of Philosophy

Development and optimization of scintillating bolometers and innovative light detectors for the search for neutrinoless double beta decay

by Michele Mancuso

Key words: Particle physics, neutrinoless double beta decay, bolometric detectors, instrumentation, Cryogenics.

The PhD work described in this manuscript was performed in the framework of the LUMINEU project, a pilot search for the neutrinoless double beta decay ($0\nu\beta\beta$) of the isotope in ^{100}Mo with $ZnMoO_4$ scintillating bolometers. The main PhD activity has consisted the development of a particle detection technology able to fulfill the requirement of a next generation experiment on $0\nu\beta\beta$ capable of exploring the inverted hierarchy region of the neutrino mass pattern. We report about an experimental physics work involving progress in detector prototype design and tests, and development of tools in view of a large experiment preparation.
The neutrinoless double beta decay is a hypothetical rare nuclear transition with a half life $T_{\frac{1}{2}}>10^{25}$ years, which is possible for some nuclei with an even number both of protons and neutrons. In the $0\nu\beta\beta$ transition two neutrons decay simultaneously in two protons with the emission of only two electrons. In a first approximation it can be seen as two simultaneous β-decays where the two neutrinos act as a single virtual particle joining the two decay vertices. It is demonstrated that any process which leads to $0\nu\beta\beta$ is possible only if $\nu \equiv \bar{\nu}$, i.e. the neutrino is a Majorana particle, which is in contrast with the Standard Model assumptions. Therefore, the observation of this phenomenon can determine the Majorana nature of massive neutrinos. This is of fundamental importance to make progress in our understanding of the origin of neutrino masses and mixing and of the symmetries governing the lepton sector of particle interactions. The measurement of the $T_{\frac{1}{2}}$ of the process would give unvaluable information on the absolute scale of neutrino masses, the type of neutrino mass spectrum and the Majorana phases. The detection approach adopted in this thesis is the homogeneous bolometric technique, which fits well the detector characteristics needed to investigate rare events. The detector provides high efficiency and a very good energy resolution and, thanks to a scintillating absorber, it allows particle discrimination for background suppression. As can be easily understood, the control of the background is crucial to measure such rare decays.
The first part of this thesis focuses on the neutrino physics and on the $0\nu\beta\beta$ decay; moreover the experimental detection approaches are briefly discussed and the sensitivity to

the half life of a $0\nu\beta\beta$ experiment is discussed. To understand the progress achieved in the technology development, the following chapter is dedicated to the detector physics: the components of a bolometer, a simple thermal model, and the detector response are introduced.
The second part of this work is dedicated to the setup. The detectors used work at very low temperatures ($\sim$10 mK), thus sophisticated thermal machines are needed; the working principles of these cryogenic systems are presented focusing on the details of the ones used in this work. Since the experimental work discussed in this thesis concerns the detector assembly and measurement, the data acquisition and analysis are discussed in details too.
The final part of the thesis is devoted to the results, starting with the progress made on bolometric light detectors: a description and optimization of the light detector design, the effect of anti-reflective coating and the thermal response enhancement obtained with the Neganov-Luke effect are presented. The results on the development of the LUMINEU prototype detectors and the measurements are summarized, from the working tests to the radioactive contaminant measurements. The growth and purification process of the $ZnMoO_4$ crystals are also presented. Based on these results, a final sensitivity of a future experiment based on this detector is computed.
Finally we present a spin-off of the LUMINEU project consisting in a scintillating bolometer prototype made with an alternative compound absorber, Li_2MoO_4. We examine the advantages and disadvantages with respect to the $ZnMoO_4$.
This manuscript aims at being a guide to an experimental approach for the search for neutrinoless double beta decay, a manual for scintillating bolometer operations and a report about the successful LUMINEU project.

Université Paris-Saclay
Università degli studi dell'insubria

Résumé

Particules, Hadrons, Energie et Noyau: Instrumentation, Imagerie, Cosmos et Simulation (PHENIICS)
Centre de Sciences Nucléaires et de Sciences de la Matière (CSNSM)

Doctor of Philosophy

Développement et optimisation de détecteurs de lumière innovants et bolométres scintillants pour une expérience pilote sur la double désintégration bêta sans émission de neutrinos

by Michele Mancuso

Mots-clés: Physique des particules, double désintégration bêta sans émission de neutrinos, detecteurs, instrumentations, cryogénie.

Le travail de doctorat exposé dans ce manuscrit a été développé dans le cadre du projet LUMINEU, une expérience pilote pour la double désintégration bêta sans émission de neutrinos ($0\nu\beta\beta$) de l'isotope ^{100}Mo avec des bolomètres scintillants de $ZnMoO_4$. L'activité principale du doctorat consistait en le développement d'une technologie de détection de particules capable de satisfaire les conditions nécessaire d'une expérience de $0\nu\beta\beta$ de nouvelle génération qui soit capable d'examiner la région de la hiérarchie inversée du modèle de la masse du neutrino. Nous exposons un travail de physique expérimentale qui implique l'avancement du design et des tests des prototypes de détecteurs, et le développement des outils en vue de la préparation d'une expérience importante.
La double désintégration bêta sans émission de neutrinos est une hypothétique transition nucléaire rare avec une demi-vie de $T_{\frac{1}{2}}>10^{25}$ ans, qui est possible pour certains noyaux avec un nombre pair de protons et de neutrons. Dans la transition $0\nu\beta\beta$ deux neutrons se désintègrent simultanément en deux protons avec l'émission de deux électrons seulement. Dans une première approximation, ce peut être vu comme deux β désintégrations où les deux neutrinos agissent comme une seule particule virtuelle en joignant les deux sommets de désintégration. Il est prouvé que n'importe quel processus qui conduit au $0\nu\beta\beta$ est possible seulement si $\nu \equiv \bar{\nu}$, v.g. le neutrino est une particule de Majorana, qui contraste avec les hypothèses du Modèle Standard. Par conséquence, l'observation de ce phénomène peut déterminer la nature Majorana des neutrinos massifs. C'est très important de faire progresser notre compréhension de l'origine de la masse et de la composition des neutrinos et de la symétrie qui régit le secteur des leptons des interactions de particules.
La mesure du $T_{\frac{1}{2}}$ du processus peut fournir des informations inestimables sur l'échelle absolue de la masse des neutrinos, sur le type de spectre de masse des neutrinos et sur les phases de Majorana. La méthode de détection adoptée dans cette thèse est la technique bolométrique, qui s'intègre bien avec les caractéristiques requises des détecteurs pour étudier les événements rares. Le détecteur fournit une grande efficacité et une très

bonne résolution en énergie et, grâce à un absorbeur scintillant, il permet la discrimination des particules pour la suppression du fond. Comme on peut bien comprendre, le contrôle du background est crucial pour mesurer ces désintégrations rares.
La première partie de cette thèse se concentre sur la physique du neutrino et sur la désintégration $0\nu\beta\beta$; en outre, les méthodes de détection expérimentales et la sensibilité de la demi-vie d'une expérience $0\nu\beta\beta$ sont traitées. Pour comprendre les progrès réalisés dans le développement de la technologie, le chapitre suivant est dédié à la physique des détecteurs: les composants d'un bolomètre, un modèle thermique simple, et la réponse d'un détecteur sont présentés.
La deuxième partie de ce travail est dédiée au setup. Les détecteurs utilisés fonctionnent aux très basses températures ($\sim$10 mK), par conséquent, des machines thermique sophistiquées sont nécessaires; les principes de fonctionnement de ces systèmes cryogéniques sont présentés en se concentrant sur les détails de ceux qui ont été utilisés dans ce travail. Puisque l'activité expérimentale présentée dans cette thèse porte sur l'assemblage et sur les mesures du détecteur, aussi l'acquisition et l'analyse des données sont traités en détails.
La dernière partie de la thèse est consacrée aux résultats, à commencer par les progrès réalisés dans le détecteurs bolométriques de lumière: une description et optimisation du design des détecteurs de lumière, l'effet du traitement antireflet et l'amélioration de la réponse thermique obtenue avec l'effet Neganov-Luke sont présentés. Les résultats sur le développement des prototypes des détecteurs LUMINEU et les mesures sont résumés. Les processus de croissance et purification des cristaux $ZnMoO_4$ sont aussi présentés. Sur la base de ces résultats nous avons calculé une sensibilité finale sur une expérience à venir basée sur ces détecteurs.
Enfin, nous présentons un spin-off du projet LUMINEU qui consiste dans un prototype d'un bolomètre scintillant réalisé avec un absorbeur composé alternatif, Li_2MoO_4. Nous examinons les avantages et les désavantages par rapport au $ZnMoO_4$.
Ce manuscrit a comme but d'être un guide à une approche expérimentale pour la recherche de la double désintégration bêta sans émission de neutrinos, un manuel pour les opérations de bolomètres scintillants et un rapport sur l'expérience réussie du projet LUMINEU.

Contents

Acronyms

AC	**A**lternating **C**urrent
ADC	**A**nalog to **D**igital **C**onverter
CL	**C**onfidence **L**evel
CMB	**C**osmic **M**icrowave **B**ackground
CSNSM	**C**entre de **S**ciences **N**uclé**e**aires et de **S**ciences de la **M**atiére
DC	**D**irect **C**urrent
DP	**D**iscrimination **P**ower
DR	**D**ilution **R**efrigerator
DU	**D**ilution **U**nit
DVP	**D**ifferential **V**oltage **P**re-amplifier
EDF	**E**nergy **D**ensity **F**unctional
FFT	**F**ast **F**ourier **T**ransform
FWHM	**F**ull **W**idth at **H**alf **M**aximum
GUT	**G**rand **U**nified **T**heories
HEM	**H**ot **E**lectron **M**odel
IAS	**I**nstitut d'**A**strophysique **S**patiale
IBM	**I**nteraction **B**oson **M**odel
IVC	**I**nner **V**acuum **C**hamber
LD	**L**ight **D**etector
LED	**L**ight-**E**mitting **D**iode
LNGS	**L**aboratori **N**azionali del **G**ran **S**asso
LSM	**L**aboratoire **S**outerrain de **M**odane
LTD	**L**ow **T**emperature **D**etector
LTG Cz	**L**ow-**T**hermal-**G**radient **Cz**ochralski technique
LUMINEU	**L**uminescent **U**nderground **M**olybdenum **I**nvestigation

	for **NEU**trino mass and nature
LY	**L**ight **Y**ield
MC	**M**ixing **C**hamber
MIT	**M**etal **I**nsulator **T**ransition
MMC	**M**etallic **M**agnetic **C**alorimeter
NIIC	**N**ikolaev **I**nstitute of **I**norganic **C**hemistry
NL	**N**eganov-**L**uke
NME	**N**uclear **M**atrix **E**lement
NSM	**N**uclear **S**hell **M**odel
NTD	**N**eutron **T**ransmutation **D**oped
PHFB	**P**rojected **H**artree-**F**ock-**B**ogoliubov
PID	**P**roportional–**I**ntegral–**D**erivative
PMD	**P**honon **M**ediated **D**etector
PT	**P**ulse **T**ube
PTFE	**P**oly**T**etra**F**luoro**E**thylene
QF	**Q**uenching **F**actor
QRPA	**Q**uasi-particle **R**andom **P**hase **A**pproximation
R&D	**R**esearch and **D**evelopment
RMS	**R**oot **M**ean **S**quare
ROI	**R**egion **O**f **I**nterest
SM	**S**tandard **M**odel
SOS	**S**ilicon **O**n **S**apphire
TES	**T**ransition **E**dge **S**ensor
TF	**T**ransfer **F**unction
TPC	**T**ime **P**rojection **C**hamber
TVL	**T**est **V**alue **L**eft
TVR	**T**est **V**alue **R**ight
VRH	**V**ariable **R**ange **H**opping
ΛCDM	Lambda **C**old **D**ark **M**atter

Physical Constants

Speed of Light	c	=	$2.997\ 924\ 58 \times 10^{8}$ ms^{-1}
Planck constant	h	=	$6.626\ 069\ 57(29) \times 10^{-34}$ Js
Gravitational constant	G	=	$6.673\ 84(80)$ m^{3}kg^{-1}s^{-2}
Electron charge	e	=	$1.602\ 176\ 565(35) \times 10^{-19}$ C
Electron mass	m_e	=	$0.510\ 998\ 928(11)$ MeVc^{-2}
		=	$9.109\ 382\ 91(40) \times 10^{-31}$ kg
Proton mass	m_p	=	$938.272\ 046(21)$ MeVc^{-2}
Avogadro constant	N_A	=	$6.022\ 141\ 29(27) \times 10^{23}$ mol^{-1}
Boltzman constant	k_b	=	$1.380\ 6488(13) \times 10^{-23}$ JK^{-1}

Chapter 1

Neutrino mass and nature

Neutrino takes an important place in our understanding of how nature behaves. Neutrino is a fundamental particle which interacts only weakly with matter and since it was first postulated, more than 80 years ago, its study has been puzzling. Up to now the whole picture of the neutrino field is still incomplete. Large and sophisticated experiments had to be conceived in order to detect and study it. The successful Standard Model theory precisely predicts the behaviour of elementary particles and obtained a number of experimental confirmations but it partially fails in the neutrino field: this is an evidence of lack in our comprehension.
A full understanding of neutrinos and related processes will answer some important questions raised in particle physics and cosmology. In particular the neutrinoless double beta decay ($0\nu\beta\beta$) – subject of this thesis – can give the following information:

- Determination of the nature - Dirac or Majorana - of massive neutrinos. This is of fundamental importance for making progress in our understanding of the origin of neutrino masses and mixing and of the symmetries governing the lepton sector of particle interactions.
- Determination of significant constraints on the absolute scale of neutrino masses.
- Concurrence to the determination of the sign of Δm^2_{31} and of the type of the neutrino mass spectrum.
- Constraints on the Majorana phases.

In addition, if it is a Majorana particle, neutrino could give a satisfying solution to the matter-antimatter asymmetry in the Universe through the mechanism known as leptogenesis, as it could provide an additional source of CP violation in the lepton sector.
$0\nu\beta\beta$ is a very rare nuclear transition, never observed, with a half life of $T_{1/2}>10^{25}$ years. Performing an experiment sensitive to this process requires a huge development in different technological aspects. The detector has to be large with a high energy resolution and efficiency. The field has developed a lot in the past ten years: now almost 1000 physicists work on $0\nu\beta\beta$.
In this thesis, the scintillating bolometer technique is presented and the final aim is to demonstrate that an experience based on this technology is capable of reaching a

sensitivity good enough to at least show a path to the solution of intriguing experimental challenges.

This chapter will present a summary on neutrino and related physics in order to introduce the $0\nu\beta\beta$ subject; then the experimental requirements and problematic will be discussed to fully understand the difficulties, the reach and the possible outcomes of the foreseen experiments.

1.1 Introduction to neutrino physics

Since the early stages of nuclear physics it was clear that the beta decay (β-decay) was different from the other nuclear decays such as the α-decay and the radiative decay. The energy spectrum of the emitted electron in fact shows a continuum with a maximum at approximately 1/3 of the Q-value, while the other decays show a monochromatic peak. In early 1900, J. Chadwick demonstrated this feature, which raised a problem of energy conservation [1]. The problem was finally solved by W. Pauli who suggested a three body decay where one of the emitted objects is not detected by the instruments. This third emitted particle has to be neutral and with spin $\frac{1}{2}$ for charge and angular momentum conservation. Today we represent the β-decay as follows:

$$\begin{aligned} N(A,Z) &\longrightarrow N(A,Z+1) + e^- + \bar{\nu} \\ N(A,Z) &\longrightarrow N(A,Z-1) + e^+ + \nu \end{aligned} \tag{1.1}$$

$N(A,Z)$ is a nuclide with mass number A and atomic number Z, e^- is the electron, e^+ is the positron, ν is the neutrino, $\bar{\nu}$ is the antineutrino. The β-decay theory was formally developed by E. Fermi with his weak interaction theory [2] in 1932-34. He called the missing particle neutrino. Fermi's theory gives a good description of the process shown in eq:1.1; it explains the shape of the energy spectrum of the emitted electron, the relation between the Q-value of the reaction and the lifetime $T_{\frac{1}{2}}$ and assumes a negligible mass for the neutrino.

1.1.1 Neutrinoless double beta decay

Subsequently to this description, M. Goeppert-Mayer, in 1935, pointed out the possibility that the nuclear transition could happen with two simultaneous β-decays [3]:

$$N(A,Z) \longrightarrow N(A,Z+2) + 2e^- + 2\bar{\nu} \tag{1.2}$$

This process, called double beta decay ($2\nu\beta\beta$), can occur in nuclei with an even number of neutrons (n) and protons (p). For some of these nuclei the $2\nu\beta\beta$ decay is possible when the β-decay to the intermediate nucleus is energetically forbidden due to the pairing interaction or strongly suppressed by a large difference in spin (fig:1.1). In this work the half life of such a process was estimated, using Fermi's theory of β-decay, to be $>10^{17}$ years.

A few years later, Ettore Majorana demonstrated that the successful theory of β-decay remained unchanged under the assumption of the existence of a neutrino not different from its antiparticle: $\nu \equiv \bar{\nu}$ [4]. Majorana was therefore proposing a new type of fermion, not yet observed in nature, which coincides with its own antiparticle. Immediately after, G. Racah [5] noticed that if neutrinos are Mayorana particles (in contrast with Dirac's

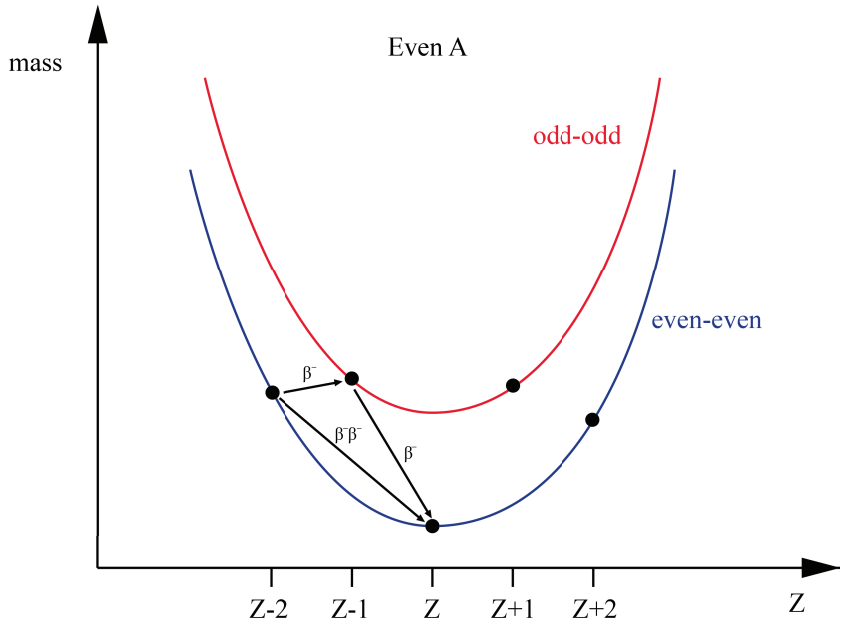

FIGURE 1.1: Mass parabolas for nuclear isobars with even A. Due to the pairing interaction in the semi-empirical mass formula, even-even nuclei have smaller masses than odd-odd nuclei. Therefore, two single β^--decays are disfavoured as the intermediate state is forbidden, though $2\beta^-$ decay is energetically possible as a second-order process from (A,Z-2) to (A,Z).

description) the emitted anti-neutrino can be absorbed by another nuclide to induce the reaction:

$$\bar{\nu}(=\nu) + N(A,Z) \longrightarrow N(A,Z+1) + e^- \tag{1.3}$$

This reaction is forbidden in the SM for a Dirac ν.
In 1939 Furry [6] analyzed the ideas of Majorana and Racah and considered for the first time the $0\nu\beta\beta$ decay (eq:1.4), a nuclear transition of the (A,Z) nucleus to a (A,Z+2) nucleus with the emission of only two electrons. In this process the first emitted neutrino is absorbed in the second vertex as a virtual intermediate neutrino (fig:1.2); this is possible since $\nu \equiv \bar{\nu}$ and the process in eq:1.3 is allowed:

$$N(A,Z) \longrightarrow N(A,Z+2) + 2e^- \tag{1.4}$$

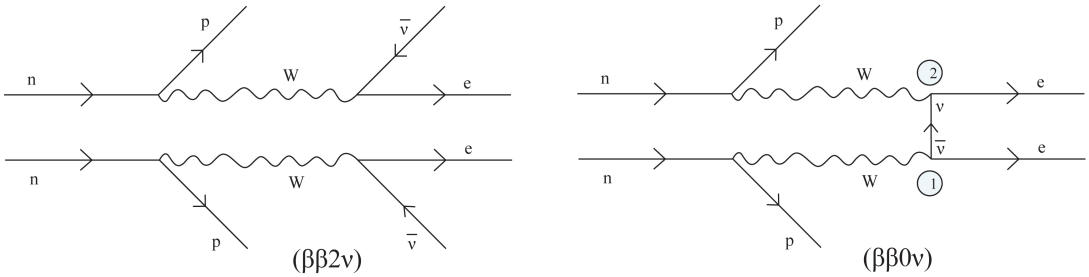

FIGURE 1.2: Feynman's diagrams of the $2\nu\beta\beta$-decay (left) and the $0\nu\beta\beta$-decay (right)

1.1.2 Neutrinos in the Standard Model

During the following years, the detection of the neutrino and the measurement of the 2β-decay half life became object of intensive study but both were far from the technology of that time. Scientists did not have nuclear reactors to use as neutrino sources and they learned only long afterwards to use the sun as a neutrino source. Only in 1956 two American scientists, Frederick Reines and Clyde Cowan, reported the first evidence for neutrinos [7]. They used a fission reactor as a neutrinos source and a well-shielded scintillator detector nearby to detect them through the process

$$\bar{\nu}_e + p \longrightarrow e^+ + n. \tag{1.5}$$

One year later, Davis' experiment [8], which searched for antineutrinos from the reactor via the nuclear reaction:

$$\bar{\nu}_e + {}^{37}\mathrm{Cl} \longrightarrow {}^{37}\mathrm{Ar} + e^- \tag{1.6}$$

produced a zero result. These experiments were interpreted as a proof that the neutrino was not a Majorana particle, but a Dirac particle. This prompted the introduction of the lepton number (L) to distinguish the neutrino from its antiparticle. The assumption of L conservation allows $2\nu\beta\beta$ but forbids $0\nu\beta\beta$, in which L is changed by two units.
It is important to find a way to disentangle the neutrino from its antiparticle. Maurice Goldhaber, Lee Grodzins and Andrew Sunyar, at the Brookhaven National Laboratory demonstrated that the new neutrino has a left-handed helicity and the anti-neutrino has a right-handed one [9]. Helicity commutes with the hamiltonian and is invariant under Lorentz transformation only for massless particles. The weak interaction is actually sensitive to the particle chirality, which is an intrinsic property and is equivalent to helicity for vanishing mass particles. A particle with negative chirality is said to be left-handed, the opposite holds for right-handed.
The chirality projector operator is defined as follows:

$$\begin{array}{ll} \text{left-handed chiral projector} & P_L = \frac{1}{2}\left(1-\gamma^5\right) \\ \text{right-handed chiral projector} & P_R = \frac{1}{2}\left(1+\gamma^5\right) \end{array} \tag{1.7}$$

where $\gamma^5 = i\gamma^0\gamma^1\gamma^2\gamma^3$ and γ^i are the Dirac's matrices. This operator acts on the particle spinor projecting its left-handed or right-handed component.
The chirality is the eigenvalue of the γ^5 matrix

$$\begin{cases} \gamma^5\psi_L = -\psi_L \\ \gamma^5\psi_R = +\psi_R \end{cases} \tag{1.8}$$

In the following period the experiments became more sophisticated and the neutrino started to be better understood. A group of scientists from the Columbia University and the Brookhaven National Laboratory performed the first accelerator neutrino experiment and demonstrated the existence of two species of neutrinos, the electron neutrino, ν_e, and the muon neutrino, ν_μ. Later the absence of a radiative decay of the type $\mu^- \longrightarrow e^- + \gamma$ led to the introduction of their own lepton numbers for ν_e and e^- and for ν_μ and μ^-, respectively. From the 60'ies the possibility for the neutrino to be a Majorana particle became less popular, and neutrinos were considered massless in the SM theory.
The neutral currents were observed (1973) and today we have proved the existence of a

third type of neutrino, ν_τ.

1.1.3 Neutrino oscillations

One problem has remained a hot topic for a long time: the observation of the neutrinos coming from the sun measured far fewer neutrinos than solar models had predicted. Already in the early 50'ies an Italian physicist, Bruno Pontecorvo, living in the USSR, formulated a theory of neutrino oscillations [10][11]. He showed that, if different species of neutrinos exist, they might be able to oscillate back and forth between different flavours in analogy with the quark behaviour in weak decays. This hypothesis was finally confirmed by the Super-Kamiokande experiment which presented significant new data on the deficit of muon neutrinos produced in the Earth's atmosphere [12]. The data suggested that the deficit varies depending on the distance the neutrinos travel – an indication that atmospheric neutrinos oscillate and have mass. The discovery of flavor oscillations of atmospheric neutrinos opened the way to the solution of the solar neutrino deficit too. SNO proved in 2001 that also the solar neutrino puzzle is explained by neutrino oscillations [13]. A confirmation, with a stricter constraint of the oscillation parameters, came from the KamLAND experiment with reactor neutrinos in 2008 [14]. Nowadays, atmospheric, solar, reactor and accelerator neutrino oscillation experiments have proven that neutrinos are massive and mixed particles. Neutrino oscillation is a quantum-mechanical phenomenon where a massive neutrino with flavour ν_l is a superposition of ν_i mass eigenstates according to the mixing relation:

$$\nu_l = \sum_{i=1}^{3} U_{li}\nu_i \quad l = e, \mu, \tau \tag{1.9}$$

The phenomenological demonstration of this superposition consists in a flavour change for a neutrino traveling along a distance L – e.g. an electron neutrino is generated in the sun and a muon or tau neutrino is detected on earth –. This can be understood because the different mass values of ν_i imply different phases for their wave functions in free space. Therefore, the original mixture corresponding to an electron neutrino is modified along the propagation, leading to a state which is in general a superposition of the three flavor states.
The probability of the transition is given [15] by the expression

$$\begin{aligned} P_{\nu_l \to \nu_{l'}} = \delta_{ll'} &- 4 \sum_{1>k} \mathcal{R}e[U^*_{li} U_{l'i} U_{lk} U^*_{l'k}] sin^2 \left(\frac{\Delta m^2_{ki} L}{4E} \right) \\ &+ 2 \sum_{1>k} \mathcal{I}m[U^*_{li} U_{l'i} U_{lk} U^*_{l'k}] sin \left(\frac{\Delta m^2_{ki} L}{2E} \right) \end{aligned} \tag{1.10}$$

The Δm^2_{ki} terms are the squared difference of the ν_i and ν_k masses: $\Delta m^2_{ki} = m^2_{\nu_i} - m^2_{\nu_k}$; L is the distance between the neutrino detector and the source and E is the energy of the neutrino. U is the so-called Pontecorvo-Maki-Nakagawa-Sakata mixing matrix [10],

described by the following expression:

$$U_{PMNS} = \begin{bmatrix} 1 & 0 & 0 \\ 0 & c_{23} & s_{23} \\ 0 & -s_{23} & c_{23} \end{bmatrix} \times \begin{bmatrix} c_{13} & 0 & s_{13}e^{-i\delta} \\ 0 & 1 & 0 \\ -s_{13}e^{i\delta} & 0 & c_{13} \end{bmatrix} \times \begin{bmatrix} c_{12} & s_{12} & 0 \\ -s_{12} & c_{12} & 0 \\ 0 & 0 & 1 \end{bmatrix} \times \begin{bmatrix} e^{i\xi_1/2} & 0 & 0 \\ 0 & e^{i\xi_2/2} & 0 \\ 0 & 0 & 1 \end{bmatrix} =$$
$$= \begin{bmatrix} c_{12}c_{13} & s_{12}c_{13} & s_{13}e^{-i\delta} \\ -s_{12}c_{23} - c_{12}s_{23}s_{13}e^{i\delta} & c_{12}c_{23} - s_{12}s_{23}s_{13}e^{i\delta} & s_{23}c_{13} \\ s_{12}s_{23} - c_{12}c_{23}s_{13}e^{i\delta} & -c_{12}s_{23} - s_{12}c_{23}s_{13}e^{i\delta} & c_{23}c_{13} \end{bmatrix} \times \begin{bmatrix} e^{i\xi_1/2} & 0 & 0 \\ 0 & e^{i\xi_2/2} & 0 \\ 0 & 0 & 1 \end{bmatrix} \tag{1.11}$$

where $c_{ab} \equiv \cos\vartheta_{ab}$ and $s_{ab} \equiv \sin\vartheta_{ab}$, with the three mixing angles ϑ_{12}, ϑ_{23}, ϑ_{13}. δ is the Dirac CP-violating phase and ξ_i are the Majorana CP-violating phases.
The oscillation effect is maximum when $\Delta m^2_{ki} \sim E/L$. The observation of this phenomenon implies that at least two over three neutrinos have mass eigenvalues $\neq 0$.
The neutrino oscillation experiments measured all the mixing angles and Δm^2 (summarised in tab:1.1). There is no precise information on the Dirac CP-violating phase δ. The value Δm^2_{12}, measured from the ν_e disappearance in the sun flux, is often called Δm^2_S and is known with its sign. From the experiment which measured the disappearance of the atmospheric ν_μ and $\bar{\nu_\mu}$ we get the value of Δm^2_A, which is known in absolute value, and due to the fact that $\Delta m^2_S \ll \Delta m^2_A$, in the framework of the three neutrino mixing it holds:

$$\Delta m^2_A = \frac{1}{2}\left|\Delta m^2_{13} + \Delta m^2_{23}\right| \tag{1.12}$$

	Best fit(3σ ranges)	
Parameter	Normal Hierarchy	Inverted Hierarchy
Δm^2_{21} [10^{-5} eV]	7.54(6.99-8.18)	
$\lvert\Delta m^2_{31}\rvert$ [10^{-3} eV]	2.43(2.23-2.61)	2.38(2.19-2.56)
$\sin^2\theta_{12}$	0.308(0.259-0.359)	
$\sin^2\theta_{23}$,	0.437(0.374-0.628)	0.455(0.380-0.641)
$\sin^2\theta_{13}$,	0.0234(0.0176-0.0295)	0.0240(0.0178-0.0298)
δ/π (2σ ranges)	1.39((0.00-0.16)$\oplus$(0.86-2.00)	1.31((0.00-0.02)$\oplus$(0.70-2.00)

TABLE 1.1: The best-fit values and 3σ ranges of the 3 neutrinos mixing parameters [16].

1.1.4 Neutrino mass in the Standard Model

Neutrino oscillation experiments give a convincing demonstration of the massive nature of neutrino in contrast with the minimal Standard Model formulation. There are several mechanisms which can give mass to neutrino; one of the most appealing is the so called see-saw mechanism [16].
It is believed that particles acquire a mass through Yukawa coupling with the Higgs field. Each interaction with this field changes particle handedness, and heavy particles like the tauon scatter much more frequently than light particles like the electron with the vacuum fluctuations of the Higgs field. The weak interaction violates parity maximally within the accuracy we can measure. Since right-handed neutrinos do not participate to weak interactions in the SM, left-handed neutrinos propagate freely in the Higgs field background and this leads to the massless nature of this particle [16].

We have now to reconsider neutrinos as massive particles. If the right-handed neutrino field is added in the SM, the neutrino masses can be generated by the standard Higgs mechanism via the Yukawa interaction. After the spontaneous breaking of the electroweak symmetry we obtain the Dirac mass term

$$\mathcal{L}^D = -\sum_{l',l} \bar{\nu}_{l'L} M^D_{l'l} \nu_{lR} + h.c. \quad l = e, \mu, \tau \tag{1.13}$$

with

$$M^D_{l'l} = \frac{Y_{l'l}}{\left(\sqrt{2}G_F\right)^{\frac{1}{2}}} \tag{1.14}$$

where G_F is the Fermi constant and $Y_{l'l}$ are the Yukawa coupling constants. After the diagonalization of the $Y_{l'l}$ matrix, the Dirac masses are obtained. The problem is to justify the small masses of the neutrino, leading to Yukawa coupling constants ten orders of magnitude smaller with respect to the other particles.
More generally, the neutrino mass Lagrangian would in fact include terms for the Dirac masses as well as terms for the Majorana masses:

$$\mathcal{L} \sim m_D \left[\bar{\psi}_L \psi_R + ...\right] + \left[m_L \bar{\psi}^C_L \psi_L + m_R \bar{\psi}^C_R \psi_R + h.c.\right] \tag{1.15}$$

The Dirac mass m_D, which represents the strength of the coupling to the Higgs field, would be the term that neutrinos would share in common with the charged fermions. Two Majorana terms, coupling left-handed fields to left-handed fields and right-to-right, with strengths m_L and m_R, can also be formed. The above interactions lead to a neutrino mass matrix that schematically takes the form

$$M_\nu = \begin{bmatrix} 0 & m_D \\ m_D & m_R \end{bmatrix} \tag{1.16}$$

where $m_L = 0$, as foreseen by the standard model principle. Diagonalizing the mass matrix, we find two eigenvalues, one heavy $\sim m_R$ and one light, which we associate with the light neutrino mass scale:

$$m_\nu \sim \frac{m_D^2}{m_R} \tag{1.17}$$

The new Majorana mass terms in combination with the Dirac mass provide a natural explanation for the anomalous scale of neutrino masses which is reduced by the factor m_D/m_R.

1.2 Absolute neutrino mass

The determination of the absolute value of neutrino masses is an open problem that cannot be solved by neutrino oscillations, which depend only on the differences of the squares of the neutrino masses.
However the neutrino oscillation experiments partially constrain the ordering of the three neutrino masses. Given the positive sign of Δm^2_{21}, we know that $m_2 > m_1$, while the still unknown sign of Δm^2_A leaves two possible scenarios (fig:1.3).

Normal mass hierarchy: $m_1 < m_2 \ll m_3$
The mass of the neutrinos as a function of the lightest one is

$$m_2 = \sqrt{m_1^2 + \Delta m_S^2}, \quad m_3 = \sqrt{m_1^2 + \Delta m_A^2 + \Delta m_S^2/2} \tag{1.18}$$

Due to the large difference in mass splitting, $\Delta m_s^2 \ll \Delta m_A^2$, it is possible to approximate m_3 as:

$$m_3 \simeq \sqrt{\Delta m_A^2} \approx 5 \times 10^{-2} \text{ eV} \tag{1.19}$$

Inverted mass hierarchy: $m_3 \ll m_1 < m_2$
In this case, the mass of the neutrinos as a function of the lightest one is

$$m_1 = \sqrt{m_3^2 + \Delta m_A^2 - \Delta m_S^2/2}, \quad m_2 = \sqrt{m_3^2 + \Delta m_A^2 + \Delta m_S^2/2} \tag{1.20}$$

which leads to

$$m_3 \ll m_1 \simeq m_2 \simeq \sqrt{\Delta m_A^2} \approx 5 \times 10^{-2} \text{ eV} \tag{1.21}$$

Quasi-degenerate mass hierarchy: $m_1 \simeq m_2 \simeq m_3$
This approximation makes sense when $\Delta m_s^2 \ll m_i^{QD}$ which in this case leads to

$$m_i^{QD} \gg \sqrt{\Delta m_A^2} \approx 5 \times 10^{-2} \text{ eV} \tag{1.22}$$

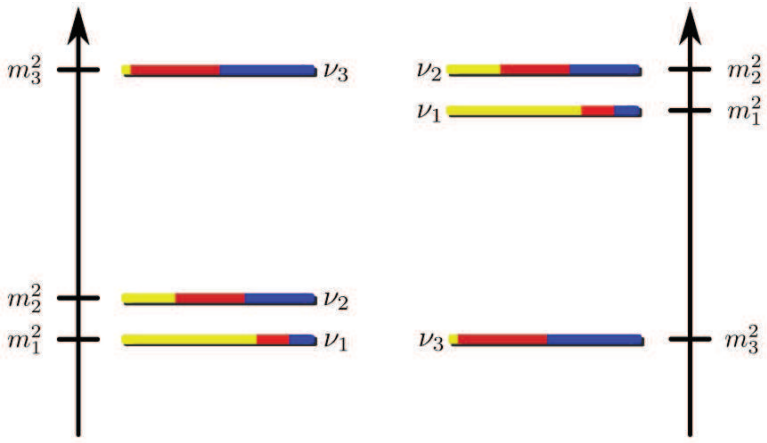

FIGURE 1.3: Schematic scale of the neutrino masses in the cases: normal hierarchy (left) and inverted hierarchy (right). The absolute value is unknown. The colours of the line represent the fraction of ν_e (yellow), ν_μ (red) and ν_τ (blue).

1.2.1 Measurement of neutrino masses

The direct measurement of neutrino masses is a hard task. In particle physics, the particle mass is commonly obtained by the measurement of two independent kinematic quantities which can be combined to obtain the particle mass itself. This approach fails with neutrinos because neutrinos interact only weakly with matter. However different indirect approaches exist to measure it.

1.2.1.1 Kinematic measurement

These techniques are based on few decays where the relativistic momentum and its conservation are studied

$$E^2 = m^2c^4 + p^2m^2 \tag{1.23}$$

In that case the measurement outcome is m_ν^2. This kind of measurement will always lead to a weighted average of the mass eigenvalues, since the investigated ν_l will be in a flavour state:

$$m_{\nu_l}^2 = \sum_{i=1}^{3} |U_{li}|^2 \, m_{\nu_i}^2 \tag{1.24}$$

ν_μ mass measurement
The first upper limit was set in 1956, using the two-body decay of pions ($\pi^\pm$); even now this is the best method to study this parameter:

$$\pi^+ \longrightarrow \mu^+ + \nu_\mu \tag{1.25}$$

Using eq:1.23 in the pion rest frame and imposing momentum conservation one obtains

$$m_{\nu_\mu}^2 = m_\pi^2 + m_\mu^2 - 2m_\pi\sqrt{m_\mu^2 + p_\mu^2} \tag{1.26}$$

This has yielded the upper limit of m_{ν_μ}<190 keV at 90% confidence [17], with the dominant error due to our imprecise knowledge of the pion mass.

ν_τ mass measurement
The tau neutrino has been studied through its multi-hadronic decays using the electron-positron colliders. One of the possible decay channels is

$$\tau^- \longrightarrow 3\pi^- + 2\pi^+ + (\pi^0) + \nu_\tau \tag{1.27}$$

From the measurement of the energy of the hadronic products it is possible to infer the mass of ν_τ. In the τ^- reference frame we obtain

$$E_h = \frac{m_\tau^2 + m_h^2 - m_\nu^2}{2m_\tau} \tag{1.28}$$

The problem is to record and to reconstruct all the five pions with enough precision in order to be sensitive to the missing energy and momentum carried away by the ν_τ. The upper limit for the mass of the ν_τ is currently m_{ν_τ}<18.2 MeV at 95% C.L. [18].

1.2.1.2 β decay

From a precise measurement of the electron energy spectrum of a β decay it is in principle possible to obtain the neutrino mass. A non-zero neutrino mass has the effect of changing the slope of the curve slightly, and also changing the maximum allowable energy given to the electron (fig:1.4)[1]. This measurement is delicate because many processes can affect the shape at the end point of the spectrum. The β source must have such features to

[1] image taken from the KATRIN website

avoid the self absorption of the electron energy. The decay on an excited state of the daughter nuclide can also affect the shape of the spectrum.
However, the β decay information on the ν_e mass is very reliable since it is related only to kinematics and is model independent. Tritium β decay experiments obtained the most stringent limit on the effective electron neutrino mass and put the most model-independent bounds on the neutrino masses [19]. The following decay is used:

$$^3H \longrightarrow ^3He + e^- + \bar{\nu}_e \tag{1.29}$$

$$m_\beta^2 = \sum_{i=1}^{3} |U_{ei}|^2 m_i^2 \tag{1.30}$$

The KATRIN experiment [20] will be the most sentive experiment on tritium β decay. It is scheduled to start in 2016 with an expected sensitivity on m_β of about 0.2 eV. The present limits are obtained in the Mainz [21] and Troitsk [22] experiments: $m_\beta \leq 2.3 - 2.05$ eV respectively.

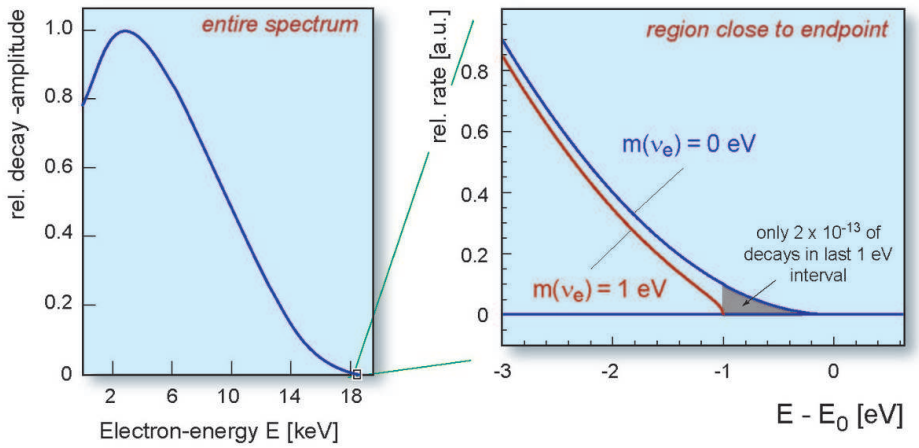

FIGURE 1.4: Spectrum of the tritium β decay. (left) Shape of the whole spectrum. (right) End point of the spectrum; the blue line corresponds to the end point of the spectrum shape with $m_\beta = 1$ eV.

1.2.1.3 Cosmological measurement

Measurements on the Cosmic Microwave Background (CMB) can give information on the neutrino masses. Given the fact that the neutrinos are massive, the distribution of the matter in the early universe is affected by the neutrino density. The analysis of cosmological data with cosmological constant the (ΛCDM) disfavour neutrino masses larger than a fraction of eV.
The most recent results and stringent limits on the sum of the three neutrino masses are given by the Planck experiment [23]. Assuming a spatially flat Universe, the obtained limit combined with other cosmological data gives

$$\sum_{i=3}^{3} m_i < 0.23 \text{ eV} \tag{1.31}$$

with 95% Bayesian probability.
Assuming the degenerate mass pattern the lightest neutrino mass would be $m_i \lesssim 0.071$ eV.

1.3 Neutrinoless double beta decay

Interest on $0\nu\beta\beta$ was renewed in the early '80s. The deficit of solar neutrinos and some wrong claims on neutrino mass measurements contributed to this renascence. Massive neutrinos were considered as candidates for dark matter in cosmology. Grand Unified Theories, which account for the neutrino mass as a Majorana mass, were formulated.
The Feynman diagrams (fig:1.2) describe only one of a pletora of processes that can contribute to $0\nu\beta\beta$, but in 1982 J. Schechter and J. W. F. Valle showed that every possible diagram implies the Majorana mass of the neutrino in the framework of gauge theories [24].
The neutrinoless mode of nuclear double beta decay (described in sec:1.1.1) is a hypothetical, very rare transition of the second order perturbation theory in the Fermi constant G_F. If it is mediated by the exchange of a light virtual neutrino, the decay rate can be calculated as

$$\left[T^{0\nu}_{\frac{1}{2}}\right]^{-1} = |m_{\beta\beta}|^2 \left|M^{0\nu}\right|^2 G^{0\nu} \tag{1.32}$$

where $m_{\beta\beta}$ is the effective Majorana mass, $M^{0\nu}$ is the nuclear matrix element and $G^{0\nu}$ is the phase space factor.
The evidence of $0\nu\beta\beta$ will determine the Majorana nature of massive neutrinos ν_i. This is of fundamental importance for making progress in our understanding of the origin of neutrino masses and mixing and of the symmetries governing the lepton sector of particle interactions.
An experiment on $0\nu\beta\beta$ aims to measure the $T^{0\nu}_{\frac{1}{2}}$ of the process. If the experiment reports a positive result, it would be an indirect measurement of the value of $m_{\beta\beta}$.
It is useful to describe each term of eq:1.32.

1.3.1 The effective Majorana neutrino mass $m_{\beta\beta}$

The decay rate of $0\nu\beta\beta$ is proportional to the square of the so called effective Majorana mass that can be expressed in terms of the elements of the first row of the PNMS matrix:

$$m_{\beta\beta} = \left|\sum_{i=1}^{3} U^2_{ei} m_{\nu_i}\right|. \tag{1.33}$$

The information provided by the neutrino oscillation experiments constrains $m_{\beta\beta}$, which can be written in explicit form as

$$m_{\beta\beta} = \left|cos^2\vartheta_{12}cos^2\vartheta_{13}e^{i2\xi_1}m_{\nu_1} + sin^2\vartheta_{12}cos^2\vartheta_{13}e^{i2\xi_2}m_{\nu_2} + sin^2\vartheta_{13}m_{\nu_3}\right|. \tag{1.34}$$

For the different mass patterns, it can be expressed as a function of the lightest mass value (fig:1.5).

Inverted mass hierarchy: $m_3 \ll m_1 < m_2$
The smallest neutrino mass is m_3 and the other two mass values can be expressed in terms of m_3 and mass splitting as shown in eq:1.20. Substituting in eq:1.34 and neglecting m_3, given its smallness, one obtains:

$$m_{\beta\beta} \approx \sqrt{\Delta m^2_A} cos^2\vartheta_{13} \left(1 - sin^2 2\vartheta_{12} sin^2\left(\xi_1 - \xi_2\right)\right)^{\frac{1}{2}} . \tag{1.35}$$

In this approximation the only unknown parameter is the Majorana phase difference. The value of $m_{\beta\beta}$ is then bounded in the interval

$$\sqrt{\Delta m^2_A} cos^2\vartheta_{13} cos^2 2\vartheta_{12} \approx 2 \times 10^{-2} \text{ eV} \lesssim m_{\beta\beta} \lesssim \sqrt{\Delta m^2_A} cos^2\vartheta_{13} \approx 5 \times 10^{-2} \text{ eV} \tag{1.36}$$

Normal mass hierarchy: $m_1 < m_2 \ll m_3$
In this context, the smallest neutrino mass is m_1. Using then eq:1.34 and eq:1.18 one obtains:

$$m_{\beta\beta} \approx \left| \sqrt{\Delta m^2_S} cos^2\vartheta_{13} sin^2\vartheta_{12} e^{i2\xi_2} + \sqrt{\Delta m^2_A} sin^2\vartheta_{13} \right| \tag{1.37}$$

The term in m_1 is neglected. These two terms are of the same order of magnitude because the largest squared mass difference Δm^2_A is suppressed by the small factor $sin^2\vartheta_{13}$. This time the unknown Majorana phase can cancel the second terms allowing $m_{\beta\beta}$ to vanish in an unlucky combination of parameters. Only an upper limit can be set in this approximation for $\xi_2 = 0$:

$$m_{\beta\beta} \lesssim \left| \sqrt{\Delta m^2_S} cos^2\vartheta_{13} sin^2\vartheta_{12} + \sqrt{\Delta m^2_A} sin^2\vartheta_{13} \right| \approx 4 \times 10^{-3} \text{ eV} \tag{1.38}$$

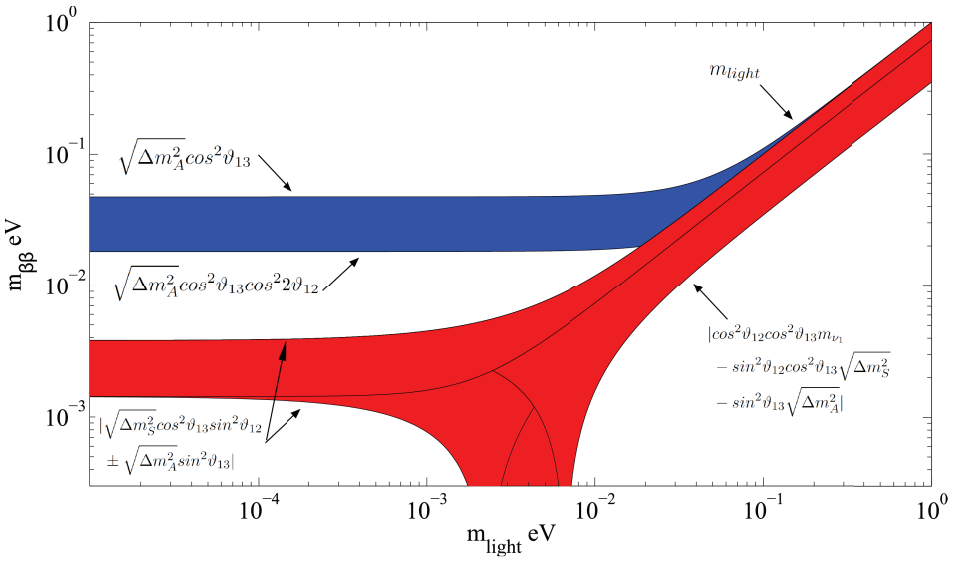

FIGURE 1.5: Effective Majorana neutrino mass as a function of the lightest neutrino mass in the normal hierarchy $m_1 < m_2 < m_3$ (red), and in the inverted hierarchy $m_3 < m_1 < m_2$ (blue) scenarios. The bands are computed with the best fit reported in tab1.1.

The measurement of $m_{\beta\beta}$ will solve the mass pattern problem providing the sign of Δm^2_{31}.

In addition, $m_{\beta\beta}$ leads to determine or obtain significant constraints on the absolute scale of neutrino masses and it will give unvaluable information on the Majorana phases.

1.3.2 Nuclear matrix element $M^{0\nu}$

Unfortunately the derivation of $m_{\beta\beta}$ from the experimental results on the $0\nu\beta\beta$ half life requires a precise knowledge of the transition nuclear matrix elements $M^{0\nu}$ appearing in eq:1.32. The nuclear part of the amplitude turns into a sum of the Gamow-Teller and Fermi nuclear matrix element

$$M^{0\nu} = M^{0\nu}_{GT} + \frac{g_V}{g_A} M^{0\nu}_F \tag{1.39}$$

where $M^{0\nu}_{GT}$ is the axial Gamow-Teller matrix element and $M^{0\nu}_F$ is the vector Fermi matrix element. g_A and g_V represent the axial and vector coupling constants.
The nuclear physics effects can be calculated only with nuclear models which approximate the many body interaction of the nucleons. The current values of the axial coupling constant is $g_A = 1.2723 \pm 0.0023$ [16] for free nucleons.
Many evaluations of the nuclear matrix elements are available in literature, but they are often in considerable disagreement, leading to large uncertainty ranges for $m_{\beta\beta}$. This has been recognized as a critical problem by the community. Different values of g_A are also considered depending on the adopted nuclear model which assumes an effective value g_A^{eff} of g_A.
Five different methods have been used for the calculation of the $0\nu\beta\beta$ decay nuclear matrix elements (NMEs) (reported in fig:1.6 and tab:1.2[2]):
NSM: Nuclear Shell Model – $g_A^{eff} = 1.25$
QRPA: Quasi-particle Random Phase Approximation – $g_A^{eff} = 1.25$
IBM: Interaction Boson Model – $g_A^{eff} = 1.269$
EDF: Energy Density Functional – $g_A^{eff} = 0.93$
PHFB: Projected Hartree-Fock-Bogoliubov approach – $g_A^{eff} = 1.25$ and $g_A^{eff} = 1$

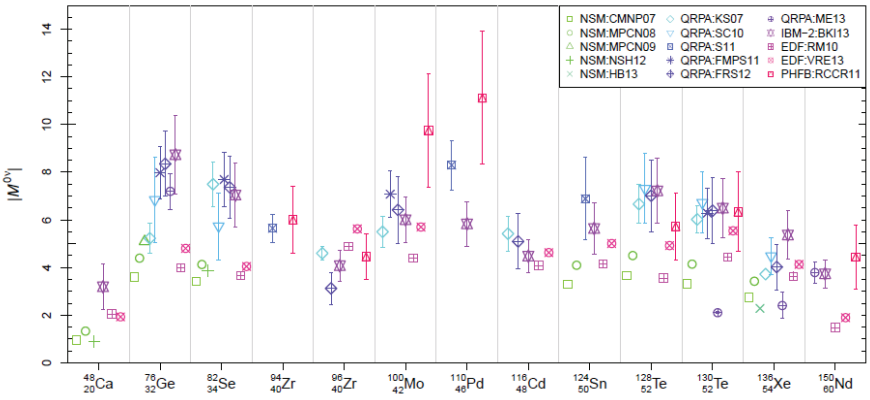

FIGURE 1.6: Values of the nuclear matrix element (NME) $M^{0\nu}$ for several nuclei of experimental interest calculated with different methods. The error bars represent the range of values of $M^{0\nu}$ in the corresponding model under variations of the model parameters and treatment of interactions [25].

[2]The reported values are taken from a recent review [25].

$0\nu\beta\beta$ decay	$M^{0\nu}$	$0\nu\beta\beta$ decay	$M^{0\nu}$
$^{48}Ca \rightarrow ^{48}Ti$	0.89 – 4.14	$^{116}Cd \rightarrow ^{116}Sn$	3.77 – 6.26
$^{76}Ge \rightarrow ^{76}Se$	3.59 – 10.39	$^{124}Sn \rightarrow ^{124}Te$	3.28 – 8.61
$^{82}Se \rightarrow ^{82}Kr$	3.41 – 8.84	$^{128}Te \rightarrow ^{128}Xe$	3.55 – 8.78
$^{96}Zr \rightarrow ^{96}Mo$	2.45 – 5.62	$^{130}Te \rightarrow ^{130}Xe$	2.06 – 8.00
$^{100}Mo \rightarrow ^{100}Ru$	4.39 – 12.13	$^{136}Xe \rightarrow ^{136}Ba$	1.85 – 6.38
$^{110}Pd \rightarrow ^{110}Cd$	4.90 – 13.91	$^{150}Nd \rightarrow ^{150}Sm$	1.48 – 5.80

TABLE 1.2: Range of values of the NMEs from different approaches.

1.3.3 Phase space factor

The phase space factor is given by

$$G^{0\nu}(Q,Z) = \frac{(G_F cos\vartheta_C)^4}{ln2\,(2\pi)^5\,R^2} \int_Q^0 F(Z,\epsilon_1)F(Z,\epsilon_2)p_1p_2\epsilon_1\epsilon_2\delta\,(E_0-\epsilon_1-\epsilon_2)\,d\epsilon_1 d\epsilon_2 \quad (1.40)$$

where G_F is the Fermi constant, ϑ_C is the Cabibbo angle, R is the radius of the nucleus, E_0 is the available energy, Q is the total energy, $F(Z,\epsilon)$ is the Fermi function that describes the Coulomb interaction of the outgoing electron, p is the electron momentum and ϵ is the energy of the electron.
The phase space factor is exactly calculable; in tab:1.3 the values recently obtained with high accuracy [26] for several nuclei are reported. The calculation was made considering the exact Dirac wave functions of the electrons, taking into account the finite nuclear size and electron screening.

$0\nu\beta\beta$ decay	$G^{0\nu}$ $[10^{-26}\mathrm{y}^{-1}\mathrm{eV}^{-2}]$	$0\nu\beta\beta$ decay	$G^{0\nu}$ $[10^{-26}\mathrm{y}^{-1}\mathrm{eV}^{-2}]$
$^{48}Ca \rightarrow ^{48}Ti$	9.501	$^{116}Cd \rightarrow ^{116}Sn$	6.396
$^{76}Ge \rightarrow ^{76}Se$	0.9049	$^{124}Sn \rightarrow ^{124}Te$	3.462
$^{82}Se \rightarrow ^{82}Kr$	3.891	$^{128}Te \rightarrow ^{128}Xe$	0.2251
$^{96}Zr \rightarrow ^{96}Mo$	7.881	$^{130}Te \rightarrow ^{130}Xe$	5.446
$^{100}Mo \rightarrow ^{100}Ru$	6.097	$^{136}Xe \rightarrow ^{136}Ba$	5.584
$^{110}Pd \rightarrow ^{110}Cd$	1.844	$^{150}Nd \rightarrow ^{150}Sm$	24.14

TABLE 1.3: Phase space factor calculated for several $0\nu\beta\beta$ candidate nuclei.

1.4 Detection of the neutrinoless double beta decay

After the spectacular experimental progress made in the studies of neutrino oscillations, further understanding of the pattern of neutrino masses and neutrino mixing require a challenging research program. In particular the research on $0\nu\beta\beta$ can really provide unvaluable information, and a proof of the Majorana nature of neutrinos.
The detection of this process is challenging due to the very low rate of this decay mode. The experimental signature of $0\nu\beta\beta$ is given by the energy spectrum of the two emitted electrons (fig:1.7). In case of $2\nu\beta\beta$, the emitted neutrinos escape with part of the reaction energy; thus the electrons energy is a continuum as in a single β decay.
On the contrary, in the case of the $0\nu\beta\beta$ decay, the whole available energy (Q-value) is

carried by the electrons; then a monochromatic peak will appear, in the electron energy spectrum, at the total transition energy.

In a counting experiment where the rate of $0\nu\beta\beta$ is obtained from the number of events

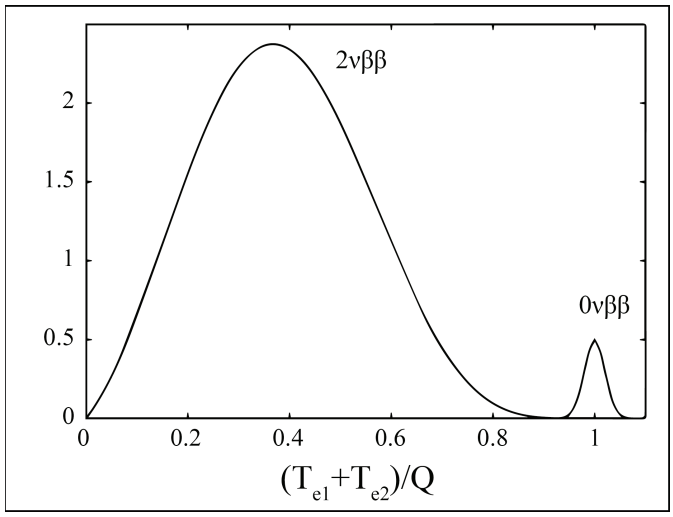

FIGURE 1.7: Schematic example of the sum energy spectrum of the two emitted electrons for the $2\nu\beta\beta$ and $0\nu\beta\beta$ modes.

in the n_{obs} peak, the half life is given by

$$T^{0\nu}_{\frac{1}{2}} = \ln(2)\frac{N_{\beta\beta}}{n_{obs}}t\epsilon \tag{1.41}$$

where t is the measurement time, $N_{\beta\beta}$ is the number of available candidate nuclei and ϵ is the detector efficiency.

The $2\nu\beta\beta$ mode has been detected and measured for several nuclei (tab:1.4). The half life for this mode depends on the isotope and the measured values are in the interval $T^{2\nu}_{\frac{1}{2}} \sim 10^{18}-10^{19}$ y. Only lower limits on the $0\nu\beta\beta$ half life have been set for this process, for which the rate is expected to be much higher, being $T^{0\nu}_{\frac{1}{2}} \sim 10^{27}$ y for $m_{\beta\beta} = 0.1$ eV.

$0\nu\beta\beta$ decay	Q-value	$T^{2\nu}_{\frac{1}{2}}$ y	isotopic abundance
^{48}Ca$\rightarrow^{48}$Ti	4272.26±4.04	$4.4^{+0.5}_{-0.4}\times10^{19}$	0.19
^{76}Ge$\rightarrow^{76}$Se	2039.06±0.01	$1.60^{+0.13}_{-0.1}\times10^{21}$	7.73
^{82}Se$\rightarrow^{82}$Kr	2995.12±2.01	9.2±0.7×10^{19}	8.73
^{96}Zr$\rightarrow^{96}$Mo	3350.37±2.89	2.3±0.2×10^{19}	2.8
^{100}Mo$\rightarrow^{100}$Ru	3034.40±0.17	7.1±0.4×10^{18}	9.82
^{110}Pd$\rightarrow^{110}$Cd	2017.85±0.64	–	11.72
^{116}Cd$\rightarrow^{116}$Sn	2813.50±0.13	2.85±0.15×10^{19}	7.49
^{124}Sn$\rightarrow^{124}$Te	2286.97±1.53	–	5.79
^{128}Te$\rightarrow^{128}$Xe	865.87±1.31	–	31.74
^{130}Te$\rightarrow^{130}$Xe	2526.97±0.23	6.9±1.3×10^{20}	34.08
^{136}Xe$\rightarrow^{136}$Ba	2457±0.37	2.20±0.06×10^{21}	8.86
^{150}Nd$\rightarrow^{150}$Sm	3371.38±0.20	8.2±9×10^{18}	5.64

TABLE 1.4: Summary of the Q-value, isotopic abundance and $T^{2\nu}_{\frac{1}{2}}$ for several nuclei.

1.4.1 Detection techniques

The most diffused experimental technique used to date in the $0\nu\beta\beta$ search experiments is a pure calorimetric technique, where the total electron energy of the two decay electrons is measured via the scintillation light, ionization, or heat deposit (bolometers). The advantage of this technique is the possibility to exploit the so called homogeneous approach, where the source is the detector itself, resulting in a very high efficiency. Another interesting approach is the inhomogeneous tracking detector thanks to the capability of reconstructing the topology of the decay but the scalability and the efficiency are limited because of such long life-times.
There are several parameters that need to be considered for these experiments:

- Efficiency
- Energy resolution
- Particle identification
- Scalability
- Enrichment
- Tracking capability

1.4.1.1 Calorimeter techniques - homogeneus detector

In the following the calorimeter techniques used in $0\nu\beta\beta$ experiments are presented [27].
Semiconductor detectors (fig:1.8): based on Ge diodes they feature an excellent energy resolution and an intrinsic radio-purity. Germanium can be enriched in the isotope of interest ^{76}Ge. The GERDA and MAJORANA experiments exploit this technique. Other semiconductors which can be enriched in other isotopes can be studied (COBRA experiment).

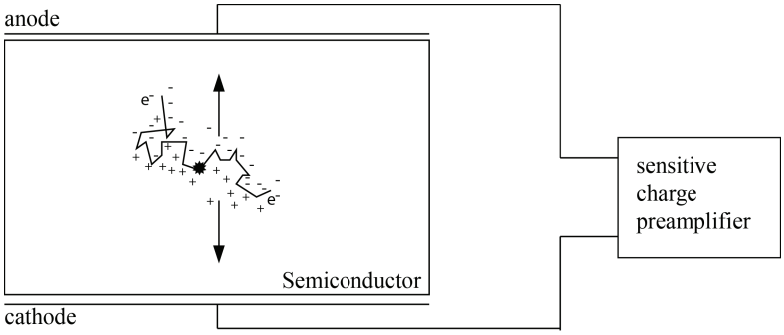

FIGURE 1.8: Ionizing radiation is measured by the number of charge carriers produced in the detector material which is arranged between two electrodes. The number of e-h pairs is proportional to the energy deposit.

Liquid-loaded scintillators (fig:1.9): the main advantage of liquid scintillators is the scalability: they can be huge with an active mass larger than all the other detector types. The bigger they are the more is the shielding power because the outer part shields the

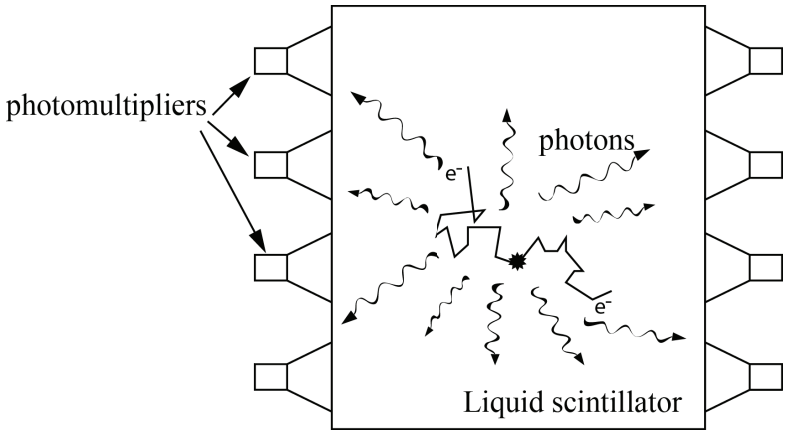

FIGURE 1.9: A scintillation detector is a scintillator coupled to an electronic light sensor like photomultipliers. The number of scintillation photons measured by the light detector is proportional to the energy deposit.

inner part. The main disadvantage is the poor energy resolution. The most important experiments are KamLAND-Zen and SNO+.

Xe Time Projection Chamber (fig:1.10): the ^{136}Xe isotope can be studied in either liquid or gas Xe based TPCs. In both cases the event topology helps in reducing the background. The energy resolution is worse than in bolometers and semiconductors but better than liquid scintillators. The EXO experiment is based on a liquid Xe TPC while the NEXT experiment is based on a gas TPC.

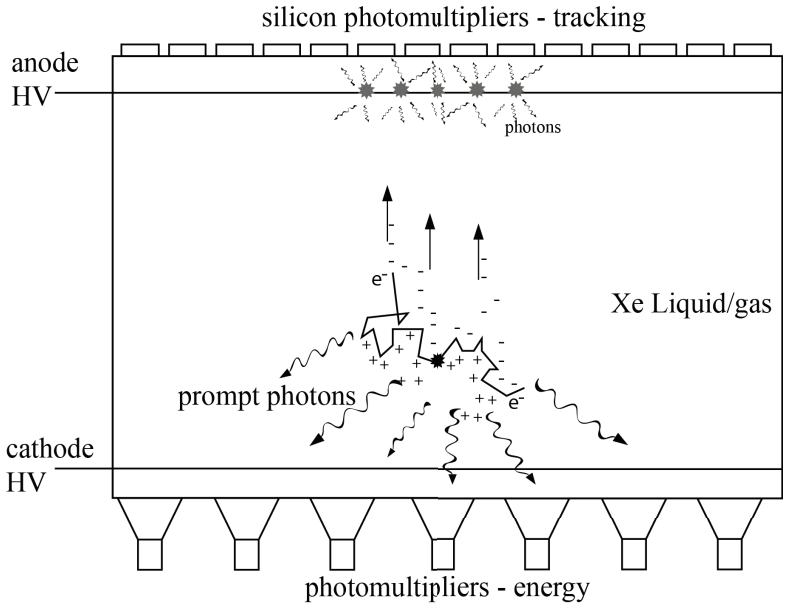

FIGURE 1.10: Particle interactions in the liquid Xe target produce scintillation and ionization. The prompt scintillation light give an energy deposit measurement through the PMTs, the ionization is then drifted into the gas by the stronger electric field. The electric field accelerates the electrons which generate a proportional second scintillation signal which gives topological information.

Bolometric detector (fig:1.11): the thermal readout is characterized by an excellent energy resolution. Almost any dielectric compound works as a bolometer. Therefore,

different isotopes can be investigated and it is demonstrated the capability of scaling the set-up up to tens of kg. A cryostat capable to house hundreds of kg is under commissioning for the CUORE experiment. Complicated cryogenic systems are needed.

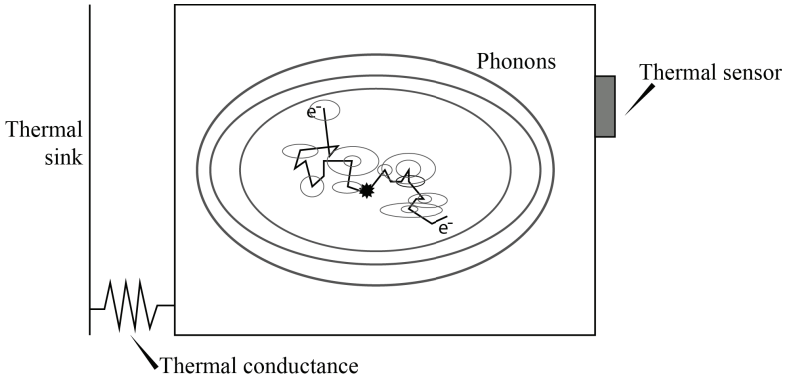

FIGURE 1.11: A bolometer consists in an absorber element where any radiation deposits its energy and increases the temperature above the thermal bath. The temperature change can be measured directly by a resistive thermometer and it is proportional to the deposited energy.

Scintillating bolometers (fig:1.12): they are an upgrade of the simple bolometers, where the absorber can also scintillate. The readout of the scintillation light is performed by an auxiliary bolometer and it enables particle identification with the drawback of doubling the readout channels. AMoRE, LUCIFER and LUMINEU are the main experiments implementing scintillating bolometers

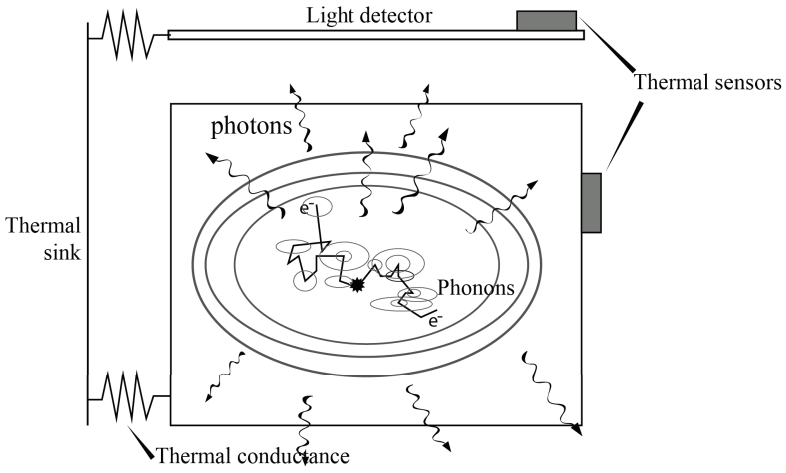

FIGURE 1.12: A scintillating bolometer consists in a bolometer with a scintillating absorber and a second bolometer dedicated to the light readout.

Calorimetric detectors with hybrid readout are very interesting because different particle interactions give a different response with respect to the readout channel; the reason to exploit a double readout is to suppress the background events by means of particle identification.

1.4.1.2 Inhomogeneous detectors

It exists only one experiment which uses an inhomogeneous detector, the tracking detector of SuperNEMO.
Tracking detector (fig:1.13): SuperNEMO is the most advanced experiment adopting this technique where a thin layer containing the source is placed inside a tracker and the electron energy is deposited in a scintillator. The main advantages are the possibility to reconstruct the topology of the events with high accuracy and to study different sources. However, it is difficult to scale up.

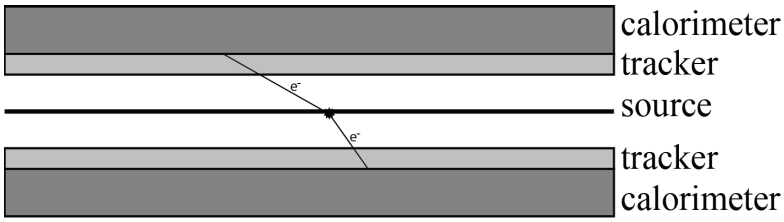

FIGURE 1.13: In a inhomogeneous detector the source is placed in the middle of two tracker elements, used to reconstruct the event topology, and two calorimeter elements to measure the energy of the reaction products.

1.4.2 Isotope selection

When an experiment on $0\nu\beta\beta$ is conceived, the selection of the isotope is important. In agreement with eq:1.32, considerations about the nuclear matrix elements and the phase-space factor are useful to select the isotope with the highest rate. The compatibility with the selected detection technique is also a requirement.
Another important criterion is the isotopic abundance of the isotope; other factors like at available enrichment technique and the costs of enrichment need to be considered too. Last but not least, the Q-value is an important factor: in a counting experiment, if the background is too large it can hide the true signal. There are several sources of background that will be discussed in detail. First of all, it is important not to use isotopes with Q-values near some natural decay energy to avoid misinterpretations.
Three isotopes are employed in large-scale experimental campaigns, with Q-values ranges from 2039 keV for ^{76}Ge to 2527 keV for ^{130}Te. Higher Q-values exist for double-beta-decay candidate nuclei such as ^{150}Nd (3371 keV), ^{100}Mo (3034 keV), ^{82}Se (2995 keV) and ^{96}Zr (3350 keV). The incorporation of these isotopes in detector-ready materials is being explored for future efforts. A Q-values larger than $\sim$3 MeV would place the $0\nu\beta\beta$ energy Region Of Interest (ROI) above the energy of gamma rays from nearly all naturally occurring radioactive isotopes.

1.4.3 Background sources

As mentioned before, the control of the background is a crucial point of these experiments. All the background sources need a specific discussion which is presented in the following.

1.4.3.1 Natural radioactivity

^{238}U and ^{232}Th are the progenitors of two common radioactive chains present in nature, which generate background directly or through their radioactive daughters. Cosmogenic activated nuclei, cosmic muons and neutrons are also sources of background.

Cosmic muons: the flux of μ's on the earth surface is about one per square centimeter per minute. Muons give a continuum in the energy spectrum. Running the experiment in underground conditions reduces the cosmic ray flux by several orders of magnitude. Active shields are added to further exclude muons and radioactivity from secondary interactions.

Neutrons: this background source is particularly insidious for an experiment for rare event search. Neutrons can contribute with two mechanisms: the first one is the activation of the detector materials of the experimental set-up by cosmic neutrons, the second is due to nuclear reactions with the prompt emission of high energy γ's during the measurement. The cosmogenic activation produces long-lived radioisotopes whose subsequent decay can contribute to the background in the ROI. The activation can be reduced storing the material underground. The high energy nuclear reaction induced by the environmental neutrons radioactivity can be reduced with a dedicated shield with a large neutron cross section.

^{238}U and ^{232}Th far from the detector: in this case, the radionuclides of these chains can contribute only with γ's. A proper shield is necessary. The highest energy line is the 2615 keV of the ^{108}Tl decay from the ^{232}Th chain. Compact detectors can be surrounded with high purity high Z materials; lead is commonly used. Large detectors, like scintillators, use active veto surrounding the detector or the outer region of the detector itself.
Another product of these chains is radon. It can be produced outside, in rocks for instance, then migrate to the atmosphere. The half life of ^{222}Rn is about 3 days. After the decay its daughter can attach to air particles and can be transported inside the shield, attach to the materials surface or be diluted inside the liquid detectors.

^{238}U and ^{232}Th near the detector: in this case β, γ and α particles can reach the detector. A careful control of methods, material selection and purification must be performed.

1.4.3.2 $2\nu\beta\beta$ and its pileup in the detectors

The end point of the $2\nu\beta\beta$ spectrum can contribute substantially to the background in the ROI if the energy resolution of the experiment is not good enough. It is possible to demonstrate that for a detector with a good energy resolution (<1%) the end point $2\nu\beta\beta$ contribution is negligible with respect to the $0\nu\beta\beta$ for $m_{\beta\beta}$ in the inverted hierarchy region.
On the contrary, for slow detectors which study an isotope with a relatively short half life for the two neutrino mode, accidental pileup of $2\nu\beta\beta$ events can produce a contribution to background in the ROI at a detectable level, thus limiting the sensitivity of an experiment. In fact, two events produced in the same detector by two random $2\nu\beta\beta$

decays within a time window smaller than the typical time response of the detector can produce a signal that is not distinguishable from the single pulse potentially populating the ROI.

1.4.4 International scenario

The current most sensitive experiments on $0\nu\beta\beta$ are GERDA, CUORE, KamLAND-Zen and EXO, which investigate the ^{76}Ge, ^{130}Te and ^{136}Xe isotopes respectively 1.5.
At present, upgrades of these searches are in preparation or the data-acquisition phase is just starting. Due to the difficult task to estimate precisely the final measurement condition and background, they report only the scale of the half lives of the investigated isotopes that would give a positive result. If the reported half lives are converted into the effective Majorana neutrino mass, using the most favourable matrix element, those improved experiments will investigate values of $m_{\beta\beta}$ close to the inverted hierarchy region (fig:1.14)
In future, the so called next generation experiments aim to explore completely the

$0\nu\beta\beta$ decay	experiment	$T^{2\nu}_{\frac{1}{2}}$ y	$m_{\beta\beta}$ eV
^{76}Ge$\rightarrow^{76}$Se	GERDA [28]	$>2.1\times10^{25}$	<0.22–0.64
^{130}Te$\rightarrow^{130}$Xe	Cuoricino [29]	$>2.8\times10^{24}$	<0.32–1.2
^{136}Xe$\rightarrow^{136}$Ba	EXO [30]	$>1.1\times10^{25}$	<0.2–0.69
	KamLAND-Zen [31]	$>1.9\times10^{25}$	<0.15–0.52

TABLE 1.5: Recent 90% C.L. experimental lower limits on $T^{2\nu}_{\frac{1}{2}}$ and corresponding upper bounds for $m_{\beta\beta}$ taking into account the NME theoretical uncertainties in Tab:1.2.

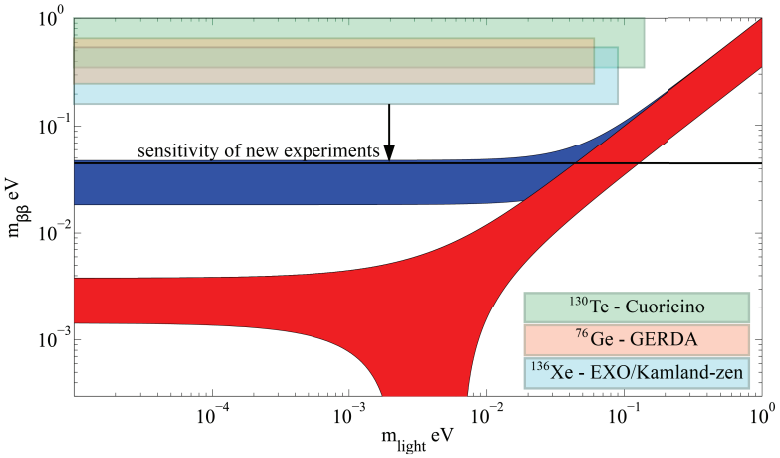

FIGURE 1.14: The explored values of the $m_{\beta\beta}$ are highlighted for the three most investigated isotopes. The black line represents roughly the present sensitivity reported with the most favourable NME indicated in tab:1.2.

inverted hierarchy region. This thesis will set the grounds for a next generation experiment based on scintillating bolometers, which aims to be extremely competitive in this context. To understand what is limiting the measurement, it is thus useful to discuss the result of a $0\nu\beta\beta$ experiment.

1.5 Result interpretation

The search for $0\nu\beta\beta$ consists to the measurement of the energy of the two electrons emitted in the decay process. If $0\nu\beta\beta$ is observed, a peak in the energy spectrum will appear at the Q-value of the nuclear reaction. The number of counts in the peak, n_{obs}, will be a measurement of the half life of the process:

$$T^{0\nu}_{\frac{1}{2}} = \ln(2)\frac{N_{\beta\beta}}{n_{obs}}t\epsilon \tag{1.42}$$

where $N_{\beta\beta}$ is the number of $0\nu\beta\beta$ candidates nuclei under investigation, t is the measurement time and ϵ is the efficiency. The average number of events registered in an experiment as a function of the unknown $T^{0\nu}_{\frac{1}{2}}$ value is thus

$$n_{obs} = \ln(2)\frac{N_a M a}{m_m T^{0\nu}_{\frac{1}{2}}}t\epsilon \tag{1.43}$$

with N_a the Avogadro number, a the isotopic abundance, m_m the molar mass and M the total mass of the $0\nu\beta\beta$ candidate isotope. Background contributes to the measurement of n_{obs} and the experimentalist aims to report the most credible value of $T^{0\nu}_{\frac{1}{2}}$ with an error.
The outcome of a measurement is $n_{obs} = n_0 + b$, a positive integer number with a poissonian distribution. n_0 is the number of true events and b the number of background counts. The mean μ of n_0 is the quantity that we want to determine. The statistical analysis of these processes is a difficult task when the obtained result is in the limit of the sensitivity of the experiment.

From eq:1.32, the effective Majorana neutrino mass will be:

$$m_{\beta\beta} = \frac{1}{M^{0\nu}\sqrt{G^{0\nu}T^{0\nu}_{\frac{1}{2}}}} \tag{1.44}$$

where $T^{0\nu}_{\frac{1}{2}}$ is the result of the measurement

$$T^{0\nu}_{\frac{1}{2}} = \ln(2) \times \frac{N_A M a}{m_{mol}} \times \frac{\epsilon t}{\mu}. \tag{1.45}$$

where $\frac{N_A M a}{m_{mol}}$ is the number of $0\nu\beta\beta$ candidate atoms, ϵ is the efficiency, t the time of the measurement and μ the corresponding measured rate.

1.5.1 Experimental reported values

In a neutrinoless double beta decay experiment, there are three different sensitivity values reported: two are given before the experiment is performed and the third one corresponds to the experiment result. The sensitivity can be expressed equally in terms of half life or effective Majorana mass.
Once the experiment is planned and its parameters are known (i.e. isotope mass, energy resolution, measurement time...) there are two ways to express the sensitivity:

- **Discovery potential**: Before the measurement, under a reasonable assumption for the background, it gives the minimum value of $T^{0\nu}_{\frac{1}{2}}$ for which a claim of discovery can be stated.
- **The exclusion limit on** $m_{\beta\beta}$ (Sensitivity): Assuming the measurement gives a negative result, it gives the smaller value of $m_{\beta\beta}$ that will be excluded. It corresponds to the average of the upper limits of the possible negative outcome results weighted on their probability.

We may decide to express the discovery potential in terms of half life because it is the value which is measured by the experiment; the exclusion limit on the contrary is often shown as the potential of the experiment in neutrino physics and the half life is commonly translated in the effective Majorana mass.
When the experiment is performed, considering the n_{obs} outcome, a result is reported in the form:

- **Confidence interval on** $m_{\beta\beta}$: If the measurement gives a positive result, it gives the range of $m_{\beta\beta}$ statistically compatible with the measurement. In case of a negative result, the absence of a lower limit on the effective Majorana mass leads to an exclusion limit.

All of the parameter are obtained with a confidence level.
To compute these values statistic tools are necessary; there exist several approaches to compute them. In this work we recommend a classical conservative approach which uses the Neyman construction of confidence belts proposed by G. Feldman and R. Cousins in 1997 [32].
The calculation with different background limits is discussed in appendix:A.

1.6 Scintillating bolometers based $0\nu\beta\beta$ experiment

The aim of this thesis is to develop scintillating bolometers for the search for $0\nu\beta\beta$.
Based on the previous discussion it is now possible to estimate the sensitivity of a hypothetical experiment with scintillating bolometers made by the $ZnMoO_4$ compound containing the ^{100}Mo candidate isotope. To reach this goal the different background contributions described in sec:1.4.3 have to be estimated. For this purpose we will make some assumptions based on the previous experience on bolometric experiments.
The fraction of the Mo mass contained in $ZnMoO_4$ is η=0.42. The density is ρ = 4.3 g/cm^3.
The CUORE experiment aims to demonstrate the scalability of a bolometric experiment up to the ton scale. In the CUORE experiment the single bolometer module consists in a crystal with a size of 5×5×5 cm^3. Using CUORE as a reference, let's assume the same module size in this estimation.

1.6.1 Background estimation

The scintillating bolometer technique (described in the next chapter) features a full particle discrimination of $e^-/\gamma/\mu$ from α's and neutrons (to be demonstrated in this

thesis, see chapter:6-7).
The chosen candidate isotope is ^{100}Mo for its high Q-value of 3.034 MeV, which is above the natural γ radioactivity. Suppose the experiment runs underground where the muon flux is strongly reduced and the set-up is equipped with an active veto.
The remaining sources of background are some high energy β-decays and the pileup generated by the two neutrino modes.

1.6.1.1 β background

At this energy scale the dominant contribution to the background is due to the β-decay of ^{210}Tl, ^{208}Tl and ^{214}Bi:

- ^{208}Tl β-decay with a Q-value of 5 MeV and a half life of 3 minutes. It belongs to the ^{232}Th chain. This element is the product of the ^{212}Bi α decay (Q-value$\sim$6 MeV) which occurs in 36% of the cases. This background can be reduced with a dedicated analysis on the delayed coincidence.
- ^{214}Bi β-decay with a Q-value of 3.27 MeV with a half life of 20 minutes. It belongs to the ^{238}U chain and ^{226}Ra is the closest long living precursor. This decay mode has a branching ratio of 99.98% to ^{214}Po, which α decays with a very short half life (163 μs) and a Q-value of 7.8 MeV. In a bolometer this creates a mixed $\alpha - \beta$ event which can be identified.
- ^{210}Tl is produced in 0.02% of the cases from ^{214}Bi by the decay of an α particle of about 5.5 MeV. ^{210}Tl is a β emitter with a half life of 1.3 minutes and Q-value of 5.4 MeV. Also in this case a delayed coincidence analysis can be performed to suppress this background.

The bulk contamination of these elements can be suppressed using scintillating bolometer properties and achieving high detector radiopurity. However, the near surface contamination can give a dominant background as the information about the α particle can be lost. With a dedicated cleaning procedure and material selection this contamination can be reduced. An evaluation of this background is performed considering the experience of by the CUORE-0 and Cuoricino experiments [33]. For our purpose let us be conservative and take the largest contamination cited which is $b_{surface} = 0.6 \times 10^{-3} \ \frac{\text{cts}}{\text{keV}\times\text{kg}\times\text{y}}$.

1.6.1.2 Background from $2\nu\beta\beta$ and its pileup

All the other discussed backgrounds could in principle be reduced at a negligible level. On the contrary, the background induced by $2\nu\beta\beta$ is always present as it is due to the $0\nu\beta\beta$ candidate isotope itself. The half life of the two neutrino mode for ^{100}Mo is reported in tab:1.4. There are two background contributions from $2\nu\beta\beta$: the end point of the $2\nu\beta\beta$ spectrum and the random coincidence (pileup) generated by the $2\nu\beta\beta$ mode. The shape of the $2\nu\beta\beta$ electrons energy spectrum is given by the following formula [34]

$$S(T_1, T_2) = (T_1 + 1)p_1F(T_1, Z)(T_2 + 1)p_2F(T_2, Z)(Q - T_1 - T_2)^5 \tag{1.46}$$

where T_i is the kinetic energy of the elecron, $F(T_i, Z)$ is the Fermi function, Q is the total available energy and p is the momentum of the electron. All the energies are

expressed in electron mass units $m_e c^2$. The distribution of the sum of the electron energy ($T = T_1 + T_2$) is then given by

$$S(T) = \int_0^T S(T - T_2, T_2) dT_2 \tag{1.47}$$

If we consider the pileup of two random events of $2\nu\beta\beta$, the resulting energy spectrum $E_p(T)$ is the convolution of $E(T)$ with itself:

$$S_p(T) = \int_0^T S(T - x) S(x) dx \tag{1.48}$$

The two energy spectral densities of the $E(T)$ and $E_p(T)$ are shown in fig:1.15. The spectrum is obtained with the Primakoff-Rosen approximation [35] of the Fermi function $F(T, Z) \sim \frac{T+1}{p}$. This simplifies eq:1.46 to

$$S(T_1, T_2) \approx (T_1 + 1)^2 (T_2 + 1)^2 (Q - T_1 - T_2)^5 \tag{1.49}$$

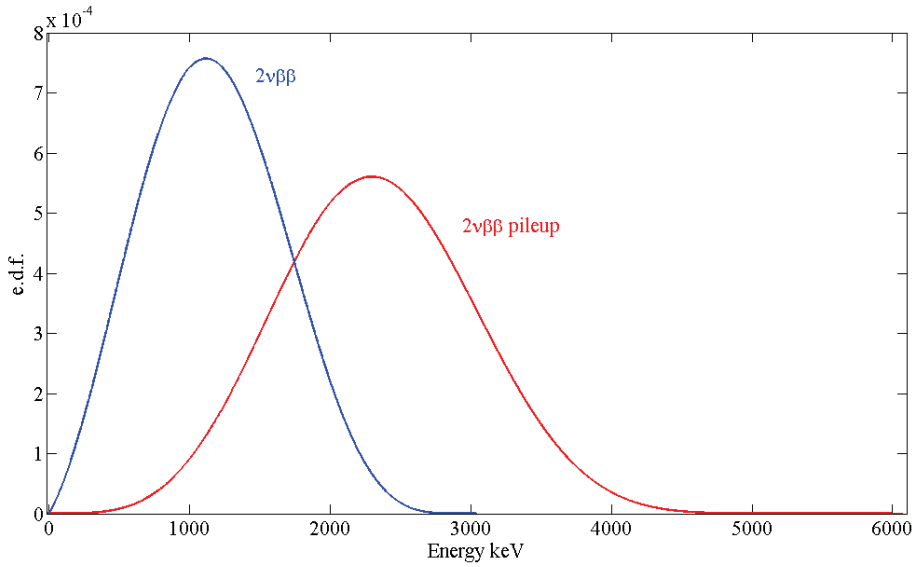

FIGURE 1.15: Energy spectrum density of the $2\nu\beta\beta$ mode (blue) and energy spectrum density of the pileup due to random coincidence (red) for ^{100}Mo.

The end point of the $2\nu\beta\beta$ spectrum: It contributes substantially to the background in the ROI as the energy resolution of the experiment becomes larger. However for a detector with a very good energy resolution (as appreciable in fig:1.15) the rate in the ROI becomes very small. The fraction of events in a ROI of 10 keV around the Q-value is $\epsilon = 5.1 \times 10^{-14}$ which is negligible with respect the other background contributions.

The pileup of the $2\nu\beta\beta$ mode: A bolometer has a slow response and if the pileup occurs in a time window shorter than the characteristic time response it is impossible to distinguish it from a single event. Let us consider 5 ms as the minimum time τ between two events to reject them as pileup. The rate of two events occurring simultaneously within the time τ is

$$R_{pileup}(N, \tau) = N(1 - e^{-N\tau}) \approx N^2 \tau \tag{1.50}$$

where N is the rate of $2\nu\beta\beta$ which is equal to $N = \frac{\ln(2)}{T^{2\nu}_{\frac{1}{2}}}$=1.94×10^{-2} Bq/kg of ^{100}Mo. The fraction of events in the ROI is $\epsilon = 3.4 \times 10^{-4}$ keV^{-1}. In a cubic crystal of $ZnMoO_4$ enriched at 100% in ^{100}Mo with a side of 5 cm the pileup background around the Q-value is:

$$b_p = \left(\frac{\ln(2) V \rho a N_A}{T^{2\nu}_{\frac{1}{2}} m_{mol}} \right)^2 \epsilon\tau = 1.1 \times 10^{-3} \frac{\text{cts}}{\text{keV} \times \text{y} \times \text{crystal}} \tag{1.51}$$

1.6.2 Sensitivity and discovery potential

Based on these background estimations, we calculated the sensitivity and the discovery potential of three different experiment sizes: one small detector using 4 $Zn^{100}MoO_4$ crystals as scintillating bolometers; one medium made by 20 crystals; and a large one based on 1000 $Zn^{100}MoO_4$ crystals. The explicit calculation is described in appendix:A.3. Tab:1.6 reports the calculated sensitivity of the three experiments. In analogy with the present limit on $m\beta\beta$ reported in fig:1.14, fig:1.16 shows the sensitivity of those hypothetical experiments. The black arrow represents the present best limit; even with conservative assumptions on the background, an experiment based on this technique will be very competitive.

Number of cristals	mass of ^{100}Mo kg	$T^{0\nu}_{\frac{1}{2}}$ Discovery [10^{25}y]	$m_{\beta\beta}$ Discovery [meV]	$T^{0\nu}_{\frac{1}{2}}$ Sensitivity [10^{25}y]	$m_{\beta\beta}$ Sensitivity [meV]
4	0.903	0.39	168–466	0.74	122–339
20	4.515	1.32	92–253	2.66	64–179
1000	225.75	14.7	27.5–76	27.8	20–55

TABLE 1.6: Sensitivity at 90% C.L. of experiments based on $ZnMoO_4$ scintillating bolometers searching for $0\nu\beta\beta$ of ^{100}Mo. The assumed background is discussed in the text. The live time is 5 y and the energy window 10 keV.

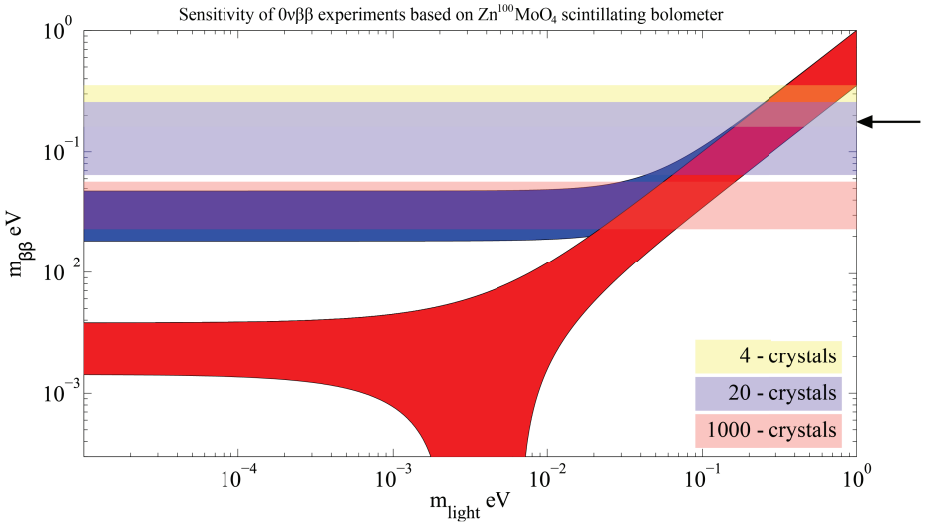

FIGURE 1.16: Sensitivity range to the effective Majorana mass for three experiments based on $Zn^{100}MoO_4$ scintillating bolometers under several hypotheses (see text). The black arrow sets the best limit on $m_{\beta\beta}$ achieved with the present technology.

1.7 Conclusion

The neutrinoless double beta decay is a powerful tool to distinguish the nature of the neutrino particle. The measurement of this rare process is still out of reach of the present technology. In this first chapter we focused on the sensitivity of an experiment which aims to measure this process.
In this thesis we will present the scintillating bolometer technique as a competitive technology for a next generation experiment on $0\nu\beta\beta$. We have started calculating the sensitivity to the effective Majorana neutrino mass for three hypothetical experiments of different size with scintillating bolometers. To approach the problem of the sensitivity calculation, we assumed typical parameter values commonly obtained with this technique. As we have seen, an experiment with these characteristics can easily reach the present forefront in the field.
The sources of background limiting these hypothetical experiments are the random coincidences of the $2\nu\beta\beta$ decay mode. The rate of this background is proportional to the energy resolution and to the time response of the detector.
We will see in the following of the thesis that:
– the capacity of ^{100}Mo-based scintillating bolometers of rejecting α background and achieving high internal radiopurity is confirmed.
– the dominant source of background i.e. the random coincidence of $2\nu\beta\beta$ events, can be significantly reduced with respect to the present evaluation.

Chapter 2

Scintillating bolometers

In this chapter, the bolometric technique and the scintillating bolometers will be briefly presented. Bolometers are Low Temperature Detectors (LTD) and they can be used to search for $0\nu\beta\beta$ following the calorimeter approach (sec:1.4.1). When a particle releases its energy in the bolometer, its detection is mediated by phonons, the quasi-particles associated to lattice vibrations. First conceived as perfect calorimeters, bolometers were proposed for the search for $0\nu\beta\beta$ by E. Fiorini and T.O. Niinikoski in 1984 [36].
In the first part of this chapter, the components of a bolometer, a simple thermal model, and the detector response will be discussed.
The second part of this chapter is more focused on the scintillating bolometers, showing how it is possible to reduce the background[1] events (the ones delivering an energy close to that of the studied process) with respect to the standard bolometric technique.

2.1 Bolometer detectors

A bolometer, which should be more properly defined as a Phonon-Mediated-Detector (PMD), is a simple and very efficient detector, in which almost the whole deposited energy is converted into phonons. If they are compared with other types of calorimetric detectors where the signal is mediated by different mechanisms, the advantage becomes immediately clear. Let's consider, for example, a ionizing particle which deposits its whole energy. In case of a charge mediated detector, like diode semiconductor detectors, only 30% of the particle energy is converted into a signal. In a scintillator the light output efficiency is at most a few %. Since the energy resolution is dominated by the fluctuation of the fraction of the energy useful for the detection, bolometers are by definition in the best position, as no fluctuation is expected in the ideal case.
Bolometers are simple devices composed by a few elements: an energy absorber, a thermal sensor (which should be more properly defined a phonon sensor) and a thermal link to the heat bath. A simple scheme is reported in fig:2.1. After a particle interaction in the absorber medium, the released energy is converted into phonons, determining, in case of full thermalization, a temperature increase ΔT, which is proportional to the energy deposited in the absorber:

$$\Delta T = \frac{E}{C} \tag{2.1}$$

[1] We will use instead 'noise' to indicate the effects which cause a degradation of the energy resolution.

where E is the deposited energy and C the heat capacity of the detector. To enhance the thermal signal, a small heat capacity is needed and so bolometers work at very low temperatures, in the 10-30 mK range. Issues arise to make them operational: they require sophisticated cooling systems and maintaining them working for a long time is a complicated task. This kind of detectors has, potentially, an excellent energy resolution,

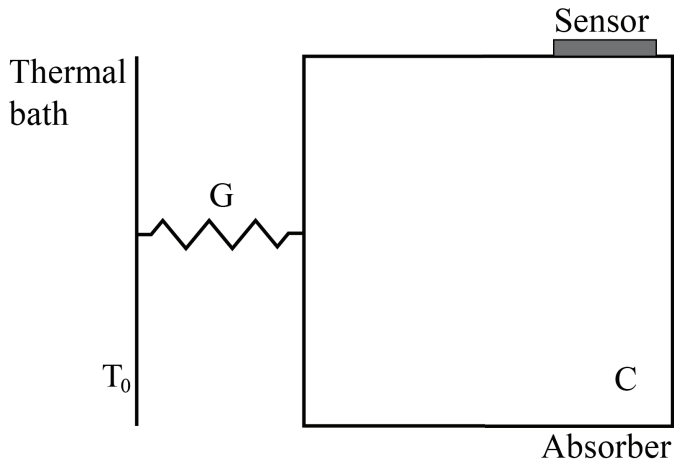

FIGURE 2.1: A bolometer could be schematically summarized as an absorber and a thermal sensor linked to a thermal bath with a thermal link.

thanks to the fine energy granularity of the detection mediators. Let us consider an impinging particle which releases its whole energy, which is fully converted into vibration modes (phonons). The sensor collects and converts them into an electrical signal. In analogy with the conventional detection techniques, the limit to the energy resolution is given by the statistical error associated with the mediators counting, which is the poissonian fluctuation of their number. The energy needed to produce a thermal phonon is $w = k_b T$, with k_b the Boltzmann constant. The number of produced phonons is

$$N = \frac{E}{w}. \tag{2.2}$$

The energy resolution is proportional to $\Delta N = \sqrt{N}$. Thus the intrinsic energy resolution ΔE_{FWHM} is

$$\frac{\Delta E_{FWHM}}{E} = 2.35\frac{\Delta N}{N} = 2.35\sqrt{\frac{Fw}{E}} \tag{2.3}$$

where F is the Fano factor[2] which conservatively is $F = 1$ for bolometers. For a 1 keV particle, $F = 1$ and a temperature $T = 20$ mK, the resulting ΔE_{FWHM} is 98 meV.
This picture, however, is very naive and does not take into consideration what is limiting the energy resolution of the detector that is the internal energy fluctuations in the absorber itself. These fluctuations follow a statistics similar to the particle case. The energy stored in the absorber is of the order of

$$E \simeq N \cdot K_b T \simeq C \cdot T \tag{2.4}$$

[2]The Fano factor is a measurement of the variance in the number of carriers produced in materials by ionizing radiation interactions [37].

Then the internal energy fluctuations ΔE will be:

$$\Delta E \simeq \sqrt{N} \cdot K_b T = \sqrt{N K_b^2} T = \sqrt{C(T) k_b} T \tag{2.5}$$

which is in general larger than the resolution associated to the particle absorption and independent from the particle energy. The same formula can be derived in a more rigorous way by using the classical statistical mechanics. The intrinsic resolution is then dominated by the statistical fluctuations in the thermal energy of the absorber.
Considering 500 g of $ZnMoO_4$ at 20 mK, the resulting ΔE_{FWHM} is $2.355 \times \Delta E = 12.7$ eV to be compared with the 98 meV of the particle case.

2.1.1 The absorber

As discussed above, the most relevant parameter of a bolometer is the overall heat capacity that has to be small in order to get large and fast signals in response to the energy deposit. The requirement of a low heat capacity is the only constraint on the bolometer absorber. For the $0\nu\beta\beta$ search, the efficiency is a crucial parameter: with a bolometer, it is possible to build a detector made of the source itself. The heat capacity C(T) of materials at low temperatures can be expressed as the sum of the crystal lattice heat capacity $C_r(T)$ and the electrons heat capacity $C_e(T)$. If the absorber is a dielectric and diamagnetic crystal, only the lattice heat capacity contributes, which is described by the Debye law and is given for 1 mole of material and in the limit of vanishing temperature by

$$C_r(T) = \frac{12\pi^4}{5} N_A k_b \left(\frac{T}{\Theta_D} \right)^3 \tag{2.6}$$

where Θ_D is the Debye temperature that characterizes the crystal.
If the material is a conductor, the electron gas in the conduction band contributes with a heat capacity proportional to the temperature and is given, for 1 mole of material and in the limit of vanishing temperature, by

$$C_e(T) = \pi^2 Z R \frac{T}{\Theta_D \Theta_F} \tag{2.7}$$

where Θ_F is the Fermi temperature, Z is the number of conduction electrons per atom and R the gas constant.
At low temperatures the material can be superconductive; in this case, if the temperature is well below the critical temperature T_c[3], the electron heat capacity $C_e(T)$ changes regime and becomes small too:

$$C_e(T) = K_s e^{-2\frac{T_c}{T}} \tag{2.8}$$

with K_s a constant which depends on the material.
Therefore the best materials for bolometer absorbers have to be selected among dielectric and diamagnetic crystals with high Debye temperatures Θ_D or among superconductors with critical temperatures $T_c \gg T_{work}$.

[3] T_c is the temperature of the phase transition to a superconducting regime.

The mechanism of energy release by an impinging particle changes with the particle type. In general, a fraction of this energy is spent in e-h pairs production and the remaining part in the direct excitation of the lattice vibration modes. The produced e-h pairs finally recombine creating thermal phonons as well or exciting luminescent centers. In the second case, part of the initial energy is lost by light emission in case of sufficient transparency of the absorber.
The interaction produces initially the so-called athermal phonons, which are characterized by a thermalization time (from ns to μs depending on the material and temperature). The thermalisation mechanisms are complex and not fully understood yet. Detectors measuring this athermal signal exist and show nice features but this topic is beyond our present discussion.
It is experimentally observed that the quality of the crystal absorber affects the detector performance; in particular impurities can trap the produced e-h pairs storing part of the energy that is lost as far as detection is concerned. Polycrystals affect the phonon propagation making signals position-dependent or the response slow. It is thus important to take care of the crystal quality.

2.1.2 Thermal sensor

The thermal sensor is the component that converts the temperature into an electrical signal. It exploits a physical parameter (resistivity, magnetic field, current...) which depends on the temperature. There exist different sensor options at such low temperatures:

- Neutron Transmutation Doped (NTD) Ge thermistors
- Transition Edge Sensors (TES)
- Metallic Magnetic Calorimeters (MMC)

Each of them has advantages and disadvantages and their choice depends on the application. Our bolometers are based on the NTD Ge thermistor readout on which we will focus.
A parameter characterizing the thermistor performance is the sensitivity defined as:

$$A = \left| \frac{d\log(R(T))}{d\log(T)} \right| = \frac{T}{R}\frac{dR(T)}{dT} \tag{2.9}$$

that measures the ability of the sensor to convert small temperature variations into resistance variations.
High sensitivities can be obtained in a semiconductor with a particular concentration of dopant impurities. The resistivity of a semiconductor decreases with the increase of the concentration of impurities, which can create energy levels just below the conduction band (in case of donor impurities) or just above the valence band (in case of acceptor impurities). Beyond a certain concentration level, defined Metal-Insulator Transition (MIT), the behavior of the doped sample becomes metallic whatever the temperature.
For low dopant concentrations at low temperatures, the carriers are trapped in the valence band leading to an insulator behavior. A particular concentration of dopant does exist, just below the MIT, where the electrons wave functions can overlap between two dopant sites.

In this case, at very low temperatures (T$\ll$ 10 K), the conduction is due to a quantum-mechanical tunneling effect through the potential barriers separating the dopant sites. This conduction regime is named Variable Range Hopping (VRH), and is characterized by hopping processes mediated by phonons between two energetically separated sites (fig:2.2).

In these particular conditions, the dependence of the resistivity $\rho(T)$ on the temperature

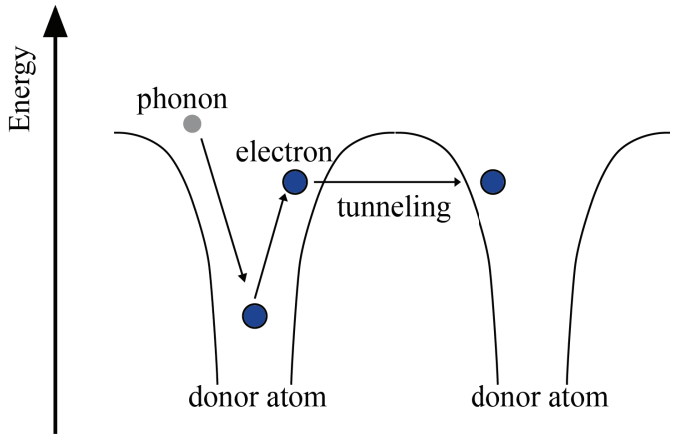

FIGURE 2.2: Simple scheme of the Variable Range Hopping mechanism. The phonon transmits its energy to the electron that can 'jump' to the near dopant site.

is given by:

$$\rho(T) = \rho_0 \exp\left(\frac{T_0}{T}\right)^{\gamma}, \tag{2.10}$$

where γ is equal to $\frac{1}{2}$ for compensated samples and ρ_0 is the resistivity. The sensors used for the bolometers described in chapters 5-6-7 are NTD Ge thermistors and they are characterized by two parameters, T_0 and $R_0 = \frac{l}{s}\rho_0$, which have to be experimentally measured. These Ge devices are defined Neutron Transmutation Doped as their doping and compensation are achieved by the formation of new atomic species deriving from nuclear decays, that follow nuclear reactions induced by thermal neutrons.

The usual method to read out the resistance of a NTD thermistor is to fix the current flowing through it and to register the voltage drop across it. The circuit which provides the current to the sensor is named bias circuit: a simple example is shown in fig:2.3. In this scheme, R_L represents the load resistance, with $R_L \gg R_{NTD}$ to assure a constant current supply even if R_{NTD} varies. Considering the basic circuit shown in fig:2.3, the relationship between the voltage ΔV, the parameters of the thermistor and the deposited energy E is given by:

$$\Delta V = \frac{2R_L}{2R_L + R} \times V_{bias} \times A\frac{\Delta T}{T_b} \approx \frac{E}{CT_b} A\sqrt{PR} \tag{2.11}$$

where T_b is the bolometer temperature, P the electrical power dissipated by the bias, and A is the logarithmic sensitivity of eq:2.9, which for NTD thermistors is:

$$A = \gamma\left(\frac{T_0}{T}\right)^{\gamma} \tag{2.12}$$

.

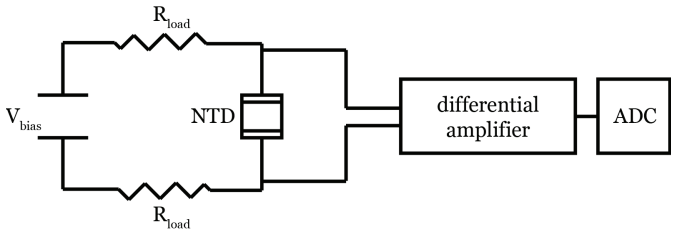

FIGURE 2.3: NTD polarization circuit.

2.1.3 Bolometer signal output

Many thermal models of a bolometer were studied, but none of them is actually capable to reproduce exactly the bolometer output. The differential equation system, resulting from the full modelisation of the bolometer in all its components, is not linear; the numerical solution reproduces only the general lines of the detector behavior.
Here we discuss the thermal signal in its essential elements in order to understand the pulse shape of a bolometer signal, which will lead to a dedicated analysis procedure described in Chapter 4.

2.1.3.1 Easy picture

Let's consider the monolithic model (fig:2.1) where the bolometer is described by an element of heat capacity C and a thermal link with thermal conductance $G(T)$.
Consider to have two systems with temperatures T_1 and T_0 respectively, coupled by a thermal conductance $G(T)$. The heat flows through the conductance from the higher temperature stage to the lower temperature stage transporting a power:

$$P = \int_{T_0}^{T_1} G(T)dT. \tag{2.13}$$

Being the thermistor polarized, there is a constant Joule dissipation in the detector. In a static equilibrium the temperature of the bolometer stands at T_b, higher than the thermal bath temperature T_0. Considering $|T_b - T_0| \ll T_0$ such that G is constant in this temperature range, T_b has to satisfy eq:2.13, which becomes

$$P = \int_{T_0}^{T_b} GdT = G(T_b - T_0). \tag{2.14}$$

Now suppose that a particle releases energy in the crystal; then the temperature $T(t)$ increases before relaxing again at T_b. The temperature variation can be calculated imposing the energy conservation in the time dt

$$Pdt - CdT = G(T(t) - T_0)dt \quad \Rightarrow \quad P - C\frac{dT}{dt} = G(T(t) - T_0) \tag{2.15}$$

If the system started in a static condition at T_b, the temperature variation is $\Delta T = T(t) - T_b$, and it obeys the following:

$$\begin{aligned} P - C\frac{d\Delta T}{dt} &= G(T(t) - T_s) + G(T_b - T_0) \\ C\frac{d\Delta T}{dt} &= G(T(t) - T_s) \end{aligned} \tag{2.16}$$

The solution of eq:2.16 with the initial condition $\Delta T(0) = E/C$ is

$$\Delta T(t) = \frac{E}{C} e^{-\frac{t}{\tau}} \quad \text{with} \quad \tau = \frac{C}{G} \tag{2.17}$$

This extremely simplified model allows a few considerations: after a particle interaction, the pulse starts from an equilibrium condition. The thermal relaxation to the equilibrium is in general described by an exponential law and the characteristic time is of the order of C/G.

2.1.3.2 Non-easy picture

It is instructive to analyze a more complicated model, where all the components are treated separately. In this case a system of differential equations describes the dynamic behavior. A scheme of this model is represented in fig:2.4.

The bolometer is treated as a composite device and it is divided in three parts: two

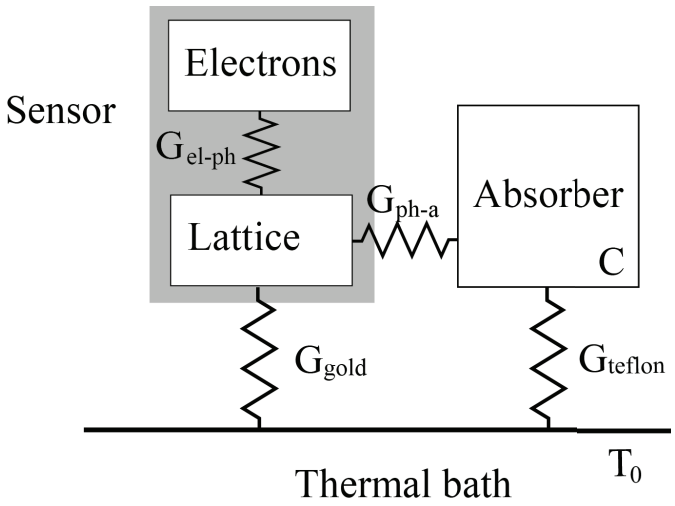

FIGURE 2.4: Composite thermal model with three nodes.

describe the sensor and the last one the absorber. In fact, at low temperatures the VRH does not describe entirely the thermistor behavior. A phenomenological model with no clear physics basics has been proposed, known as Hot Electron Model (HEM) [38].
In order to explain the VRH conduction non-linearity excess, HEM introduces a thermal conductance, G_{el-ph}, between phonons in the thermistor lattice and electrons.
The absorber is held inside the holder by means of teflon clamps, whose goal is to provide a mechanical support and a negligible thermal conductance G_{teflon}. In the bolometers described in this work, the thermal link to the thermal bath is dominated by the gold electric contacts, described by G_{gold}, which are coupled to the lattice of the thermistor.

The sensor is glued to the absorber introducing one more conductance, G_{ph-a}.
In this scheme, neglecting G_{teflon}, the temperature at the equilibrium is obtained imposing that the Joule power dissipation flows through G_{gold} and G_{el-ph}. To solve the dynamical case, as we did before , it is enough to impose the energy conservation in all the nodes:

$$\begin{cases} C_e \frac{dT_e(t)}{dt} + G_{el-ph}(T_e(t) - T_l(t)) = 0 \\ C_l \frac{dT_l(t)}{dt} + G_{el-ph}(T_l(t) - T_e(t)) + G_{glue}(T_l(t) - T_a(t)) + G_{gold}(T_l(t) - T_l(0)) = 0 \\ C_a \frac{dT_e(t)}{dt} + G_{glue}(T_a(t) - T_l(t)) = 0 \end{cases} \tag{2.18}$$

A particle interaction with the absorber introduces, as before, an initial condition $\Delta T_a = E/C_a$.
These equations are valid in the approximation of a small perturbation of the working temperature and can be solved under the assumption that the heat capacity of the lattice system is negligible: $C_l \ll C_e < C_a$. The system has to be solved for $\Delta T = T_e(t) - T_e(0)$, which describes the temporal evolution of the electron temperature, which is the measured one. We obtain:

$$\Delta T(t) = K \frac{E}{C_a} \left(e^{-\frac{t}{\tau_1}} - e^{-\frac{t}{\tau_2}} \right) \tag{2.19}$$

where K, τ_1 and τ_2 are constants depending on the heat capacities and conductances with $\tau_2 < \tau_1$ and $0 < K < 1$.
The resulting equation shows that unlike the simplified model, the temperature change is not instantaneous but the thermal pulse needs a characteristic time to reach its maximum; this time is related to the experimental parameter conventionally defined 'rise time' which is the time required to the pulse to rise from 10% to 90% of its maximum. The decay time, which is asymptotically given by τ_1, is related to the absorber heat capacity and its coupling to the thermal bath as in eq:2.17.

2.1.4 Non linearity

All the approximations have been applied to linearise the system and solve it analytically: this works pretty well for small signals. When the signal is so large that the approximation $\Delta T \ll T_0$ is not valid, the detector shows non linearities in the response. The amplitude of the pulse, defined as the maximum ΔV measured across the sensor, is no longer proportional to the deposited energy. To correct the output amplitude we propose here a procedure which takes into account three factors.

2.1.4.1 NTD non linearity

First we consider the bias current i constant across the thermistor so that

$$\Delta V = (R(T_b) - R(T_{max}))\, i. \tag{2.20}$$

Considering the equations for the NTD resistivity (eq:2.10), eq:2.20 can be written as

$$\Delta V = \left[R_0 \left(\exp\left(\frac{T_0}{T_b}\right)^{\frac{1}{2}} - \exp\left(\frac{T_0}{T_{max}}\right)^{\frac{1}{2}} \right) \right] i; \tag{2.21}$$

Substituting T_{max} with $T_b + \Delta T$ one obtains:

$$\begin{aligned} \Delta V &= \left[R_b - R_0 \exp\left(\frac{T_0}{T_b + \Delta T}\right)^{\frac{1}{2}} \right] i \\ &= \left[R_b - R_0 \exp\left(\frac{T_0}{T_b + E/C}\right)^{\frac{1}{2}} \right] i \end{aligned} \tag{2.22}$$

2.1.4.2 Heat capacity dependence on the temperature

Here we consider the dependence on the temperature of the heat capacity; as before, we assume that all the energy E is deposited in the absorber.
The absorber considered in this work is dielectric, with a heat capacity C_a which satisfies eq:2.6:

$$\frac{dE}{dT} = C(T) \quad \text{with} \quad C(T) = c_0 T^3 \tag{2.23}$$

Therefore, T_{max} has to satisfy

$$E = \int_{T_b}^{T_{max}} c_0 T^3 dT = \frac{c_0}{4}\left(T_{max}^4 - T_b^4\right) \quad \Rightarrow \quad T_{max} = \left(T_b^4 - \frac{4}{c_0}E\right)^{\frac{1}{4}} \tag{2.24}$$

Then ΔV is equal to:

$$\Delta V = \left[R_b - R_0 \exp\left(\frac{T_0}{\sqrt[4]{T_b^4 - \frac{4}{c_0}E}}\right)^{\frac{1}{2}} \right] i \tag{2.25}$$

From eq:2.25 we can explicitly find an equation which corrects the output taking into account the non linearity of the NTD and the dependence of the heat capacity on the temperature, which is

$$E = \frac{c_0}{4}\left\{ \left[\frac{T_0}{\left[\ln\left(\frac{R_b}{R_0} - \frac{\Delta V}{iR_0}\right)\right]^2} \right]^4 - T_b^4 \right\} \tag{2.26}$$

We have used successfully eq:2.26 as a calibration law with high sensitivity non-linear detectors. This is a rough approximation in the picture of a monolithic model.
From eq:2.19, which describes the thermal response for a composite bolometer, ΔT depends not only on C_a but also on K, a combination of heat capacities and conductances. Let's propose a more general equation where the dependence on temperature assumes a

free parameter in the power law:

$$E = \int_{T_b}^{T_{max}} a_0 T^\alpha dT = \frac{c_0}{\alpha+1}\left(T_{max}^{\alpha+1} - T_b^{\alpha+1}\right)$$
$$\Rightarrow\ E = \frac{a_0}{\alpha+1}\left\{\left[\frac{T_0}{\left[\ln\left(\frac{R_b}{R_0} - \frac{\Delta V}{iR_0}\right)\right]^2}\right]^{\alpha+1} - T_b^{\alpha+1}\right\} \tag{2.27}$$

where a_0 is a new constant. Even if this approximation appears very simplified, a good phenomenological agreement is observed.

2.1.4.3 Electro-thermal feedback

We model the sensor as two separate systems: the electron system and the lattice system, thermally connected through G_{el-ph}. The temperature of the electrons is determined by Joule heating and the heat leak to the lattice. When an event heats the bolometer, the resistivity of the NTD decreases, reducing also the Joule power dissipation.
The return to the equilibrium is then described by

$$-C_e\frac{d\Delta T}{dt} = -\frac{P_e A}{T}\Delta T + G_{el-ph}\Delta T \tag{2.28}$$

where A is the sensitivity (eq:2.9). The first term on the right side is the effect of reduced Joule heating and the second term is the effect of the increased heat flow. This effect can be translated to a G_{el-ph}^{eff}

$$-C_e\frac{d\Delta T}{dt} = \left(G_{el-ph} - \frac{P_e A}{T}\right)\Delta T = G_{el-ph}^{eff}\Delta T \tag{2.29}$$

It is complicated to introduce this effect in an analytical model, because G_{el-ph}^{eff} depends on T even for small ΔT if the sensor is highly sensitive. This effect plays a role in all the parameters describing the pulse shape (eq:2.19).
From the experimental point of view, if the sensor is very sensitive, it can be a source of non linearity because large pulses recover to the equilibrium conditions faster as their amplitude increases.

2.2 Scintillating bolometer detectors

A $0\nu\beta\beta$ experiment based on bolometers is a promising way to investigate this extremely rare process, as this detection technique matches well the requirements of high energy resolution and efficiency. Different dielectric diamagnetic crystals containing a candidate isotope can be chosen as absorbers, so that the source is contained in the detector. This provides not only high efficiency, but also a flexibility in the isotope and compound choice.
The absorber can be selected among the scintillating compounds, which, after a particle interaction, will emit a light flash. This flash, if collected and quantified, can provide a second output channel. These hybrid low temperature devices, which –as we will see– are capable of discriminating particles, are named scintillating bolometers.

2.2.1 Motivation

Background events are an intrinsic limit to the sensitivity of an experiment searching for a $0\nu\beta\beta$ decay. α particles are demonstrated to be the dominant background in the >2.5 MeV energy range, typical Q-values of the most favorable $0\nu\beta\beta$ isotopes.
The feasibility of a large bolometric experiment will be definitely proved by the CUORE detector which will run 998 bolometers of TeO_2. The precursor of CUORE, the Cuoricino experiment, clearly highlighted [39] that an irreducible background level in the energy region of interest is due to α particles from the radioactive nuclides of the uranium and thorium chains, which can contaminate the crystal surfaces and the surrounding materials (as discussed in the first chapter) (fig:2.5). In Cuoricino, this level was equal to $\sim$0.12 $\frac{\text{cts}}{\text{keV}\times\text{kg}\times\text{y}}$ and, thanks to special surface treatments, was reduced to $\sim$ 0.02 $\frac{\text{cts}}{\text{keV}\times\text{kg}\times\text{y}}$ in CUORE-0 [39], the first CUORE like tower operated in the Cuoricino cryostat. The possibility to identify the nature of the interacting particles will reduce the

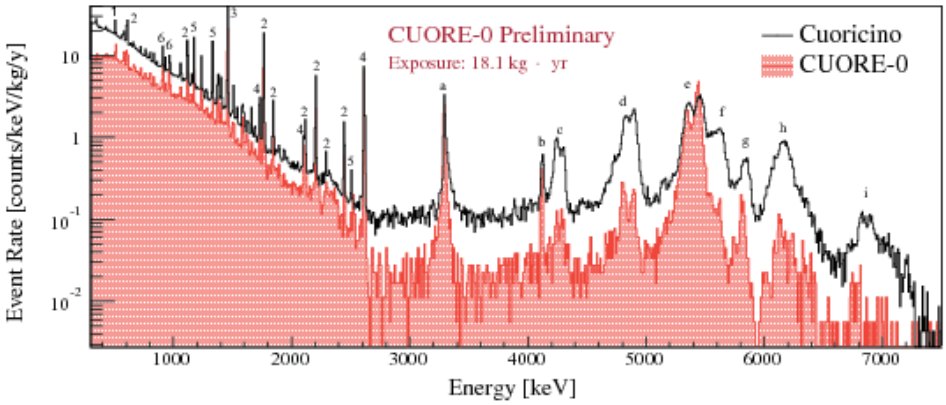

FIGURE 2.5: Cuoricino (line) and CUORE-0 (shaded) background spectra comparison. Only events with a single crystal hit are considered (anti-coincidence mode) [39].

α background contribution increasing significantly the sensitivity of such experiments.

2.2.2 Scintillation mechanisms

The mechanisms leading to light emission in the inorganic crystals are complex and not all of them are fully understood yet. The main mechanism, responsible for the light emission, consists in the de-excitation of electrons in the conduction band bound to impurities, which provide energetic levels in between the valence band and the conduction band. The electron emits a series of photons at low energies not re-absorbed by the medium.
The Light Yield (LY) provides the information about the particle nature. It is defined as the ratio of the light produced by scintillation and the total energy deposited in the absorber:

$$LY \equiv \frac{dL}{dE} \tag{2.30}$$

The discrimination power (DP) of these detectors is due to the fact that α particles have a different LY from β/γ.
The difference in light emission can be phenomenologically explained by the different length of the particle paths inside the crystal. Heavy charged particles release their

whole energy in a smaller volume than β/γ and, given that the activation centers are homogeneously distributed, the way in which they are excited is different. J.B. Birks proposed a semi-empirical formula [40] to quantify this phenomenon:

$$\frac{dL}{dr} = \frac{S\frac{dE}{dr}}{1 + kB\frac{dE}{dr}} \tag{2.31}$$

where S is the scintillation efficiency and kB is the Birks factor, which depends on the concentration of the activation centers.
From eq:2.31 it is possible to distinguish two limit cases. For a particle with a large stopping power like the α ones the limit is

$$\frac{dL}{dr} \approx \frac{S}{kB} \tag{2.32}$$

On the contrary, for light particles with a smaller stopping power like β's and γ's, eq:2.31 can be approximated with

$$\frac{dL}{dr} \approx S\frac{dE}{dr}. \tag{2.33}$$

The Quenching Factor (QF) is defined as the LY_α-to-$LY_{\beta/\gamma}$ ratio:

$$QF = \frac{LY_\alpha}{LY_{\beta/\gamma}} \approx \frac{1}{kB} \tag{2.34}$$

2.2.3 Scintillating bolometers design

The most natural way to read out the emitted light is to use an auxiliary bolometer. In a cryogenic set-up, in the mK temperature range, other devices could be difficult to operate. The material selected as absorber for the light detector in this work is germanium; it is a semiconductor with excellent bolometric properties and, due to the very short absorption length for the scintillating photons, it may be very thin (at 600 nm the absorption coefficient in Ge is 2.4 μm^{-1}).
In order to increase the collection efficiency, the main bolometer and the light detector are located in the same holder close to each other. The surrounding elements are covered with highly reflecting foils (see scheme in fig:2.6).
In this way, different particles depositing the same energy, measured as heat, produce different light signals in the main bolometer. The energy of the measured light is always proportional to the deposited energy with a slope defined by the LY. If the light signals are plotted as a function of the amplitudes of the corresponding heat signals, different amplitude bands are recognizable (fig:2.7). Each point populating the bands in the scatter plot corresponds to a measured event. A high efficiency in photons collection and a more precise measurement of their energy will improve the discrimination power. This effect will be particularly clear at low energies, where the points in which the bands merge will be shifted to a lower energy.
The same information can be shown with the so called Q-plot, where the light signal-to-heat signal ratio, the LY, is plotted as a function of the heat signal (fig:2.8). The

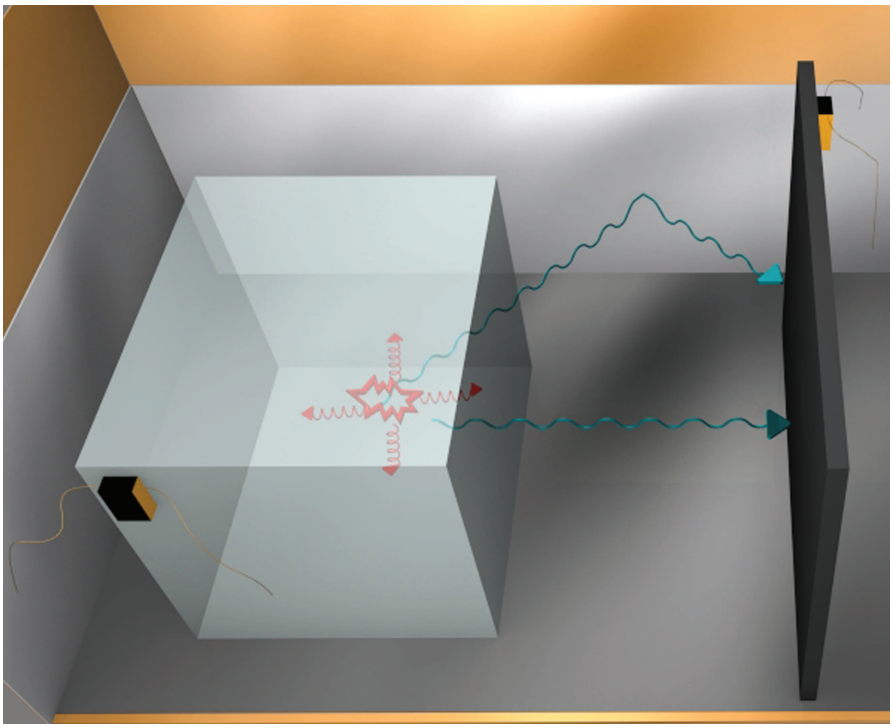

FIGURE 2.6: Scintillating bolometer sketch. The main bolometer (left) and the light detector bolometer (right) are located in a copper frame covered by reflecting foils. The figure shows an interaction inside the main bolometer with the emission of photons and phonons.

separation between the α band and the β/γ band defines the discrimination power:

$$DP \equiv \frac{\left|LY_{\beta/\gamma} - LY_{\alpha}\right|}{\sqrt{\sigma^2_{\beta/\gamma} + \sigma^2_{\alpha}}} \tag{2.35}$$

The LY and the σ are obtained with a gaussian fit of the light-to-heat ratio at the energy of interest. The confidence bands drawn in fig:2.8 can be experimentally calculated by fitting with a gaussian distribution the LY in the energy range of interest. An equivalent analytical calculation can be performed by propagating the errors of the energy measurements (light and heat) to the light-to-heat ratio (LY).

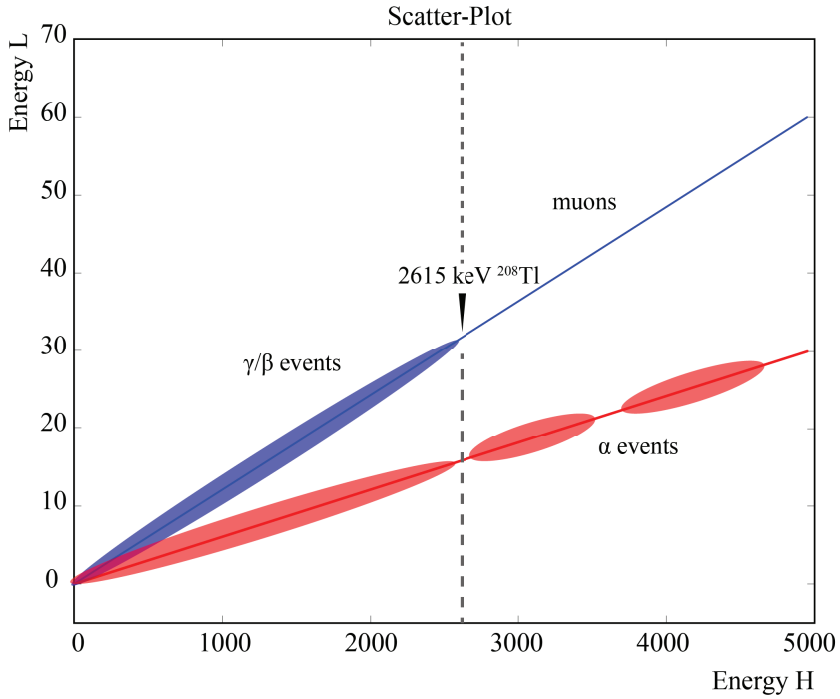

FIGURE 2.7: Example of a scatter plot: the red lines represent α particles and the blue lines β and γ particles.

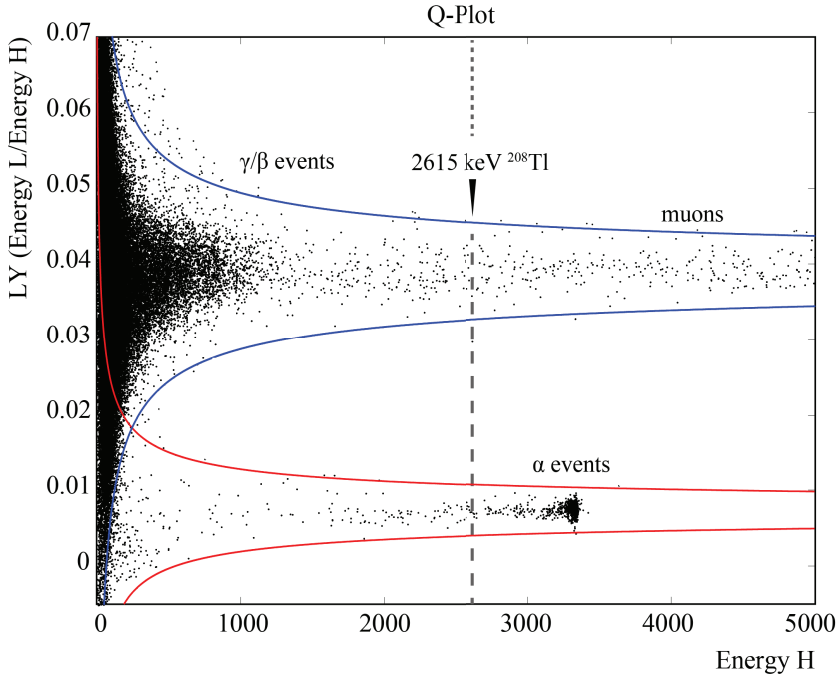

FIGURE 2.8: Example of a Q-plot: each point corresponds to an event, solid lines are the confidence bands (see text).

Chapter 3

Cryogenics setup

To reach very low temperatures, we used a thermodynamic machine, called Dilution Refrigerator (DR). This device allows to cool down large masses at temperatures in the mK range. A cryostat, which is a cryogenic setup housing the dilution refrigerator in its more internal section, appears horribly complicated, intricate and as a fragile mess of tubes. With a bit of experience, it is possible to control it but, because of its delicate working equilibrium, during the periods of running, a cryostat needs constant maintenance and supervision. To reach and maintain such low temperatures, the system has to be wholly isolated from the environment in a vacuum chamber with several screens placed one inside the other.
In this work five different cryogenic systems have been used. The working principle of the cryogenic system will be presented in the first part of this chapter; the second part contains a brief description of each setup.

3.1 Dilution refrigerator concepts

To cool down samples at $T \approx 10$ mK the heat flow from the 300 K stage has to be reduced below the cooling power of the machine. For this reason, the cooling system is maintained in vacuum and several copper screens are implemented to shield the sample from the black-body radiation. The first screen stands at the first cooling stage, which consists of a bath of liquid nitrogen (LN_2 $T = 77$ K); inside this screen there is the Inner Vacuum Chamber (IVC), where the dilution circuit is placed. The IVC is kept at $T = 4.2$ K with a Liquid He bath (LHe).
The base temperature is reached in the lower part of the cryostat by subsequent steps. The coldest point is named Mixing Chamber (MC). Each temperature stage has a copper screen associated.
To go below the LHe temperature the cryostat uses a mixture of two isotopes of helium: ^{3}He and ^{4}He. The mixture which flows in a closed circuit provides the cooling power. This system was proposed for the first time by Heinz London in the early 1950s, and it was experimentally realized in 1964 in the Kamerlingh Onnes Laboratorium at the Leiden University [41].
The working principle is based on the properties of the mixture of the two stable isotopes of helium, for which two phases coexist under particular conditions: the mixture has to be cooled below the tri-critical point at 870 mK and the total ^{3}He concentration

must be larger than 6.5% (fig:3.1). The lighter 'concentrated phase' is rich in ^{3}He, and the heavier 'diluted phase' is rich in ^{4}He. The concentration of ^{3}He in each phase is temperature-dependent. Since the enthalpy of ^{3}He in the two phases is different, the 'evaporation' of ^{3}He from the concentrated phase to the diluted one may provide highly effective cooling. ^{4}He, composing the bulk of the diluted phase, is inert and non inter-

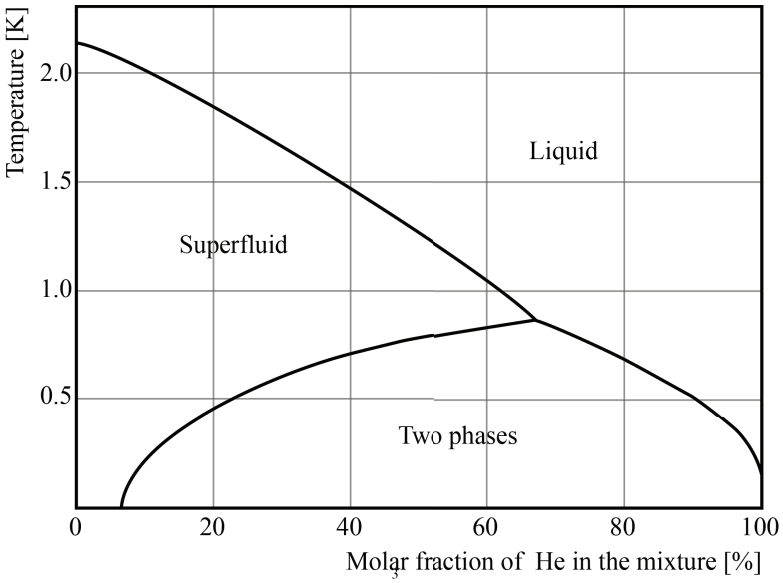

FIGURE 3.1: Phase diagram of the liquid ^{3}He-^{4}He mixtures at the saturated vapor pressure.

acting, and it may be neglected. The evaporation of ^{3}He from the 'liquid' phase to the 'gas' phase cools the sample. Thanks to the different quantum properties of the two isotopes, this process works even at the lowest temperatures because the equilibrium concentration of ^{3}He in the diluted phase is finite, even at zero temperature.
To reach the critical point, the mixture, which is injected starting from room temperature, is thermalized at the first cooling stage, then it passes through an impedance flux, providing a free adiabatic expansion in vacuum and cooling down the mixture through the Joule-Thomson effect. Sometimes (this method was the standard one until a few years ago), a small volume of pumped LHe is injected inside the IVC to thermalize the mixture at $T \approx 1.2$ K; it is called 1K pot. Neither the Joule-Thomson effect nor the 1K pot cool the mixture sufficiently to form the boundary phase. A separation phase occurs when temperatures fall below the tri-critical point. This cooling is provided by the still; the incoming mixture is cooled by the still before it enters the heat exchangers and the mixing chamber (fig:3.2).
During the operations, ^{3}He must be extracted from the diluted phase (to prevent saturation) and re-supplied to the concentrated phase. ^{3}He is pumped away from the liquid surface in the still, where at $\sim$0.6 K ^{3}He preferentially evaporates. The ^{3}He exiting from the mixing chambers is used to cool down the incoming mixture with heat exchangers between the inlet and outlet lines.
The dilution refrigerator has been designed with a two-part external gas handling system. One part (the circulation system) is dedicated to the circulation and handling of the mixture, and the other (the auxiliary system) to auxiliary pumping operations.
In general, every time the refrigerator is cooled down, a hermetic vacuum seal at cryogenic temperatures needs to be made, and a low temperature vacuum feed-through must

be used for the experimental wiring.
Finally, samples are mechanically and thermally connected to the MC.

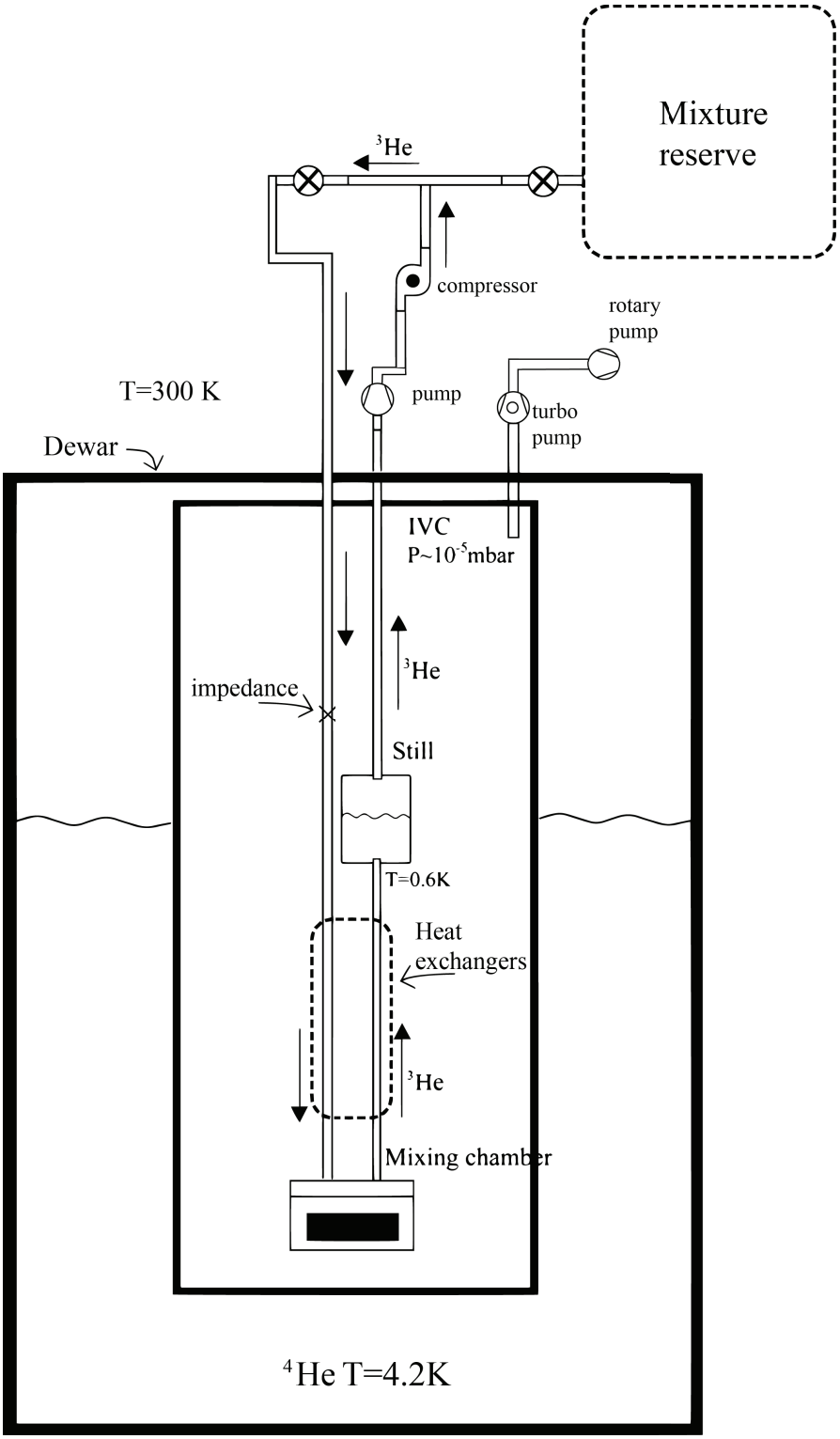

FIGURE 3.2: Scheme of a typical dilution refrigerator.

3.1.1 Wet cryostat

'Wet cryostat' is the name used for dilution refrigerators which use cryo-liquids at the first cold stage. In these systems the IVC is placed inside a LHe bath which provides the first cooling stage at 4.2 K. The two main reasons to have a cold stage at 4 K is to prevent heat supply from outside and to pre-cool the mixture before entering in the heat exchangers. In some case, the liquid He dewar has an additional outer chamber for liquid nitrogen in order to decrease the He consumption.

3.1.2 Dry cryostat

Modern dilution refrigerators can pre-cool ^{3}He with a cryocooler replacing liquid helium. No external supply of cryogenic liquids is needed in these 'dry cryostats' and operations can be highly automatized. However, dry cryostats have high energy requirements and suffer of mechanical vibrations, such as those produced by pulse tube refrigerators. The first experimental machines were built in the 1990s, when (commercial) cryocoolers became available; they were capable of reaching lower temperatures than those of liquid helium and had sufficient cooling power. Pulse tube coolers are commonly used as cryocoolers in dry dilution refrigerators.
Dry dilution refrigerators generally follow two designs: one design incorporates a dedicated inner vacuum can, which is used to initially pre-cool the machine from room temperature down to the base temperature of the pulse tube cooler using heat-exchange gas; the second design uses a small amount of heat-exchange ^{4}He gas directly in the IVC volume to pre-cool the DU at 4 K and then is pumped out before starting the mixture circulation.

3.2 Setups used in this work

The development of the bolometer prototypes is accompanied by a systematic test of the produced samples. Depending on the specific project or R&D, different characteristics of the setup are required.
The aboveground facilities are used to perform fast tests of bolometric response and, in case of scintillating bolometers, to evaluate the light yield and the α-particle quenching factor.
To measure the radio-purity (internal α counting) and the α rejection factor, long measurement campaigns are performed in underground conditions. In case of too large bolometers (hundreds of grams), it may not be possible to characterize them aboveground because of the environmental radioactivity; then they should be directly moved underground.

3.2.1 LUMINEU test facility – 'Ulisse'

This test cryostat was assembled to serve the LUMINEU project [42] and the setup is optimized for this work. Four working months were needed to make it operational and ready for measurements (fig:3.3).
The facility [43] consists of a dry dilution refrigerator with an experimental space large

enough to house several large mass bolometers.
This Dilution Refrigerator located at the CSNSM is a classical dilution unit incorporating sintered silver heat exchangers and a large pumping system (40 m^3/h rotary pump and 400 l/s turbo pump in He). It can achieve reasonably high ^{3}He flow rates, thus providing the cooling power needed by massive $0\nu\beta\beta$ detectors.
The dilution unit is coupled to a pulse-tube refrigerator, consisting of the commercial unit PT-405 manufactured by Cryomech [44]. This model provides a cooling power of 25 W at 55 K at its first stage, and 0.3 W at 3.5 K at its second stage.
Unlike other machines, characterised by high vibration levels, pulse tubes are rather quiet devices. However, the operation of macro-bolometers in a pulse-tube DR remains non-obvious, as these detectors are particularly sensitive to the vibrations. The cryostat is described in more detail elsewhere [6] with the acronym PT-DR1. With respect to the original PT-DR1 design, the number of the sintered silver heat exchangers was reduced from four to two, without affecting the base temperature.
The DR presently runs at 7 mK with a flow rate of 130 μmol/s. In order to benefit from the cooling power available at the level of the regenerator, two copper heat exchangers were installed on the stainless steel tube connecting the two main stages of the pulse-tube cryocooler, aiming at improving the effectiveness of the mixture condensation process. The result of this modification was spectacular: the mixture condensation time was reduced from 20 to only 3 h. An interesting feature of the PT-DR1, particularly relevant in the present context, is that it is well optimized from the thermodynamical point of view. This allows to stop the ^{3}He compressor, a major source of vibrations, during the normal operation, keeping a low injection pressure (of the order of 0.5 bar at a circulation rate of 130 μmol/s). The cooling power in this condition is $\sim$100 μW at 100 mK and $\sim$0.5 μW at 7 mK.
The experimental volume available for the bolometers corresponds to a cylindrical space with a diameter of 30 cm and a height of 20 cm. This allows to easily house arrays of four large scintillating bolometers.
The length of the signal in the heat channel poses the serious problem of pulse pileup due to environmental radioactivity. In order to mitigate this effect, which is detrimental to the energy resolution on the γ lines, a shield of low-activity lead (less than 30 Bq/kg in ^{210}Pb content) was placed around the cryostat, with a minimum thickness of 10 cm. The benefit of the shield can be appreciated in tab:3.1. The system is suspended on three

Energy range keV	Without Pb shield [counts/s]	With Pb shield [counts/s]	Reduction factor
100-500	1.84	0.084	0.046
500-1000	0.309	0.0156	0.05
1000-1500	0.114	0.0064	0.056
1500-2000	0.027	0.0034	0.126
2000-2500	0.014	0.0021	0.15
2500-3000	0.005	0.0016	0.32

TABLE 3.1: Counting rate in the natural radioactivity region of the 23.8 g $ZnMoO_4$ detector in the CSNSM test facility before and after the installation of a lead shield around the cryostat. The reduction factor is the ratio of the counting rates after-to-before the lead shield implementation.

dumper modules to isolate it from external vibrations. At the mixing chamber stage a mechanical decoupling system is placed in order to reduce the vibration transmission to the detector. It is based on four stainless steel springs which provide a cut-off frequency

of ∼3 Hz with a ∼2 kg load. Modules of copper disks can be placed in order to tune the weight of the detector assembly.
The MC temperature can be stabilized to a fixed value by means of a PID controller, which delivers power to a heater in order to compensate temperature fluctuations.
In order to read out the bolometers, the refrigerator was equipped with a woven ribbon cable, carrying 12 twisted pairs of manganine leads in a polyamide resin. The acquisition system is based on a DC bias circuit and a room temperature pre-amplifier (see sec:4.1.1).
Calibrations are performed using thoriated tungsten wires placed in between the OVC and the external lead shield.

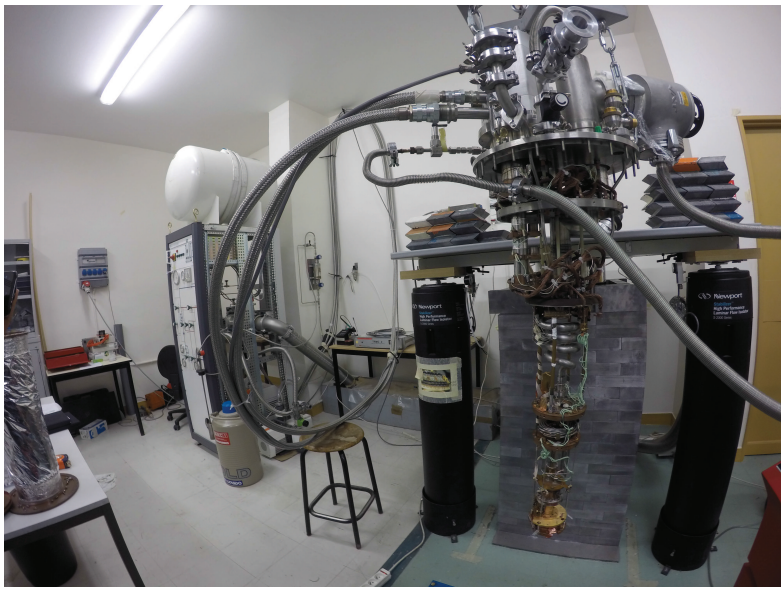

FIGURE 3.3: Picture of the Ulisse cryostat.

3.2.2 EDELWEISS test facility – 'Mulet Modane'

The Moulet-Modane cryostat (fig:3.4) at CSNSM is a standard wet cryostat, used for aboveground tests of the EDELWEISS [45] and LUMINEU bolometers. Like before, the cryostat floats on 4 dumping supports in order to decouple vibrations; a 10 cm lead shield covers the lower part of the cryostat to reduce the environmental radioactivity.
The IVC isolates the DU from the main LHe bath and is sealed with an indium joint. The first mixture thermalisation stage is at 4.2K and the condensation temperature is reached with a 1K-pot. In order to maintain the OVC at ∼4 K and the 1K-pot working, the LHe bath needs to be refilled each 1.5–2 days.
As in the Ulisse cryostat, the MC temperature is stabilized using a PID controller to compensate temperature fluctuations.
Detector calibrations are performed using thoriated tungsten wires placed in between the LHe dewar and the external lead shield.
The data acquisition system is based on AC electronics (sec:4.1.2) with cold pre-amplifiers at the ∼1 K stage.

FIGURE 3.4: Picture of the Mulet Modane cryostat.

3.2.3 A powerful liquid-free test facility – 'Cryofree'

The Cryofree cryostat (fig:3.5) at CSNSM is a highly automatised dry cryostat. The gas handling system is equipped with electro-valves and it can be fully controlled remotely. The precooling is made without exchange gas in the IVC since it incorporates an innovative dilution unit which can act as inner vacuum can to pre-cool the system from room temperature to ∼4K (sec:3.1). The pulse tube coupled to the DU is a commercial cryomech PT-410 which provides a cooling power of 1 W at 4 K.
The experimental space of Ø30 cm×20 cm allows to measure simultaneously many samples. This system, thanks to the special dilution unit and the high power pulse tube cooler, takes only 15 h to reach 30 mK and 20 h to go below 10 mK. At 100 mK the cooling power is about 100 μW.
This cryostat has been used only for some working tests of small bolometers like light detectors; in fact, this system is not surrounded with a lead shield to prevent the pileup induced by the natural radioactivity. The acquisition chain is the same of the Ulisse cryostat.

FIGURE 3.5: Picture of the Cryofree cryostat.

3.2.4 LNGS test cryostat – Hall-C cryiostat

The Hall-C cryiostat (fig:3.6) is located in the Laboratori Nazionali del Gran Sasso (LNGS), Italy. The Gran Sasso underground laboratory consists of three experimental Halls, named A, B and C. They are about 80 m distant from each other and, in principle, could feature slightly different rock coverage. The test cryostat is located in the hall C where the muons flux is measured by the BOREXINO experiment [46] to be $(3.14\pm0.01)\times10^{-4}$ m^{-2}s^{-1}.
The DR consists of a wet cryostat equipped with a high power dilution unit with an experimental space capable to host a CUORE mini-tower of 12 bolometer of $5\times5\times5$ cm^3 each.
The entire setup is shielded with two layers of lead of 10 cm minimum thickness each. The outer layer is made of common low radioactivity lead, while the inner layer is made of copper. The refrigerator thermal screens made by electrolytic copper provide additional shield with a minimum thickness of 2 cm. An external 10 cm layer of borated polyethylene was installed to reduce the background due to environmental neutrons. The experimental space is shielded against the intrinsic radioactive contamination of the dilution unit materials by an internal layer of 10 cm of Roman lead (^{210}Pb activity <4 mBq/kg), located inside the cryostat immediately below the MC.
The refrigerator is surrounded by a Plexiglas antiradon box flushed with clean N_2 from a liquid nitrogen evaporator and is also enclosed in a Faraday cage to eliminate electromagnetic interference.
Calibrations are performed using two wires of thoriated tungsten inserted inside the external lead shield in immediate contact with the outer vacuum chamber (OVC) of the dilution refrigerator.
Data are acquired with a DC electronics, similar to the one described in sec:4.1.1. For some channels a cold pre-amplifier at 4 K is provided.

3.2.5 Modane underground cryostat – EDELWEISS cryostat

The EDELWEISS cryostat (fig:3.7) is located in the Laboratiore Souterrain de Modane (LSM), France. The laboratory is located under the Fréjus mountain and it is one of the deepest underground laboratory. The above 1780 m of rock (4800 m water equivalent) reduce the muons flux down to $\sim$4 m^{-2}day^{-1}.
The EDELWEISS setup consists in a special upside down dilution unit with LHe as the first cooling stage. It is actually a hybrid machine with a pulse tube refrigerator used to decrease the LHe consumption of the main bath.
The head of the cryostat has a large experimental volume of 50 l and is placed in a ISO class 4 clean room.
The experimental volume is shielded from the radioactive environment by 10 cm of copper and 20 cm of lead. Pure nitrogen gas is circulated around the cryostat in order to reduce radon accumulation. All the electronic components were moved away from the detector and hidden behind a 7 cm thick Roman lead shield. A polyethylene shield of 50 cm is placed outside the lead shield. An active muon veto covers the entire setup with a 98% geometry efficiency.
The data acquisition system is based on AC electronics with cold pre-amplifiers at the 4 K stage.

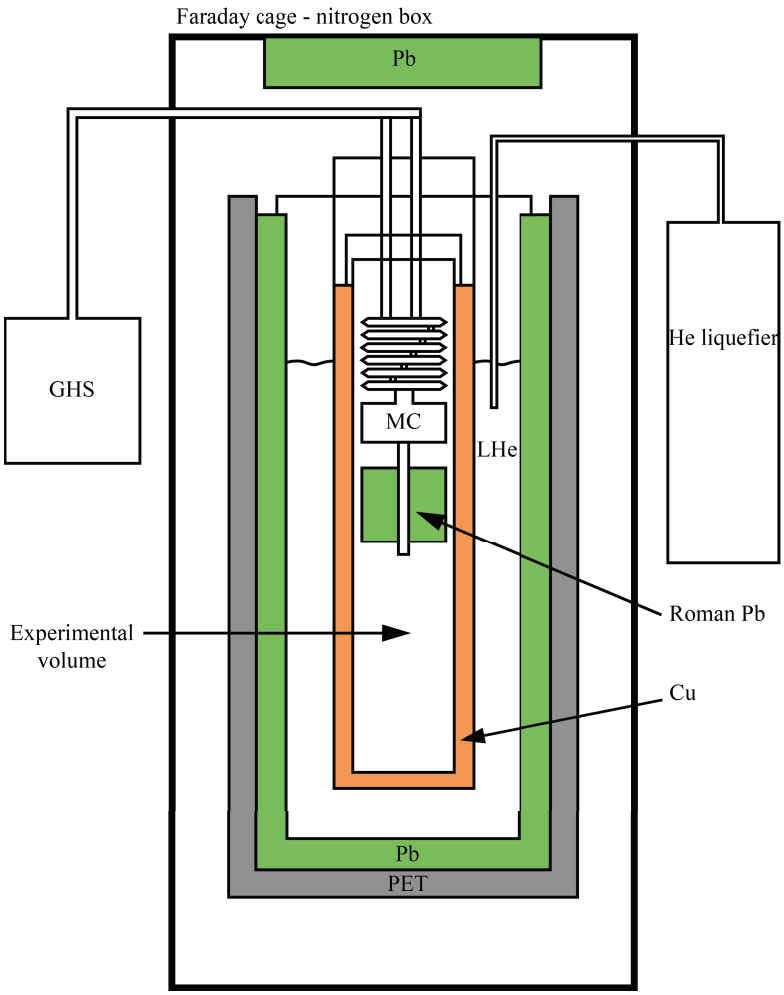

FIGURE 3.6: Scheme of the R&D cryostat in the Hall C of LNGS.

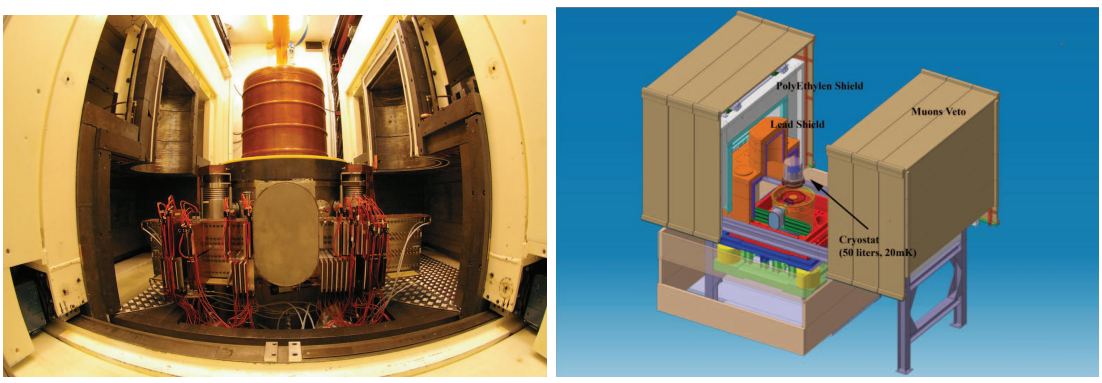

(A) (B)

FIGURE 3.7: (A) Picture of the cryostat clean room; the outer copper screen is visible in the center. (B) Scheme of the EDELWEISS cryostat setup.

3.2.6 Insubria cryogenic 1.5 K facility – 'Criostatino'

This cryogenic setup is located in the cryogenic lab of the Università degli Studi dell'Insubria, Como, Italy. It is based on a ^{4}He pumped refrigerator produced by INFRARED.

Cryostats based on pumped LHe can reach a temperature of T≈1.2 K. We used this system to validate some detector components in a systematic way. The working principle is the following: the samples are placed on a copper holder mechanically and thermally connected to a LHe dewar. The pressure at the He surface can be decreased using a rotatory pump in order to achieve low temperatures. The He dewar and the samples are placed in vacuum with a radiation screen maintained at 77 K by means of a LN_2 reservoir. The schematic structure of the cryostat is reported in fig:3.8. In view of the

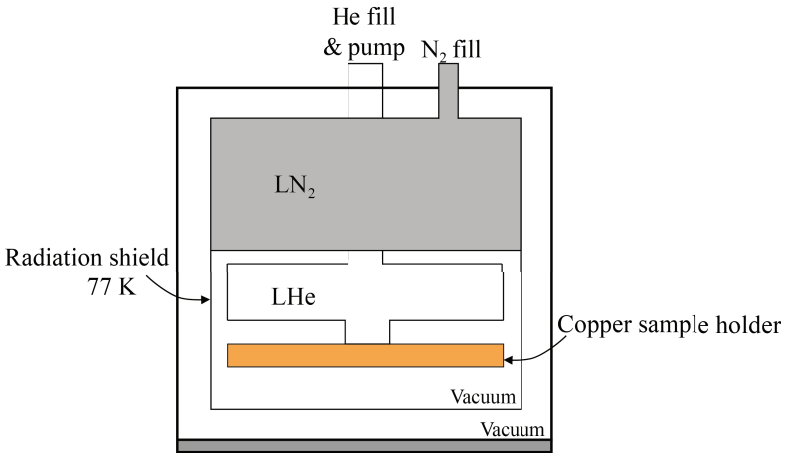

FIGURE 3.8: Scheme of the LHe pumped cryostat.

foreseen measurements a proper wiring of the cryostat and a calibrated thermometer were added to provide the necessary electrical connections and temperature readout.

Chapter 4

Data Processing and Analysis

This chapter describes how to treat the output signal of a bolometer.
An experiment in modern physics converts a physical event into an electric signal through a detector/sensor with well known characteristics. The output signal is usually digitalized and registered to be analysed. Two different approaches exist: either storing all the data continuously (streaming data) or storing only the physical events within a defined time window (triggered data). The first approach records the experiment whole output, which can be useful to check or reprocess the results; the second one is less time and space consuming but if something misses after the data taking, this is lost.
The output signals are affected by noise. Data analysis is the process to reconstruct the relevant information in the original physical events starting from the stored data.
This chapter, after the presentation of the readout system, describes in detail the data processing used to tag signals generated by interacting particles and extract the physical information of interest, while minimizing the errors induced by noise.

4.1 readout system

Two different methods were used to inject current in thermistors in order to read out the resistance. These two approaches follow different philosophies of data taking: one is based on DC bias and the other on AC bias. Two simplified circuits are shown in fig:4.1. Having performed measurement with different setups, both the circuits have been used: for instance the EDELWEISS set-up is based on the AC approach, while CUORE R&D uses DC electronics. Aboveground facilities also adopt either, depending on the framework in which the facility is built.

4.1.1 DC bias

This solution [47] is the one adopted for the readout of the Cuoricino experiment. It is implemented through a programmable front end electronics located at room temperature. A current flow is controlled by imposing a potential across the NTD Ge thermistor and two load resistors in series with it (fig:4.1); in order to obtain a constant current flow in the NTD thermistor, the two load resistors have a total resistance $2R_L \gg R_{NTD}$. The readout has a Differential Voltage Sensitive Pre-amplifier (DVP) at the input, which

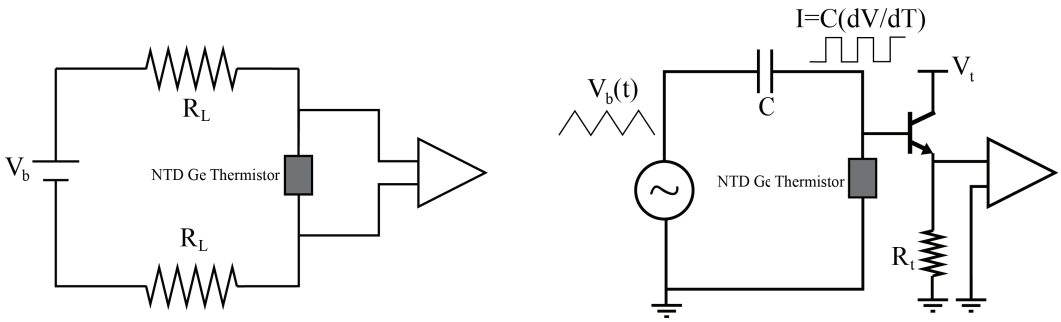

FIGURE 4.1: The electric scheme of the bias circuit for the thermistor readout: (left: **DC bias circuit**; right: **AC bias circuit**.

operates at room temperature. The R_L resistors which load the bolometer are also located at room temperature. The connection from the room-temperature front-end to the low temperature bolometer is made by a pair of twisted wires with a differential configuration.
The DVP inputs can be connected to the ground. The polarity of the bias voltage can be inverted independently for each detector channel and an attenuating resistive network is used to choose the bias-voltage value.
This input network arrangement allows to make a full DC characterization of the bolometer, consisting of a collection of a set of voltage-current points (Load curve or I-V curve) (fig:5.23).

4.1.2 AC bias

EDELWEISS-like systems use AC bias circuits; the motivation which led to this choice is the modulation theorem [48]. The idea is to shift the frequency band of the signal in a frequency region without noise structures. There is, however, a drawback in the use of this solution, which is the complication of the data processing to deconvolve the modulation with finite time windows and frequency sampling.
The thermistor is biassed with a square wave current, which is obtained thanks to a triangular wave through a load capacitor, as shown in fig:4.1. The frequency of the square wave (modulation frequency) is of the order of 1-2 kHz, to be compared with a sampling frequency of 100 kHz to assure enough points in the half period plateau. The current modulation and the ADC are synchronized by the same clock.
The square wave assures that the power dissipated in the thermistor is constant to reproduce the thermal conditions of the static bias. The load capacitor and the thermistor resistance form a CR circuit and the current needs time to reach the plateau; to compensate this effect a second wave is added to the triangular one. The compensation wave is very sharp in the transient in order to charge the capacitor faster. All the points remaining in the transition region are excluded from the demodulation algorithm which is applied off line.

4.2 Bolometers output

An event corresponds to the energy deposited by an interacting particle, which produces a variation in temperature. Assuming the simple monolithic model, after an event the

temperature evolution is:

$$\Delta T = \frac{\Delta E}{C} \cdot e^{-t \cdot \frac{C}{G}} \tag{4.1}$$

as described in sec:2.1.3.1.
From eq:4.1 the time constants of the corresponding pulse depend only on the heat capacity of the detector and the thermal conductance to the thermal bath. We know that the monolithic model is extremely simplified; however for the data processing discussion one can start from here and make some simple phenomenological considerations.
Let us assume that the energy deposit is instantaneous and a certain time is needed for the heat to diffuse to the sensor: this time is related to the rise time of the temperature pulse. The time to lower the signal during the thermalization to the heat sink often involves more than one exponential. In general the decay time of a pulse is well described with two exponential components, a fast one and a slow one: an example of a thermal pulse is shown in fig:4.2.
In first approximation the shape of the pulse (time evolution) is fixed by the detector

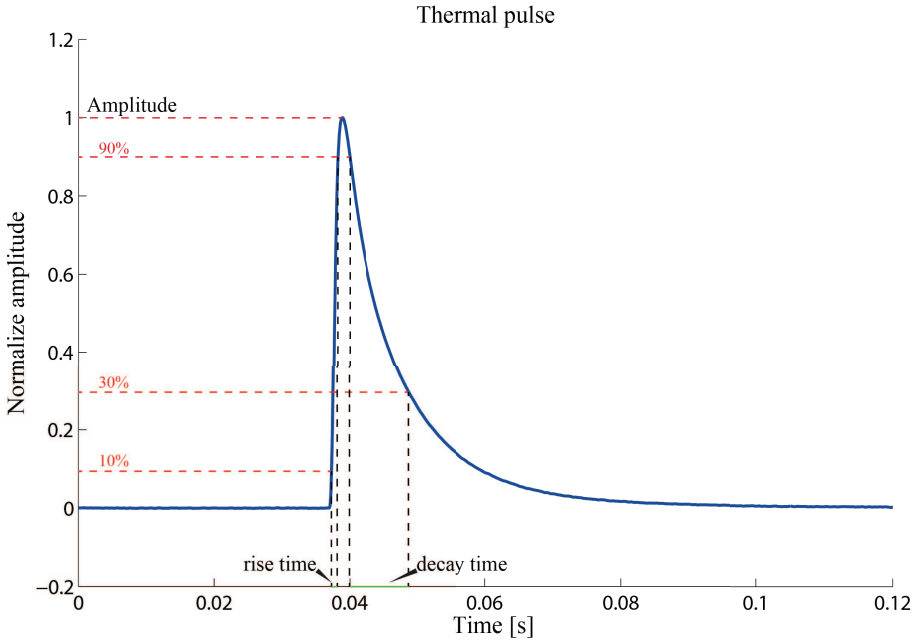

FIGURE 4.2: A typical thermal pulse.

characteristics (C_a, C_{el}, G_{el-ph}...), the working temperature and the bias current (working point) of the NTD Ge thermistor (sec:2.1.3.2). However, even the more complicated model including three thermal stages, described in sec:2.1.3.2, does not account in general for the shape of the pulses. Often a function involving three exponentials with three independent time constants is required for an accurate pulse description.
Once the measurement condition is established, a particle interaction in the detector generates an output signal $v(t)$, which reflects the temperature pulse features and is described as follows:

$$v(t) = As(t - t_0) + n(t) \tag{4.2}$$

where A is the amplitude, which contains the information on the deposited energy, $s(t)$ is the pulse shape function, t_0 is the arrival time of the particle and $n(t)$ is the noise. The basic parameters to characterise an event are defined as follows:

- **Pulse amplitude**: The value of A;
- **Rise time**: The time taken by the signal to rise from 10% to 90% of its maximum amplitude;
- **Decay time**: The time taken by the signal to decrease from 90% to 30% of its maximum amplitude.

To evaluate precisely these quantities and other interesting parameters, the noise contribution has to be reduced. We will define some treatments applied to the bolometer output and designed for minimizing the noise contribution.

4.3 Pulse amplitude

The pulse amplitude A is the most important parameter as it carries the information about the energy of the interacting particle. The value of A is commonly obtained from the maximum of the pulse where the noise contribution is smaller.
The noise contributes to the energy resolution σ, which for a peak of a given energy is:

$$\sigma_{tot} = \sqrt{\sigma_{noise}^2 + \sigma_{detect}^2} \tag{4.3}$$

where σ_{detect} is the value associated to the physics process itself (eq:2.5) and σ_{noise} is the error associated with the other contributions to the signal. σ_{detect} is an irreducible contribution while σ_{noise} can be decreased with an adequate data processing.
To understand this fact, an example can be described. Suppose that all the points describing the signal are proportional to the pulse amplitude so A can be computed as an average:

$$A = \frac{1}{N}\sum_{k=1}^{N} v(t_k)/s(t_k) \tag{4.4}$$

In case of white noise, σ_{noise} is reduced by a factor N equal to the number of points describing the pulse. Actually, when such an algorithm is introduced other contributions to σ can appear; in this case the time synchronization with the reference pulse (reference normalized pulse shape) is not obvious and the resulting σ_{tot} will be:

$$\sigma_{tot} = \sqrt{\left(\sigma_{noise}/N\right)^2 + \sigma_{detect}^2 + \sigma_{sinc}^2}. \tag{4.5}$$

If the detector is not linear, σ_{tot} can be even worse.
The most effective way to reduce the noise contribution is to filter it using matched-filters, which, thanks to the properties of the Fourier transform, do not affect the value of A (eq:4.6). A matched-filter is modelled on the relationship between the expected signal and the noise. The matched-filter transfer function (TF) is designed to optimize a chosen response parameter following a criterion of optimization.
Once the transfer function is designed, the filtered pulse will be equal to:

$$v_{filtered}\left(t\right) = \frac{A}{2\pi}\int_{-\infty}^{+\infty} H\left(\omega\right) V\left(\omega\right) e^{-j\omega t} d\omega \tag{4.6}$$

where $H\left(\omega\right)$ is the transfer function in the frequency domain, $V\left(\omega\right)$ is the Fourier transform of the signal $v(t)$. We propose optimum transfer functions $H(f)$ which are built

using only the noise power spectrum and a reference pulse. Details on the computational methods and filters can be found in appendix:A.

4.3.1 The Wiener optimum filter

This filter is designed to minimize the square difference between the $v_{filtered}(t)$ and the reference pulse $s(t)$

$$\int_{-\infty}^{+\infty} |v_{filtered}(t) - s(t)|^2 \, dt \tag{4.7}$$

The Wiener optimum filter then preserves at maximum the shape of the pulse. It is a suitable TF to extract the shape parameters and the time constants of the pulses. The resulting transfer function is:

$$H(f) = \frac{|S(f)|^2}{|S(f)|^2 + |N(f)|^2} \tag{4.8}$$

4.3.2 The Gatti-Manfredi optimum filter

This filter, unlike the previous one, does not preserve the shape of the pulse. In this case the criterion of optimization is the maximization of the signal to noise ratio ρ:

$$\rho = \frac{\frac{A}{2\pi} \int_{-\infty}^{+\infty} H(\omega) V(\omega) e^{-j\omega t} d\omega}{\left(\frac{1}{2\pi} \int_{-\infty}^{+\infty} |H(\omega)|^2 \mathcal{N}(\omega) \right)^{\frac{1}{2}}} \tag{4.9}$$

There is a unique solution for $H(\omega)$ [49] which maximises ρ and it is

$$H(j\omega) = K' \frac{S^*(\omega)}{N(\omega)} e^{-j\omega\tau_M}. \tag{4.10}$$

The resolution can be derived as:

$$\sigma^2_{noise} = \left(\sum \frac{|S(\omega)|^2}{\mathcal{N}(\omega)} \right)^{-1} \tag{4.11}$$

It is also interesting to notice that, thanks to the properties of the Fourier transform, this filter can be obtained using all the derivatives of its components without changing the response.
Using the derivative of the signal is a clever way to get rid of the offset problem:

$$\mathcal{F}\left(\frac{df(t)}{dt} \right) = \omega \mathcal{F}(f(t)) \tag{4.12}$$

$$s_1(t) = AK' \int_{-\infty}^{+\infty} \omega S_1(\omega) \frac{\omega S^*(\omega)}{\omega^2 N(\omega)} e^{-j\omega\tau_M} d\omega \tag{4.13}$$

4.3.3 The integrated optimum filter

The last proposed algorithm to extract the value of A in the frequency domain is analog to a filtering procedure. The amplitude is evaluated in the whole frequency domain in a way similar to the ratio $A = v(t)/s(t)$ in the time domain, but after the application of a weight function (filter). A is obtained minimizing the sum of the squared differences between the pulse and the reference pulse in the frequency domain

$$\chi^2 = \sum_k \frac{|V(\omega_k) - AS(\omega_k)|^2}{\mathcal{N}(\omega_k)}. \tag{4.14}$$

Imposing $\frac{\partial \chi^2}{\partial A} = 0$, one gets:

$$A = \frac{\sum_k \frac{Re(V(\omega_k)\cdot S^*(\omega_k))}{\mathcal{N}(\omega_k)}}{\sum_k \frac{|S(\omega_k)|^2}{\mathcal{N}(\omega_k)}} \tag{4.15}$$

Now the 'filter' becomes clear: in the numerator the signal at each frequency, $V(\omega_k)$, is weighted by $S(\omega_k)/\mathcal{N}(\omega_k)$, so that frequencies with a large signal to noise ratio are emphasized. The noise is the following:

$$\sigma^2_{noise} = \left(\sum \frac{|S(\omega)|^2}{\mathcal{N}(\omega)} \right)^{-1}. \tag{4.16}$$

4.4 Filter application and comparison

The presented filters are just a few examples among all the existing matched-filters. They have been selected on the basis of their properties in view of a specific application. The spectrometric properties of a bolometer are crucial in this kind of research; for that purpose the Gatti-Manfredi filter and the integrated filter are the most appropriate.
It is also important to remark that in many cases, different particles could generate pulses with a different shape in case of a not complete thermal formation of the signal. Sometimes these differences are extremely small. Therefore, to be able to reconstruct the time pattern of the pulse becomes an important tool for particle identification. To better evaluate these differences, the Wiener filter must be selected.
In terms of spectrometric performance, fig:4.3 shows an energy spectrum obtained by simulated data. The purpose of the simulation is to test the three filter responses (fig:4.4). The data is generated adding pulses, with three different amplitudes, to the noise, which is artificial and consisting of three contributions: white noise, a 50 Hz and a 30 Hz sinus with random phases. The two frequencies are close to the most important contributions normally found in real data.

As expected, from this simulation, the best results for the amplitude evaluation are obtained with the Gatti-Manfredi filter and the integrated one. The Wiener filter becomes less effective as the amplitude-to-noise ratio increases.
With the real data the necessary quantities to compute the transfer functions are obtained numerically from the data themselves. The estimation of $\mathcal{N}(\omega)$ is made by averaging the power spectrum of a large set of data windows not containing signals, while the signal shape $s(t)$ is obtained by averaging a set of selected particle signals.

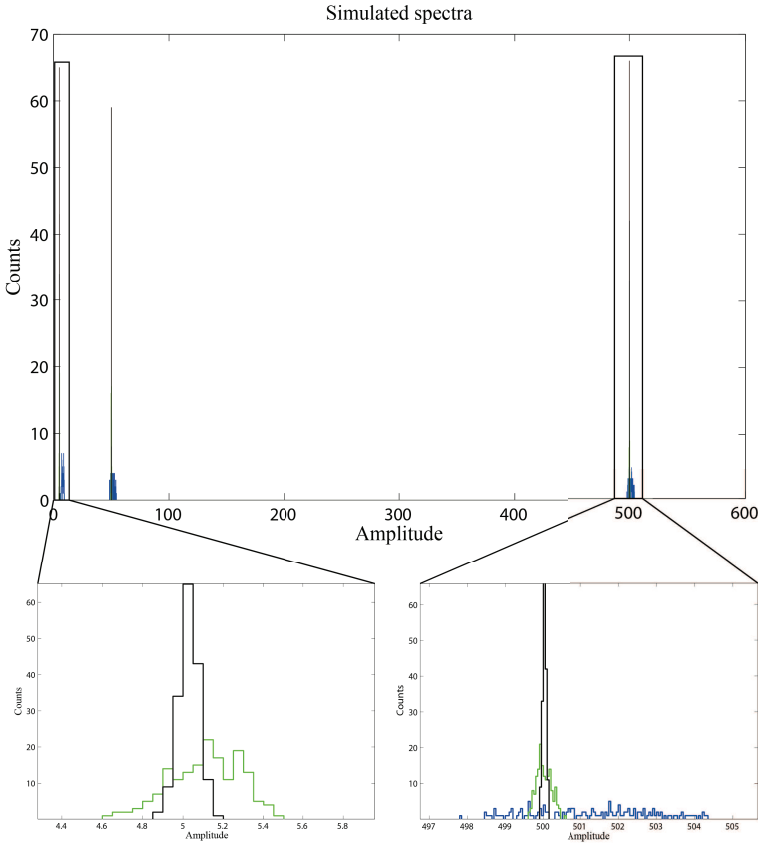

FIGURE 4.3: Amplitude spectrum of the simulated signals. The blue line represents the maximum of the raw data, the green line represents the maximum obtained with the data treated with the Wiener filter and the black line represents the maximum evaluated with the Gatti-Manfredi filter and the integrated one.

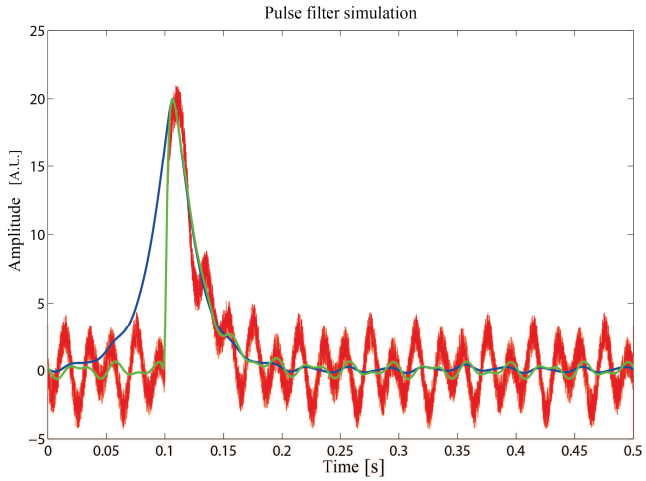

FIGURE 4.4: Applied filters. Red: the original pulse with noise - Green: pulse filtered with the Wiener transfer function - Blue: pulse filtered with the Gatti-Manfredi transfer function.

4.5 Trigger

The first step of the analysis process consists in recognizing the pulses and tag them as events. This first step is called trigger.
The basic trigger is a threshold on the voltage output: when the signal exceeds a certain fixed value, the trigger tags this as an event. The threshold is chosen as a function of the noise to avoid to tag noise fluctuations instead of physical events (electrical spike, crosstalk...).
For the $0\nu\beta\beta$ searches, there is no need to look at very low energies –events close to the baseline fluctuation– but for other applications using bolometers this is mandatory. A lower energy threshold can be obtained because, compared to raw data, matched-filtered data feature a larger signal to noise ratio. However, filtering numerically all the data is not obvious.
The algorithm needs as input the expected shape of the signal and the noise power spectrum of the bolometer like the normal filter process. No manual tuning is needed, because all the parameters can be set at optimal values automatically. This can be done with a simple algorithm, described in [50], which allows to perform the fast Fourier transform (FFT) continuously on the data.
The algorithm works as follows:

- it selects a time window of M points.
- it builds the transfer function which will be described by M points.
- it inserts a number of M points equal to 0 in the center of the TF obtaining therefore a $2 \times M$ point vector.
- a data window of $2 \times M$ can be processed with the modified TF.
- the M/2 points at the edges are spoiled and rejected (fig:4.5).
- it repeats the process iteratively taking $2 \times M$ points windows each M points of data and merges the unspoiled part (fig:4.6).

Thus the trigger can be applied on the filtered data without any windowing problem.
The matched-filter used for this purpose is the Gatti-Manfredi mached-filter for a sim-

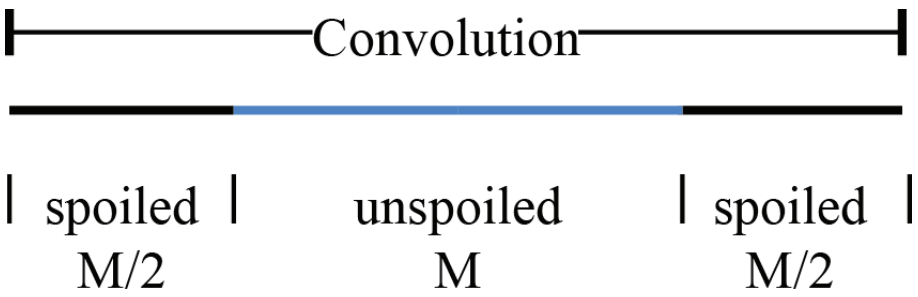

FIGURE 4.5: Window of $2 \times M$ points convoluted with the modified TF. The M/2 points at the edges are spoiled and rejected.

ple reason: it is the filter which performs the best signal-to-noise ratio.
A drawback of this procedure happens when high energy pulses are triggered: a set

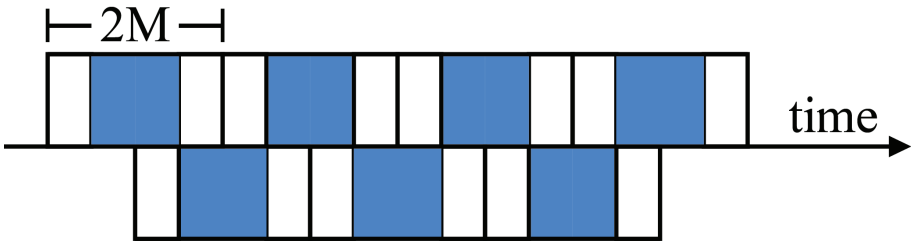

FIGURE 4.6: Treatment of the data. Each M points a $2 \times M$ points window are taken and filtered. The central M points of each treated window are taken and merged with the others.

of secondary pulses are seen. This is due to the fact that the filtered pulse may have symmetric lobes above zero; these bumps can occur when the noise does not satisfy completely the requirement (appendix:A). The amplitude above zero of the side lobes is a constant fraction of the amplitude of the main lobe, and it can be estimated from the filtered reference pulse (fig:4.7). To get rid of this problem we considered three options: setting a second threshold based on different parameters; an active search of the lobes; comparing the transformed signal shape with the individual pulse with that of the reference one.
The third option has been chosen. After various tests on different algorithms this second selection criterion is based on the correlation parameter between the filtered reference pulse and the individual filtered signal which exceeds the threshold; it is easy to compute and has no systematic error.
Different interacting particles produce slightly different pulse shapes and the time constants can also depend on the energy; the correlation is very sensitive to the pulse shape and the corresponding threshold has to be chosen carefully. This second trigger evaluation could be long but feasible. It is always possible anyway to find some more complicate and efficient algorithms.

4.6 Analysis

The following step in the data acquisition is the production of the n-tuples: for each detected pulse a vector containing all the relevant parameters is created. Some of these elements can be derived from the raw pulse, other parameters from the filtered one. It is easier to process the filtered pulse because the Gatti-Manfredi transformed pulse is symmetrical with respect to the maximum. Processing the raw pulse is more complicate: the maximum position is not so well defined, the baseline offset is not equal to zero and the exact signal starting point is difficult to find. Given the uncertainty on the maximum position, to know the starting point is crucial; to find it, an algorithm described in [51] is used: it is very effective and corresponds to the following steps:

- Calculation of the standard deviation of the baseline noise in a safe window before the maximum in order to avoid the pulse contribution.
- Determination of the first point which exceeds a certain number of baseline sigmas (which belongs surely to the signal).

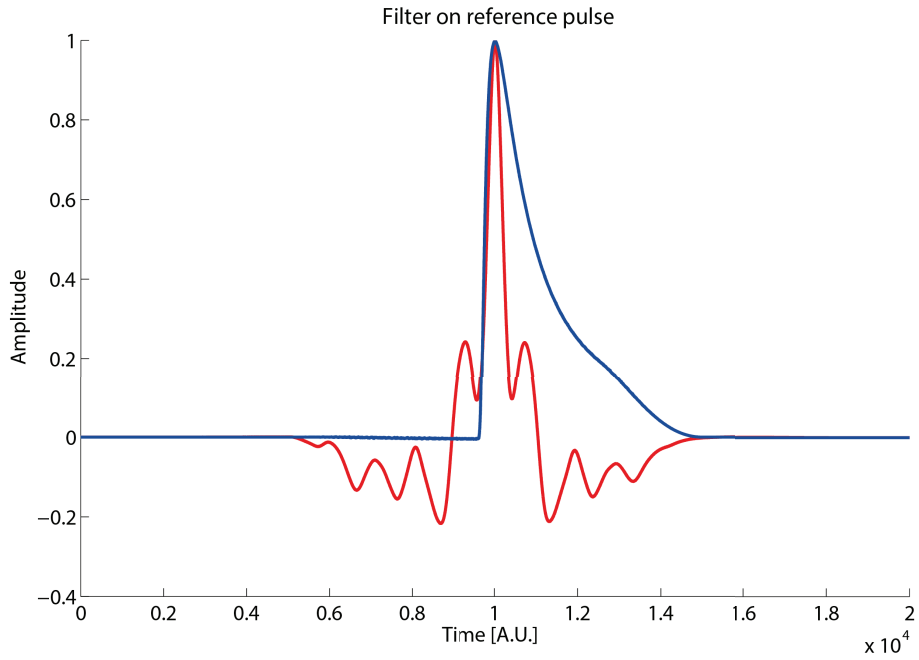

FIGURE 4.7: Blue - real reference pulse. Red - reference pulse filtered with the Gatti-Manfredi matched filter.

- Going back from this point till the sign of the derivative changes and set this point as the start of the pulse.

Once the starting point is found, all the time dependent parameters can be calculated on the raw pulse.
There are several parameters of interest. They are resumed here with a description of the computation method, when necessary, for clarity:

I **Arrival time**: The exact position of the pulse maximum;

II **Baseline value**: The value of the signal offset; it is computed as:

- The average of the signal in a safe interval before the pulse maximum.
- The constant term of a linear fit performed on a plot of the pulse versus the reference pulse $(s(t_k),v(t_k))$.

III **Pulse amplitude**: The energy of the pulse. It is useful to compute it in several ways because the comparison allows to find discriminating parameters:

- The average around the maximum of the raw pulse.
- The maximum of the filtered pulse in the time domain.
- The slope of a linear fit after plotting the individual filtered pulse as a function of the reference filtered pulse $(\tilde{s}(t_k),\tilde{v}(t_k))$.
- The slope of a linear fit on the pulse versus the reference pulse $(s(t_k),v(t_k))$.
- The amplitude of the pulse at a fixed time delay after the maximum of the signal. The so called delayed amplitude.

IV **Rise time**: The time the signal needs to rise from 10% to 90% of its maximum amplitude;

V **Decay time**: The time the signal needs to decrease from 90% to 30% of its maximum amplitude;

- in both the above, cases if the point corresponding to these percentages is missing, it is possible to interpolate it linearly using the nearby points.

VI **Mean time value** [52]: The parameter is given by the following formula:

$$\langle t \rangle = \frac{\sum_k f(t_k)\, t_k}{\sum_k f(t_k)} \tag{4.17}$$

where k runs over a fixed number of points from the start of the pulse.

VII **Test Value (AF)**: It is the mean squared difference between the filtered reference pulse and the single filtered pulse. The parameter AF (Adaptive Filter) evaluates the goodness of the fit:

$$AF = \frac{1}{N} \sum_{i=1}^{N} (s_i - a_i)^2 \tag{4.18}$$

VIII **Test Value Left (TVL)**: It is the test value on the left of the signal.

$$TVL = \frac{1}{\frac{N}{2}} \sum_{i=1}^{\frac{N}{2}} (s_i - a_i)^2 \tag{4.19}$$

IX **Test Value Right (TVR)**: It is the test value on the right of the signal.

$$TVL = \frac{1}{\frac{N}{2}} \sum_{i=\frac{N}{2}+1}^{N} (s_i - a_i)^2 \tag{4.20}$$

4.7 Analysis Program

Based on the elements described above, a dedicated analysis program for the bolometer output has been developed. This program allows the user to build the mached-filter, trigger and data pre-processing. The output is an n-tuple file where each event is described by its parameters arranged in a row of values.

Chapter 5

Bolometric light detectors

In this chapter we will discuss the structure and the performance of Light Detectors (LDs) used with scintillating bolometers. In our work these devices consist of thin slabs of semiconductor operated as auxiliary bolometers.
The main purpose is to identify particles by exploiting scintillation light; thus, the requirement for the light detector is to be sensitive enough to well distinguish the different light yields (LYs) related to different interaction types with several sigma accuracy at the energy of interest.
The needed sensitivity and energy resolution of the light detector will indeed depend on the LY and the Quenching Factor (QF) of the scintillating material. Let's make a numerical example with a $ZnMoO_4$ scintillating crystal. The common obtained LYs are $LY_{\gamma/\beta}$ ≈1 keV/MeV and LY_{α} ≈0.2 keV/MeV which correspond to a $QF_{\alpha/\beta}$ ≈0.2. At the Q-value of the $0\nu\beta\beta$ decay of ^{100}Mo, 3.034 MeV, the measured scintillating light is ≈ 3 keV for β particles and ≈ 0.6 keV for α particles. Using the heat signal from the main bolometer to trigger the pulses, an energy resolution for the LD of ≈ 500 eV is large enough to reject efficiently the alpha background. The goal is to decrease the contribution of the α background to $b<10^{-4}\ \frac{\text{cts}}{\text{keV}\times\text{kg}\times\text{y}}$; with a 500 eV σ on the light detector, the Discrimination Power (DP) with a $ZnMoO_4$ scintillating crystal is equal to 3.4 (eq:2.35) which corresponds to a rejection factor >99.9%. If we consider an α background index similar to the one obtained by the CUORE-0 experiment (sec:2.2.1), the background induced by the alpha particle in the ROI becomes $<2\times10^{-5}\ \frac{\text{cts}}{\text{keV}\times\text{kg}\times\text{y}}$.
In this context, improving the energy resolution leads to a better discrimination factor and improving the sensitivity means a lower energy threshold for the discrimination of the different LY bands.

In the first part of this chapter the existing technologies of bolometric LDs are briefly discussed; then we will focus on the detectors fabricated and operated in this work. The rest of the chapter is dedicated to possible achievable improvements. We will discuss the optimization of the thermal response, the effect of an anti-reflective coating and we will conclude with the Neganov-Luke amplification applied to LDs.

5.1 Light detectors in general

In a scintillating bolometer, the light generated in the main crystal is first converted into heat by absorption on the light detector whose material is chosen for its absorption coefficient and its heat capacity. The thermal sensor is directly in touch with the absorber (when it consists of a thin film deposited on it) or connected with a high thermal conductivity link (when it consists of a massive chip attached by gluing).
The rise time of the light detector has to be as small as possible because it has to be much smaller than the decay time $\tau_d \approx C/G$. The fact that $\tau_r < \tau_d$ guarantees the maximal sensitivity mainly because the heat does not evacuate the bolometer before the sensor measurement. Moreover, a fast light detector is advantageous because a massive bolometer has a slow response and often suffers of pileup so a fast light detector can improve the rejection of these events [51].
The typical wavelength emission for a scintillating bolometer crystal is in the visible bandwith and so the most frequently used materials for the light detector in present experiments are Ge, Si and SOS (Silicon On Sapphire) as shown in tab:5.1. The sapphire is transparent at the visible wavelengths and needs to be coated to increase the absorption.

Absorbing materials	Specific heat C_0T^3 $\mathrm{JK^{-1}cm^{-3}}$	Energy gap at T=0K	nature
Silicon	$6.3 \times 10^{-7}T^3$	$1.17eV$	Semiconductor
Germanium	$2.8 \times 10^{-6}T^3$	$0.6eV$	Semiconductor
Sapphire	$1.8 \times 10^{-7}T^3$	$\approx 9.3eV$	Dielectric

TABLE 5.1: Heat capacity and energy gap for materials used as bolometric LDs.

At present, four combinations of materials and sensors are used for large area bolometric light detectors:

- **Ge and NTD thermistor:** in this case the Ge NTD thermistor is glued with a bicomponent epoxy glue on the substrate [this work].
- **Si and IrAu TES sensor:** the TES (Transition Edge Sensor) can be deposited directly on the detector or on a carrier depending if the detector surface is rough or polished [53].
- **Ge and MMC:** the phonon collection on the Ge is performed by a gold film deposited on the Germanium and then transferred to the MMC (Metallic Magnetic Calorimeter) coupled to the heat sink by means of golden wires [54].
- **SOS and W TES sensor:** W-TES (tungsten Transition Edge Sensor) is directly deposited on the substrate; on a side of the TES element there is a heater element providing temperature stability around the T_c and the thermal link is obtained via the bonding wires [55].

The absorber consists of a thin wafer, less than 1 mm, of the chosen material.
The performance of these detectors depends on their intrinsic properties and on the measurement environment. In tab:5.2 the best performances achieved with the different detectors are reported. The following parameters of interest characterizing a light detector can be defined:

- **Sensitivity:** the ratio between the signal amplitude and the absorbed energy which has determined it, $S = \frac{\partial V}{\partial E}$.
- **Baseline resolution:** in a first approximation, it is the true RMS value of the baseline in absence of pulses. If a filtering procedure is applied to pulses, it can be applied also to baseline segments having the same length of the pulses. The gaussian distribution of the amplitudes obtained in this way provides the baseline resolution in terms of σ or FWHM.
- **Energy resolution at 5.9 keV:** the σ and the FWHM of the ^{55}Fe 5.9 keV X-ray peak, often used for the calibration.
- **Rise time τ_r and decay time τ_d:** the time that the signal needs to rise from 10% to 90% and to decrease from 90% to 30% of its amplitude.

Absorbing materials	Area cm^2	Sensor	Baseline Energy resolution	Rise Time	Decay time	Sigma @ 5.9 keV	ref.
Germanium	12.6	NTD	$\approx$ 20 eV	$\approx$ 0.9 ms	$\approx$ 1.5 ms	$\approx$ 130 eV	[56]
Silicon	4	IrAu TeS	$\approx$ 50 eV	-	-	-	[53]
Germanium	20	MMC	-	$\approx$ 0.2 ms	$\approx$ 2.5 ms	$\approx$ 230 eV	[54]
SOS	12.6	W-TES	$\approx$ 7-20 eV	$\approx$ 0.7 ms	$\approx$ 2.5 ms	$\approx$ 100 eV	[55]

TABLE 5.2: Best performance of the present LDs.

The different LDs used in the present experiment show a similar performance; the best energy resolution at present is achieved with SOS and W-TES.

5.2 NTD based Ge light detectors

In view of large experiments with scintillating bolometers which will feauture thousand of detectors, the detector should be reproducible and easy to build.
The solution that we adopted consists in light detectors made by an ultrapure Ge disk as the absorber coupled to a NTD Ge thermistor. Using the same material for the absorber and the sensor is advantageous as they can be mechanically coupled without problems of thermal contraction. These sensitive detectors are simple and effective. We have used devices with two different structures.

5.2.1 Easy-assembly light detector

The majority of the LDs used in this work belong to this structure. We produced many of them to couple with our scintillating crystals as they provide a performance good enough.
In general LDs of this type are built as follows: the germanium substrate is held in a copper frame with Polytetrafluoroethylene (PTFE) clamps. The temperature sensor is glued on the absorber surface with spots of Araldite epoxy glue. Electric and thermal connections are provided by Ø25 μm golden wires which connect the NTD electric pad to the contacts on the holder. A picture of a light detector is shown in fig:5.1.
The typical performance obtained with this kind of detector is summarised in tab:5.3;

the energy calibration is obtained with the peak at 5.9 keV of ^{55}Fe X-ray source placed near the detector in the experimental set-up.
The performance achieved with this simple structure is largely sufficient for particle discrimination in $ZnMoO_4$ based scintillating bolometers. For simplicity we decided to keep this configuration [57].

TABLE 5.3: Average performance of basic Ge + NTD thermistor LDs.

Sensitivity	Baseline Energy resolution σ	^{55}Fe energy resolution σ	Rise time	Decay time
0.7-2 μV/keV	≈130 eV	≈180 eV	≈ 1-3 ms	≈ 20 ms

However, the detectors need an assembly protocol to be reproducible. Based on the acquired experience, a few guidelines to build them are listed in the following:

- **NTD thermistor:** the NTD Ge thermistor has to be as small as possible, since its specific heat capacity is much larger than that of the absorber. The heat capacity of the electrons in a NTD Ge thermistor dominates as the dependence on temperature is linear to be compared with the cubic dependence of the germanium lattice. The smallest NTD that we produced has a size of $3 \times 1 \times 0.6$ mm^3 and it is glued to a germanium wafer of $\O44 \times 0.175$ mm^3. In this detector the heat capacity of the NTD is ∼6 times larger than the absorber at 20 mK.
- **NTD gluing:** the NTD is glued on the substrate with a bi-component glue named Araldite. We suggest to put a couple of small drops of glue using a smeared needle and press NTD on the surface with a force corresponding to a weight of 30 g. The quantity of glue should be enough to make a layer which covers the whole matching surface.
- **Bonding wire:** the thermalisation and the electric contact are made with bonding wires. We measured different wire materials and lengths and the detector response does not show appreciable differences. We did not perform systematic tests, but using gold or silver wires no appreciable difference appears even if gold has a factor 30 in thermal conductivity with respect to silver. We used once a superconducting wire and the thermal response was very slow (several seconds decay time) proving the negligible contribution of the suspension. In fact, the bottle neck of the heat flow in this configuration is elsewhere. Two small $\O25-50$ μm gold wires are good enough.
- **Suspension:** We tested different suspensions trying to evaluate the thermal response with different holding systems. No appreciable difference was obtained using plastic and dielectric material. The thermal conductance to the heat sink of the suspensions is negligible with respect the gold wire. The PTFE clamp elements work well. Anyway we suggest to reduce the contact surface as much as possible shaping the element with a cutter because a smaller contact surface with the other material is always better.

The described detectors are easy to build and the performance are reproducible even if they are hand made.

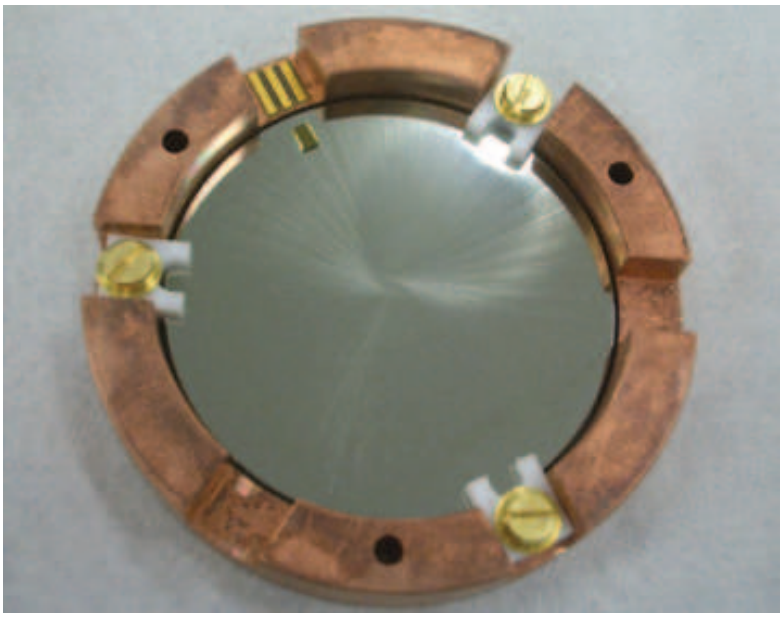

FIGURE 5.1: Picture of a Ge disk instrumented with a NTD Ge thermistor operated as light detector.

5.2.2 Advanced NTD based light detectors

In this section an advanced light detector developed at IAS (Institut d'Astrophysique Spatiale) [58] will be described. This detector is based on the same technology of our light detectors but it is optimised in terms of thermal response. We used this detector coupled to a scintillating crystal measuring it both aboveground and underground.
The purpose of the thermal optimization is to improve the energy resolution; starting from eq:2.5, one can obtain the theoretical limit on the ΔE_{FWHM} with a resistive sensor [59]:

$$\Delta E_{FWHM} = 2.35 \Delta E_{rms} = \epsilon \left(k_b T_0^2 C\right)^{\frac{1}{2}} \tag{5.1}$$

where ϵ is a new coefficient which depends on the properties of the sensor (for a NTD Ge thermistor in general $\epsilon \approx 6$) and T_0 is the temperature of the thermal bath. In eq:5.1 the factor ϵ depends on the temperature difference between the detector and the heat sink $\Delta T_b = T - T_0$; the minimum of ϵ is found at $T/T_0 = 1.2$.
To improve the energy resolution we can act on the heat capacity trying to decrease it as much as possible, reducing the NTD Ge thermistor size and the absorber heat capacity. Once the material of the absorber is chosen, to reduce the heat capacity we can act on the absorber size: given that a large surface is convenient for light collection, the thickness has to be reduced. To measure the scintillation light, the minimal thickness d is defined by the absorption coefficient at the wavelength of interest; for photons of $\lambda = 600$ nm the absorption length is 42 nm.
In their optimization discussion, the authors of ref:[58] consider one other constraint: the substrate must have a d large enough to assure that the internal thermal gradients ΔT_i between the edge and the sensor are much smaller than ΔT_b:

$$\Delta T_i \ll \Delta T_b \tag{5.2}$$

in order to respect the approximation of a monolithic calorimeter. Let's consider a disk shaped absorber with a radius r_a. The thermal conductance G_i between the border of

the absorber and the sensor placed in the center with radius r_s is:

$$G_i = \frac{(G_0 2\pi d)}{\log(r_a/r_s)} \tag{5.3}$$

G_0 is the intrinsic heat conductivity of the absorber which is given for thin materials by the Casimir's law $G_0 = g_0 dT^3$. Actually, for thin materials the surface state is not negligible in terms of phonon transmission: a factor ≈4 [58] increase is observed for a polished surface. To satisfy eq:5.2 the thermal conductivity should be

$$G_i \gg G_b \tag{5.4}$$

For our detector we can set $r_s \approx r_a/20$ and fixing the arbitrary condition $\Delta T_i < 5\Delta T_b$ we can set a minimum thickness of the substrate d equal to

$$d \geq \frac{4.8 C_0 S}{g_0 \tau_b} \tag{5.5}$$

where τ_b is the characteristic time constant of the detector in a monolithic picture, $\tau_b = C/G_b$. To respect the condition imposed by eq:5.5, once the thickness of the absorber is reduced at the limit of the technology, a constraint on the thermal conductivity G_b has to be satisfied.
The tested advanced detector has been build following the scheme shown in figure 5.2. The detector is made by a Ø40 mm Ge disk with a thickness of 45 μm with a $2 \times 0.4 \times 0.3$ mm^3 NTD Ge thermistor, which corresponds to a heat capacity of the absorber ∼4 times larger than the NTD at 20 mK. The detector is held using superconducting wires which have G=0 to concentrate the thermal flow in the calibrated heat link. The electric contacts are made by a superconductor too. This complicated design provides an energy resolution 5-6 times better than the one described in the previous section.

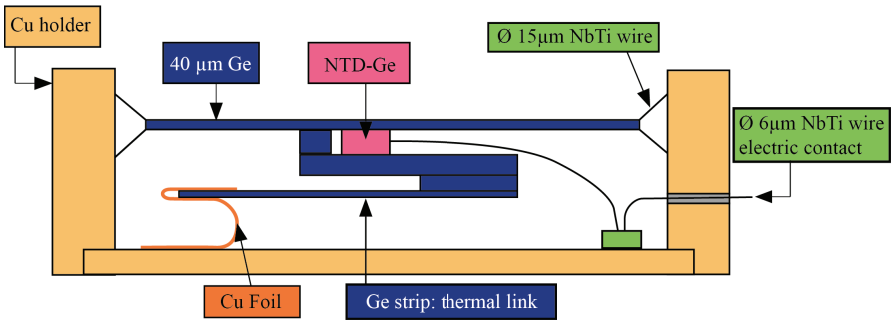

FIGURE 5.2: Scheme of an advanced light detector construction.

5.2.2.1 Aboveground results

This detector was first measured in the aboveground test facility Ulisse in CSNSM (sec:3.2.1) with the performance reported in tab:5.4 and in fig:5.3.

Sensitivity	Baseline Energy resolution σ	^{55}Fe energy resolution σ	Rise time	Decay time
3.12 μV/keV	33 eV	157 eV	0.9 ms	1.4 ms

TABLE 5.4: Performance of the advanced light detector operated aboveground.

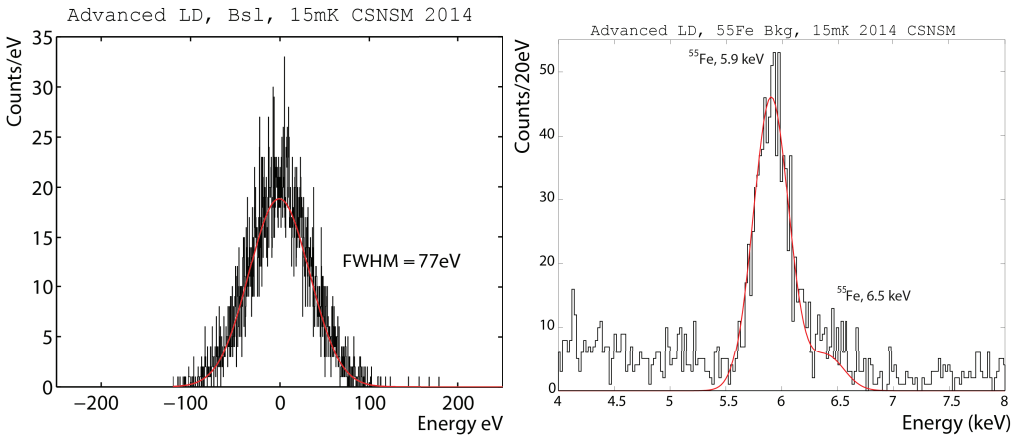

(A) (B)

FIGURE 5.3: (A) Histogram of the baseline windows treated like pulses (black line) with a gaussian fit (red line). (B) Histogram of the 5.89 keV line of the ^{55}Fe source.

5.2.2.2 Underground results

The detector was moved underground in the LNGS laboratories (sec:3.2.4) to perform the low radioactive measurements where it gave the best results ever achieved with this technology.

Sensitivity	Baseline Energy resolution σ	^{55}Fe energy resolution σ	Rise time	Decay time
4.24 μV/keV	17 eV	141 eV	1.2 ms	2 ms

TABLE 5.5: Performance of the advanced light detector operated underground.

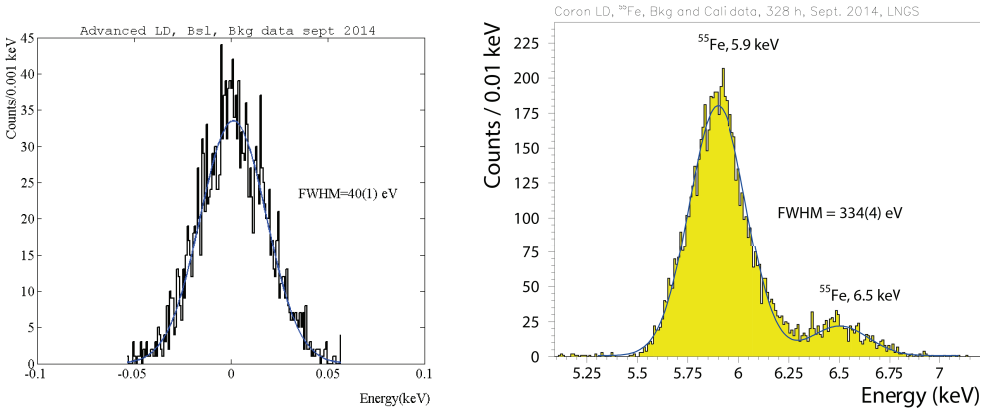

(A) (B)

FIGURE 5.4: (A) Histogram of the baseline windows treated like pulses (black line) with a gaussian fit (red line). (B) Histogram of the 5.89 keV line of the ^{55}Fe source.

5.2.3 Conclusion

Among the possible combination of absorbers and thermal sensors we decided to use a Ge absorber and a Ge NTD thermistor because they provide a simple and effective solution to achieve the sensitivity required in our search.
We have considered and used two types of Ge LDs: one simpler not fully optimized but effective and the second carefully designed. Most of our detectors are built with the first method which provides a performance good enough for our research. Our detectors have still room for improvement to get the forefront of this technology as proved by the presented advanced light detector, which shows the best performances achievable with a combination of a Ge absorber and a NTD Ge sensor.

5.3 Anti-reflective coating

An improvement in light detector design is the minimization of the reflected light that can be obtained using proper anti-reflective coating on the Ge side exposed to the luminescent bolometer in order to increase the light collection efficiency.
It is possible to calculate the absorbed fraction by using the well-known formula which provides the reflectance R for normally incident light at the interface between two media as a function of their refraction indices:

$$R = \frac{(n_0 - n_1)^2 + k_1^2}{(n_0 + n_1)^2 + k_1^2} \tag{5.6}$$

where n_0 is the real refraction index of the transparent medium and n_1 and k_1 are respectively the real and the imaginary part of the complex refraction index of the absorbing medium. In case of a vacuum–germanium interface, the absorbed light intensity (given by 1-R) is of the order of only 51% (n_1=5.48 and k_1=0.823 at 632 nm and at room temperature).
The simplest form of anti-reflective coating is based on the so called refraction index matching. If a thin layer of material with an intermediate refraction index n_i is interposed between the vacuum and the absorbing medium, we have to apply twice eq:5.6, first from vacuum to the intermediate medium (represented by the coating material) and then from the intermediate medium to the absorbing one. On the basis of these considerations a proper material which maximizes the absorption can be selected. There is an optimum value for n_i of the antireflecting material, that in the case of germanium is ∼2.4. A layer with this feature would increase the absorbed fraction up to 69%, corresponding to a gain of 35% with respect to the bare germanium.

5.3.1 Coating effect

The materials that we have deposited on our Ge light detector are SiO_2 [60] and SiO [61]. We decided to select these two materials among the possible ones as they have a refractive index close to the optimum value for germanium and they were available.
Using the refractive index tabulated data for Germanium [62], silicon dioxide [63] and silicon monoxide [64] we calculated numerically, in the range of 0.25 μm-0.82 μm, the fraction of the incident light absorbed by the detector (fig:5.5a) and the corresponding gain on the absorbed fraction (fig:5.5b) using the two different materials as coating

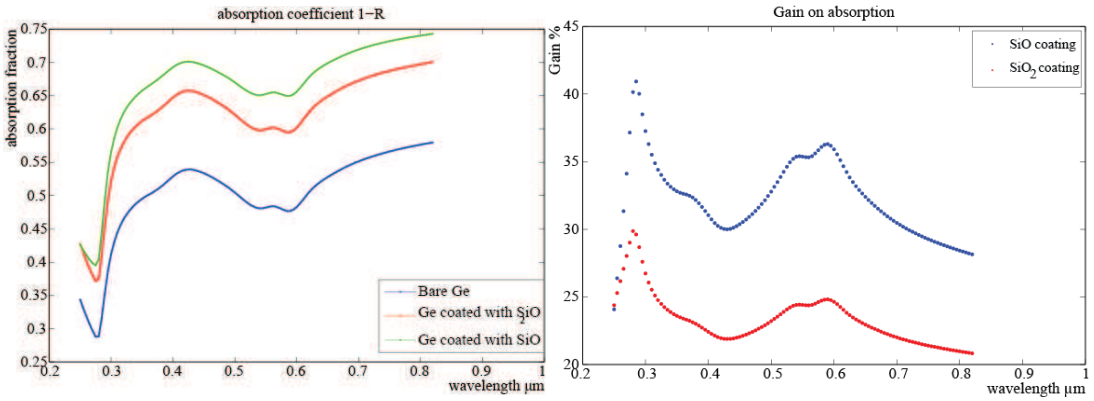

(A) (B)

FIGURE 5.5: (A) Absorbed fraction of the incident light for bare and coated Ge. (B) Gain on the light absorption of the coated Ge with respect to the bare one.

The effect of our coating is however difficult to predict, because of uncertainties in the structure and stoichiometry of the film (which affects the refraction index) and in the temperature dependence of the refraction indices. In addition, in scintillating bolometers the light output is isotropic: therefore, the assumption of normal incidence is a crude approximation. Multiple detector source reflections are not taken into account.
We expect anyway much better results with the SiO coating as fig:5.5b illustrates clearly.

5.3.2 Test set-up

Two germanium slabs were coated to be tested, one with SiO and the second with SiO_2. Four samples from each slab were cut to be tested as light detector. A dedicated set-up was developped for this purpose. The main idea was to fabricate thin detectors with a coating only on one side, and to make them as symmetric as possible with respect to the two sides in any other aspect. The same light source was then used to illuminate each light detector, in a first cryogenic run (named Run #1) from one side and in a second cryogenic run (named Run #2) from the other side (fig:5.6). In both runs on the side opposite to that of the light source, a X-ray source was placed. The detector-source geometrical coupling was identical in the two runs.
The bolometers were equipped with a resistive heater to normalize the detector performance in the two runs. In order to get a redundant confirmation of the results and to overcome inevitable small side asymmetries in the detector configuration, four bolometers of each type have been assembled. The light sources (fig:5.7.b) were performed by sending ionizing radiation on four ZnSe slabs obtained by crystalline samples. On one side of each slab, one or two drops of an uranium standard solution were deposited and then dried.
Independent measurements of the radioactive source showed that the secular equilibrium of ^{238}U was broken. A source spectral characterization showed ^{238}U α particles at 4.15 MeV (B.R. 21%) and 4.20 MeV (B.R. 79%). A weak doublet from ^{234}U was also observed at 4.77 MeV (B.R. 71.4%) and 4.72 MeV (B.R. 28.4%), with an intensity about 10 times smaller than that of the lower energy doublet. The α particles are fully absorbed by the ZnSe element, and only scintillation light is expected to exit the opposite side of the slab. We do not expect that a source energy spectrum obtained through light pulses preserves the well defined energy structure of the source with two sharp

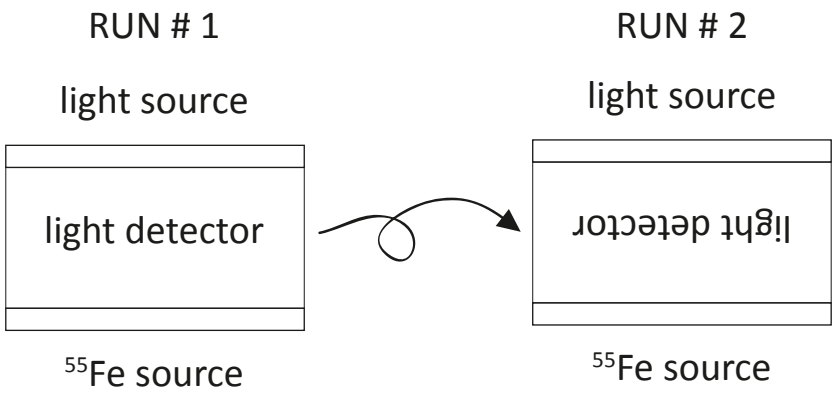

FIGURE 5.6: Scheme of the light assembly. In the two runs the light detector position is reversed in order to enlighten the two sides with the same light dource.

peaks, since the reaction of the acid with ZnSe produces an opaque region(appreciable in fig:5.7.B), with consequent partial light absorption. In the actual energy spectrum, we expect therefore a smeared structure with a low energy tail in which however the two main characteristic energies of the source (4.2 and 4.7 MeV) should be recognizable. The side where the source was deposited was covered with a reflective foil in order to increase the light emission.
The use of ZnSe as a source material ensures that the spectral features of the emitted light are similar to that expected for a scintillating bolometer; in fact the wavelength emission of ZnSe($\sim$600 nm) is close to the one of $ZnMoO_4$ and Li_2MoO_4 crystals used in this thesis.
On the opposite side of the light detectors a low rate ^{55}Fe (fig:5.7.C) was placed to provide an energy calibration with X-rays which should not be affected by the coating effects. Environmental radioactivity and cosmic rays provided a significant interaction rate in the light detectors, comparable to that due to the light sources, which resulted to be in the range 0.06–0.1 Hz. As for the light sources, the rate was in agreement with the amount of the uranium solution deposited on the ZnSe slabs.

5.3.2.1 Results on the SiO_2 coating effect

The α particles are fully absorbed by the ZnSe element, and only scintillation light is expected to exit; as said above, the two main characteristic α energies of the source ($\approx$4.2 and $\approx$4.7 MeV) should be recognizable. In order to isolate the component due to the light flashes in the energy spectrum of the detectors, we have exploited the fact that the temporal structure of the signal is different for pulses due to the light absorption with respect to pulses due to the single ionizing particles.
In order to compare the detector responses in the two runs, we have used the absolute calibration provided by the ^{55}Fe source, when it was possible; in any other case the heater signals provide a relative calibration. In the latter case we have adjusted the energy scales with an energy calibration made with cosmic rays.
The gain due to the SiO_2 coating in terms of total energy absorbed by the light detector is apparent. As an example, two light spectra collected with the LD#3 detector in the two runs are reported in fig:5.8. Similar plots are obtained for the other detectors. It is confirmed that the SiO_2 coating gives reproducible positive effects on the light collection

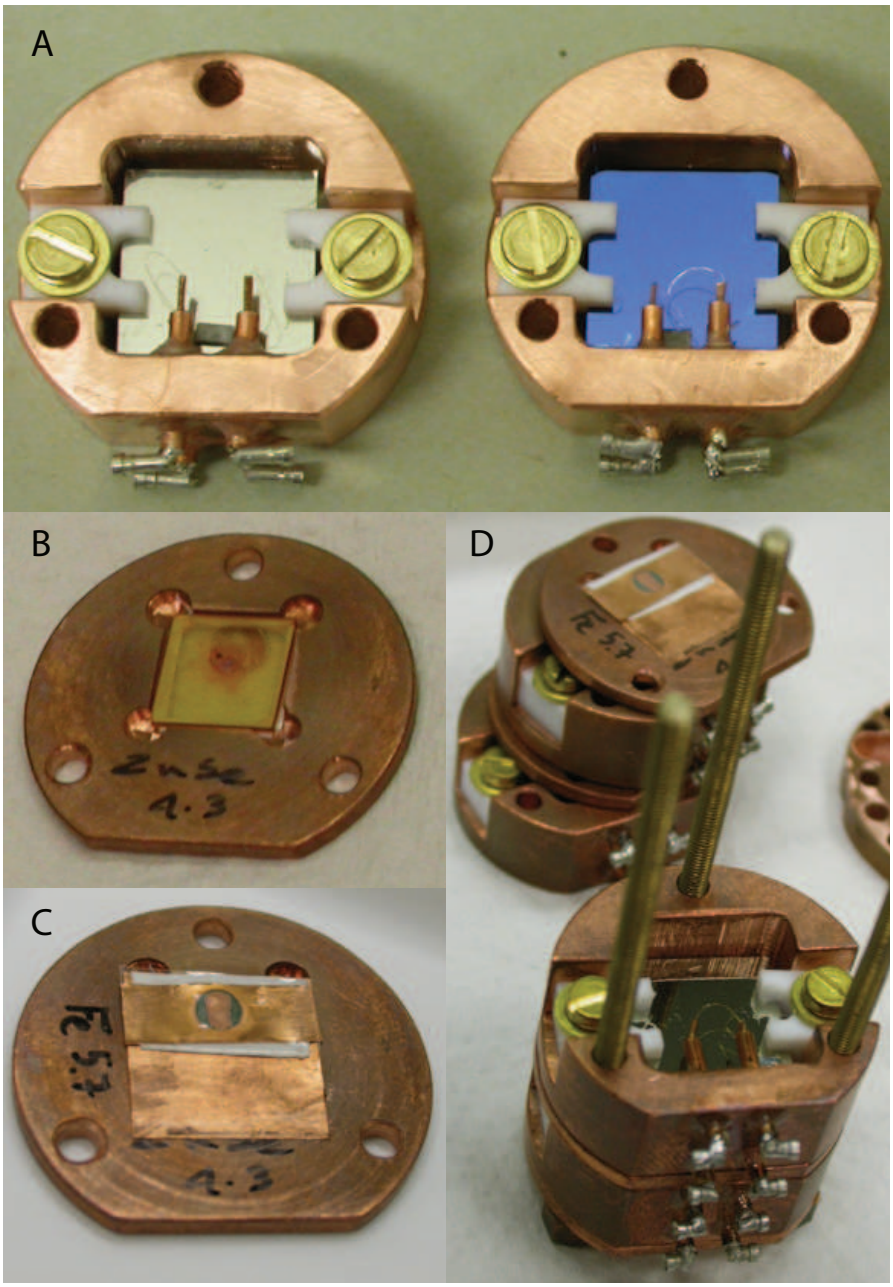

FIGURE 5.7: Pictures of the detector assembly: (A) bare Ge side (left) and coated Ge side (right). (B) ZnSe source. (C) ^{55}Fe source. (D) Detector assembly.

efficiency, which prevail over any other possible systematic factors that could simulate or fade this result.

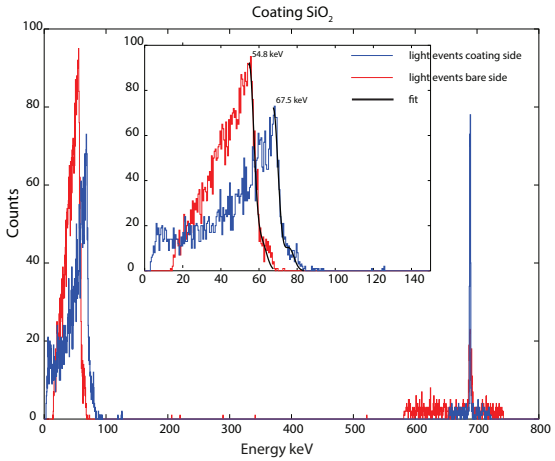

FIGURE 5.8: The energy spectra after the selection of the light pulses through pulse shape discrimination are reported for the LD#3 detector, both for Run#1 (red histogram), corresponding to a coated side and for Run#2 (blue histogram), bare side, after the normalization of the energy scale through the heater peak.

The quantification of the achieved improvement was estimated by fitting the high-energy sides of the light spectra (not influenced by light absorption in the alpha source) with a sum of two semi-Gaussian functions. The distance between the maxima of the two functions was fixed according to the positions of the two main lines of the uranium source described in sec:5.3.2. The amplitude of the gaussian at higher energy resulted always about 10 times smaller than the other gaussian, confirming a known feature of the employed alpha source. The position of the main maximum of the fitting function in Run#1 was compared with that in Run#2, taking into account their statistical uncertainties after the energy normalization (which also contributes to the global uncertainty). The results are reported in tab:5.6, in terms of the percentage improvement due to the SiO_2 coating.

detector	Improvement factor %
LD#1	18.5 ± 4.0
LD#2	19.8 ± 2.2
LD#3	20.3 ± 0.8
LD#4	20.1 ± 1.8

TABLE 5.6: Improvement factor in light absorption with a SiO_2 coated Ge.

5.3.2.2 Result on the SiO coating effect

The same data treatment was applied also to SiO light detectors. Unluckily two out of three detectors lost the electric contact during Run#2. However, taking into account the gain predictions and the agreement found with the SiO_2 coating, we present the result obtained with the last detector, namely LD#1, which worked properly. As shown in fig:5.9 a full particle discrimination was obtained; the energy calibration is provided by the 5.9 keV peak of the ^{55}Fe source. Fitting the end-points of the two light curves measured in the two runs, like in the SiO_2 case, the improvement in light collection can be estimated to be 34.3 ± 0.5 %.

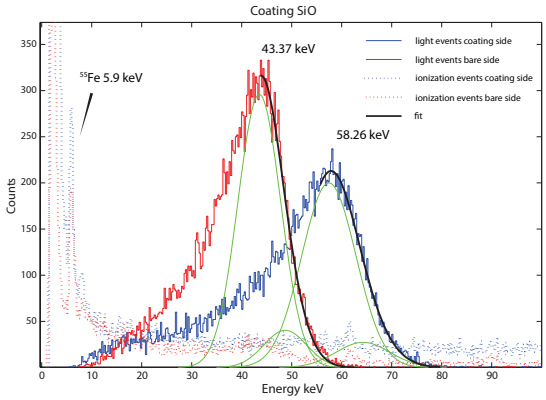

FIGURE 5.9: The energy spectra after the selection of the light pulses through pulse shape discrimination are reported for the LD#1 detector, the blue histogram correspond to a SiO coated side and the red histogram to the bare side. The dotted lines correspond to single ionization events used to set the energy scale through the 5.9 keV ^{55}Fe peak.

detector	Improvement factor %
LD#1	34.3 ± 0.5

TABLE 5.7: Improvement factor in light absorption with the SiO coated Ge.

5.3.2.3 Conclusion

The described setup has allowed to measure unambiguously the positive effect induced by the SiO_2 and SiO coatings on the Ge absorbers of bolometric light detectors in terms of the light collection. The measurement was performed in conditions very similar to those in which scintillating bolometers normally operate.
The increase of the collected light can be explained by the simple model of refractive index matching and consequently SiO coating provides a better performance, with a 34.3% increase of the absorbed light.
The results confirm that an appropriate coating procedure helps in improving the sensitivity of bolometric light detectors and can be included in the recipe for the development of an optimized radio-pure scintillating bolometer.

5.4 Neganov-Luke assisted Light detector

The Neganov-Luke effect applied on bolometric light detectors based on a semiconductor absorber represents a powerful method to enhance the thermal signal of these devices. Neganov and Trofimov [65], followed by Luke [66], discussed an interesting effect: when an electric field is applied to collect and measure the charge produced by a ionizing particle, the drift of the charges along the built-in field produces phonons. In a bolometer, the supplementary phonons increase the thermal signal proportionally to the number of produced e-h pairs. This is mostly a version of the Joule effect in a bolometric context. To evaluate the supplementary energy we consider the number of electron-hole pairs N produced by the particle interaction. Each pair has a potential energy equal to eV where e is the electron charge and V the voltage applied by the electrodes. The e-h

pairs dissipate their energy during the drift and finally are collected by the electrodes. If E_c is the energy needed to produce one pair then $N = \frac{E}{E_c}$ is the number of produced e-h pairs; the total energy E_t measured as a thermal signal after the absorption of the energy E is

$$E_t = E(1 + \frac{eV}{E_c}). \tag{5.7}$$

In germanium the energy gap between the valence band and the conduction band is 0.64 eV but when a particle interacts in the Ge medium only a part of its energy is used for electron-hole pair production. E_c then is not equal to the energy gap but should be divided by the quantum efficiency $\eta(E)$ which depends on the energy of the interacting particle becoming constant for E >2.2 eV (fig:5.10). Fig:5.10 is the only measurement of the quantum efficiency in Ge (in our knowledge) and the Ge used for this measurement was doped. We decided to include this figure to illustrate the general behavior of the quantum efficiency as a function of the photon energy. For intrinsic Ge the energy needed to produce one e-h pair with high energy photons is 3 eV.
We introduce another factor ζ which represents the fraction of e-h pairs that successfully avoid recombination and trapping at the material surface and contribute to the current useful for the Neganov-Luke (NL) effect. We can consider ζ as a quality factor. The total measured energy becomes

$$E_t = E(1 + \frac{\zeta\eta eV}{E_c}) = E(1 + \frac{V}{\epsilon}) \tag{5.8}$$

ϵ will be the parameter obtained with the fit of the experimental (E, V) points and we can consider it like the effective energy needed to create a e-h pair contributing to the NL effect. This parameter allows to evaluate the gain G achievable with the applied voltage V, $G = 1 + V/\epsilon$. It may appear that it is possible to increase the gain and the voltage without restriction. In terms of signal-to-noise ratio the achievable gain is limited by the leakage current. When the electric field is large enough, a small current starts to flow between the electrodes deteriorating the baseline noise, a fact which limits the gain.

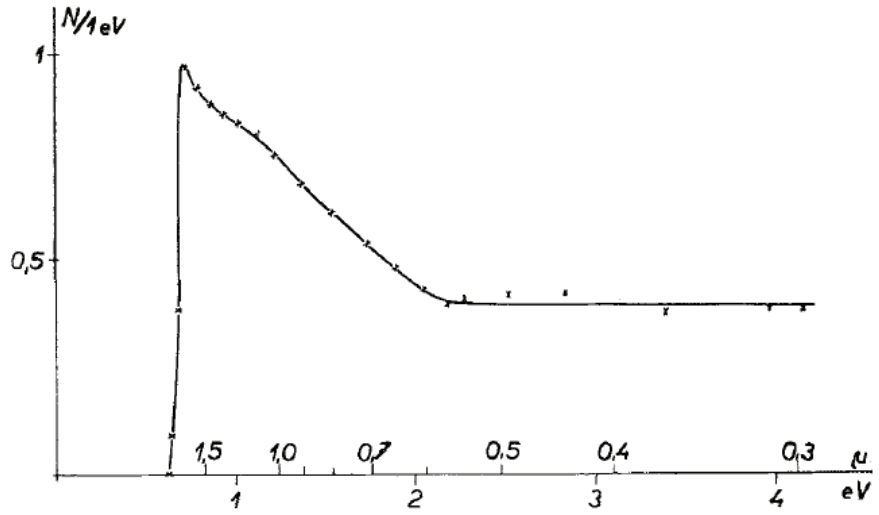

FIGURE 5.10: Number of electron-hole pairs generated in germunium by the absorption of the total energy of one electronvolt as a function of the energy of the incident radiation [67].

At CSNSM several LDs equipped with contact grids to build the electric field were produced for testing. In particular we will refer to three NL assisted light detectors. The measured detectors were equipped with different sources and measured in different setups. In the following the different conditions of the measurement environment and the different sources are presented. Then we will discuss the results for each developed detector.

5.4.1 Setup

The measurements were performed with four different high-power dilution cryostats:

- **Ulisse:** the test facility of the LUMINEU project (sec:3.2.1).
- **Cryofree:** a high power dilution unit cryostat located at CSNSM (sec:3.2.3).
- **Moulet Modan:** the test facility of the EDELWEISS experiment (sec:3.2.2).
- **Hall C cryostat:** the test cryostat located in the Hall C at LNGS (sec:3.2.4).

The acquisition system is a DC bias based Ulisse electronics (sec:4.1.1).
Each detector was equipped with different sources:

- Two different LEDs, one with a 1.4 μm wavelength and the second with a 1.6 μm wavelength.
- A ^{55}Fe source.
- A ZnSe slab crystal with a drop of liquid ^{238}U-^{235}U source to provide scintillation light in the same way as for the coating test but instrumented with a NTD thermistor to perform coincidence and simulate a scintillating bolometer.
- An optical fiber from room temperature to the bolometer. At the room temperature side of the fiber a LED with a 950 nm wavelength was installed as a light source.

We have developed and operated three NL LDs, which will be described in the next sections. All of them have the same electrode structure, an aluminum concentrically annular electrode, spaced of 4 mm, directly deposited on the bare Ge (fig:5.12). This geometry was made available by the EDELWEISS technology and for us it is convenient as the length of the carriers path is small, which reduces the probability of charge trapping.

5.4.2 Detector number 1

The first presented NL assisted LD is made by a 0.15 mm thick of ultrapure germanium slab of ⌀44 mm; it is held in a ring shape copper holder with 3 PTFE clamps and instrumented with a NTD thermistor of 3×1×0.6 mm^3. It is electrically and thermal connected by 2 gold bonding wires. The electric field is applied though aluminum electrodes deposited on Ge by evaporation using a shadow mask (fig:5.12). Even and odd

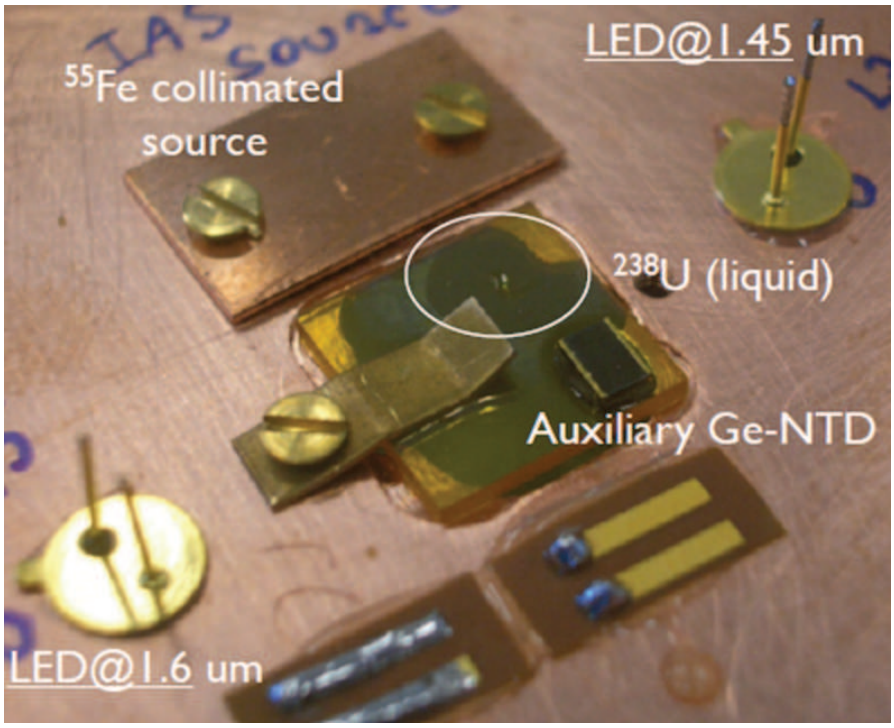

FIGURE 5.11: sources cover.

aluminum annular electrodes are respectively connected by bonding aluminum wires. V_{bias} is applied within the two sets.

The detector was cooled down to 16.7 mK in the ULISSE setup; the acquisition rate

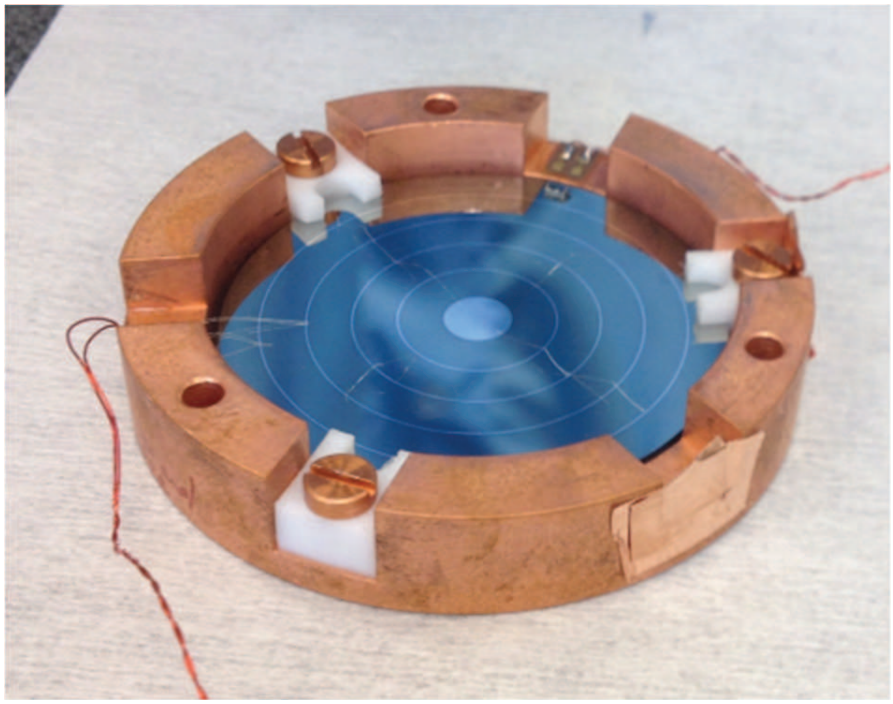

FIGURE 5.12: Neganov-Luke LD number 1.

was 20 kHz, the NTD thermistor was biased at 5 nA.

Measurement 1: the goal was to test the detector response with LED pulses. The LED was connected to a wave generator which was set to provide square pulses of 100 μs with different amplitude, from 900 mV to 810 mV with steps of 10 mV and a frequency of 1 Hz. The amplitude was changed every 3 minutes; fig:5.13a shows the measured pulse amplitude as a function of time. In fig:5.13b a zoom of the 900 mV LED pulse amplitude measurement is shown. The 'pattern' behaviors suggests an instability of the LED source that is the main origin of noise on the σ peak provided by the LED.

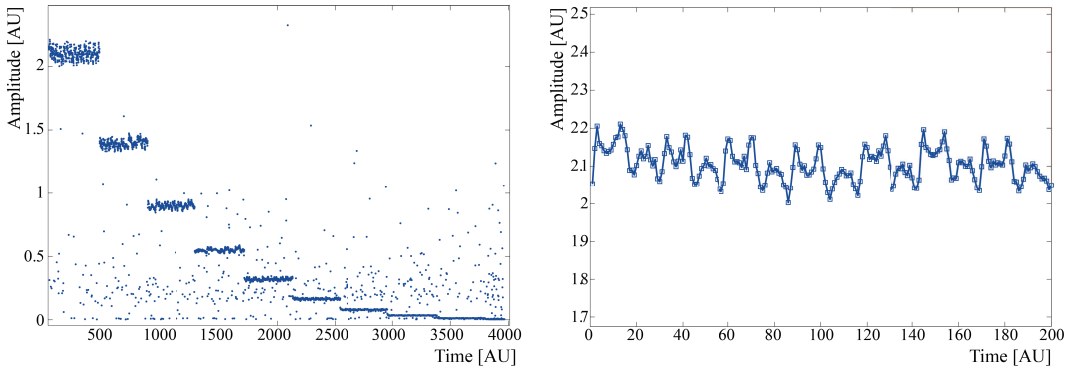

(A) (B)

FIGURE 5.13: (A) Amplitude of the LED pulses changing the voltage across the LED. (B) Zoom of the time pattern of the LED response with 900 mV squared pulses.

Measurement 2: The goal was to perform an absolute calibration of the detector with a X-ray energy scale and to characterize it in absence of the NL effect.

TABLE 5.8: Performance of the NL LD #1 without the electric field.

Sensitivity	Baseline Energy resolution σ	^{55}Fe energy resolution σ	Rise time	Decay time
0.354 μV/keV	537 eV	760 eV	0.7 ms	9 ms

The performance of this detector is a bit lifeless comparing with the average.

Measurement 3: a voltage was applied at the grids establishing an electric field in the detector. The LED provided 1 Hz pulses of 810 mV and we increased step by step the voltage V_{bias} up to 53.17 V. The voltage was provided by 9 batteries of 9 V each connected in series. Each voltage was maintained for 3 minutes; in fig:5.14a each point represents the amplitude of the LED peak at each V_{bias} with error bars at 1 σ. From the fit a value of ϵ=2.045±0.015 at 1.45 μm was found.
During the measurement the behavior changed twice. The LED was swiched off for some minutes to operate the cryogenic system and when it was on again the behavior was slightly different; this introduced a small error which is taken into account. The maximal NL gain achieved with this detector was G=27 at 53.17 V. The single LED pulse with 0 V and 53.17 V applied to the grids is shown in fig:5.14b. To evaluate the signal-to-noise ratio S/N, considering the instability of the LED, we took the average of the amplitude divided by the average of the baseline RMS just before the pulse. The gain in terms of S/N is G =19.8 at 53.17 V.
An interesting feature found in this measurement is that with a high bias on the grid we

were able to see the same instability pattern seen with large LED pulses which was not recognizable with small pulses (fig:5.14c). This was the first proof of the positive effect of the NL amplification.

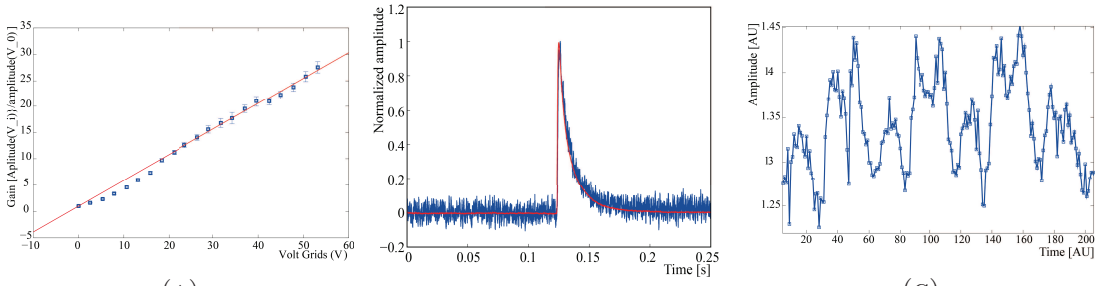

(A) (B) (C)

FIGURE 5.14: (A) NL gain as a function of V. (B) Pulse comparison (blue 0 V and red 53 V). (C) Instability pattern of the LED at 53 V.

Measurement 4: This measurement was performed to test if the NL gain degrades with time. This is a known effect of these detectors. The charges can be trapped during the drift and accumulate creating a space charge; after some time (which depends on the total rate and the detector features), the electric field generated by the space charge can partially compensate the applied one reducing the NL gain.
The LED pulse was set to 810 mV with a frequency of 0.25 Hz; a 53.17 V bias was applied at the grids. No degradation was observed in a 4 hour measurement.

5.4.3 Detector number 2

The NL light detector #2 belongs to the last generation of this kind of detectors developed at CSNSM. The ultrapure Ge wafer surface is instrumented with the electrodes and then covered with 70 nm of SiO coating. The electrode region is treated with 100 eV ionized Ar and covered with 50 nm hydrogenate amorphous Ge before the aluminum deposit.
A $3\times1\times0.6$ mm^3 NTD Ge thermistor was used for the temperature readout; it is electrically and thermally connected with two gold bonding wires of Ø25 μm.
For the measurement the detector was instrumented with the source cover (fig:5.11), it was measured in the Moulet Modane cryostat at different temperatures: 30 mK, 22 mK, 20 mK and 16.5 mK. We report the best result achieved at 20 mK, with a bias current on the NTD thermistor of 8.32 nA.

Measurement 1: The goal was to perform an absolute calibration of the detector with a X-ray energy scale and to characterize it in absence of the NL effect.

TABLE 5.9: Performance of the Neganov-Luke LD #2 without the NL effect.

Sensitivity	Baseline Energy resolution σ	^{55}Fe energy resolution σ	Rise time	Decay time
0.527 μV/keV	91.5 eV	147 eV	0.9 ms	7.9 ms

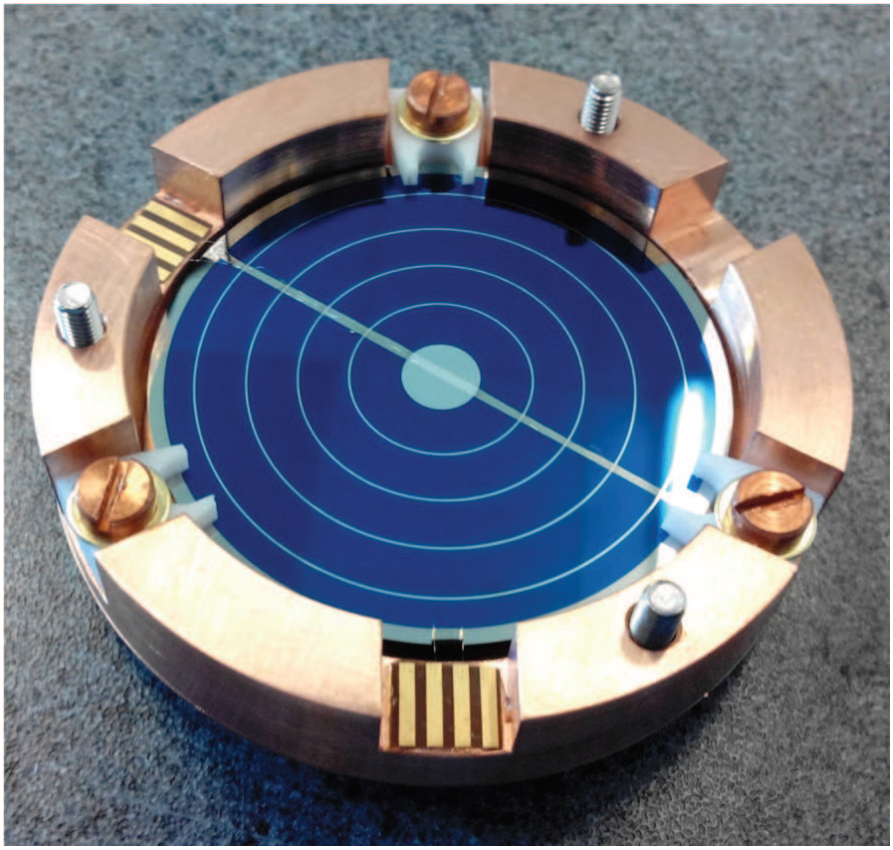

FIGURE 5.15: Picture of the NL light detector #2.

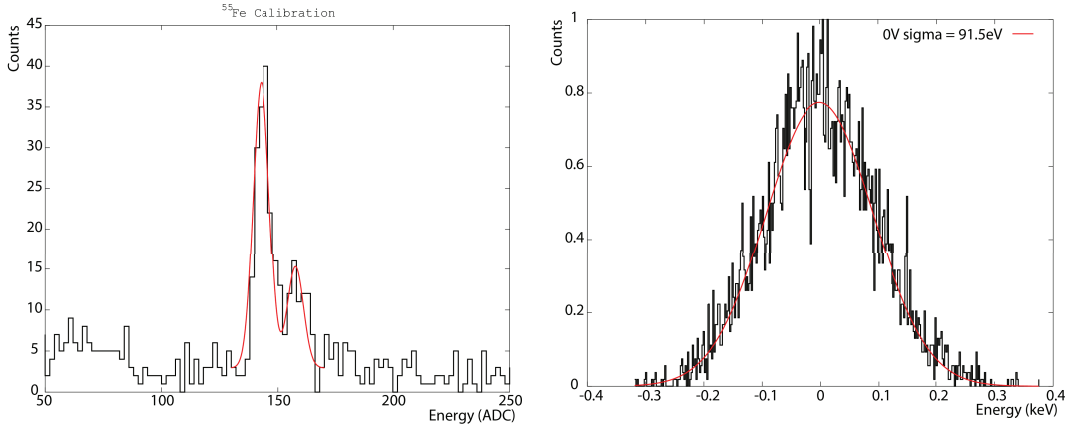

(A) (B)

FIGURE 5.16: (A) ^{55}Fe calibration. (B) Baseline resolution.

Measurement 2: the NL amplification was tested using the cold Hamamatsu LED L8245 with a wavelength of 1.65 μm. The LED was not stable in time like in the previous case, so the amplitude corresponds to the average of a large number of pulses and the noise is the RMS of the baseline during the measurement. From the fit in fig:5.17a we get ϵ=1.68 at a 1.65 μm wavelength.
Fig:5.17b shows the baseline noise RMS as a function of the applied V_{bias}; the noise remains stable till 80 V. This noise degradation can be explained by the appearance of a small leakage current on the detector surface.

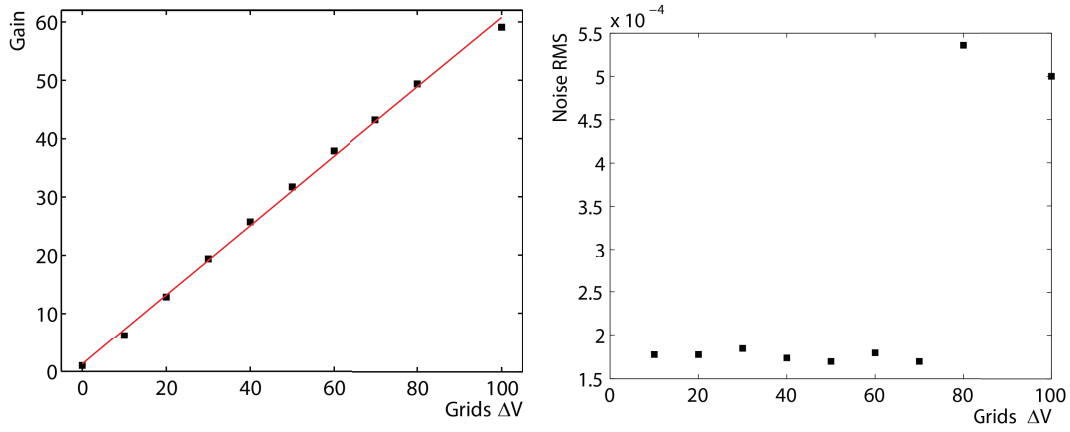

(A) NL Gain (B) NL Noise

FIGURE 5.17: (A) Pulse amplitude versus V_{bias}. (B) RMS baseline noise versus V_{bias}.

Measurement 3: it is focused on the evaluation of the effective advantages that could be achieved applying the NL effect in a scintillating bolometer measurement. Here we used the small NTD equipped ZnSe slab as a 'scintillating bolometer'.
The two components, ZnSe and the light detector, were laying horizontally so that most of the coincidences were provided by cosmic muons crossing both. A stringent pulse shape cut was applied on the light signal shape to select only the scintillating events.
We applied three different electric field values on the light detector in order to compare the scatter plots. The applied voltages were 0 V, 70 V and 90 V.
At high energies the error associated to the scintillation peak is dominated by the statistical collection of photons, which is irreducible. On the contrary, at low energy, where the signal-to-noise ratio is smaller, an effective improvement was achieved. In practice, the energy where the separation of the LY bands occurs becomes lower.
Fig:5.18 shows the three Q-plots together; on the ordinate, the measured light energy is expressed in output V to show the different responses of the detector. The black dots, corresponding to the measurement at 0 V, are squeezed in the lower part of the plot as the LD response with an applied electric field is much larger.
Fig:5.19 presents the comparison between the 0 V and 90 V measurements: at high energy the discrimination power is almost the same but at low energy the intersection of the bands shifts to a lower energy when a 90 V bias is applied to the detector. In particular the intersection of the zero light band and the γ/β band moves from 154 keV to 60 keV.
These events with zero light output (dark events) are sometimes observed: they can be due to a shaded interaction or to an energy deposit in non scintillating parts thermally connected to the detector.

5.4.4 Detector number 3

Detector # 3 is a twin of the previous one (fig:5.12). This time the measurement was performed in the Cryofree cryostat and the detector was equipped with a room temperature LED source driven to the detector using an optical fibre. The chosen LED was an OSRAM LED L271 with a wavelength of 0.95μm. The main purpose of the run was to test the NL amplification with a stable light source. The optical fibre allows to understand better the stability of the detector when an electric field is applied.

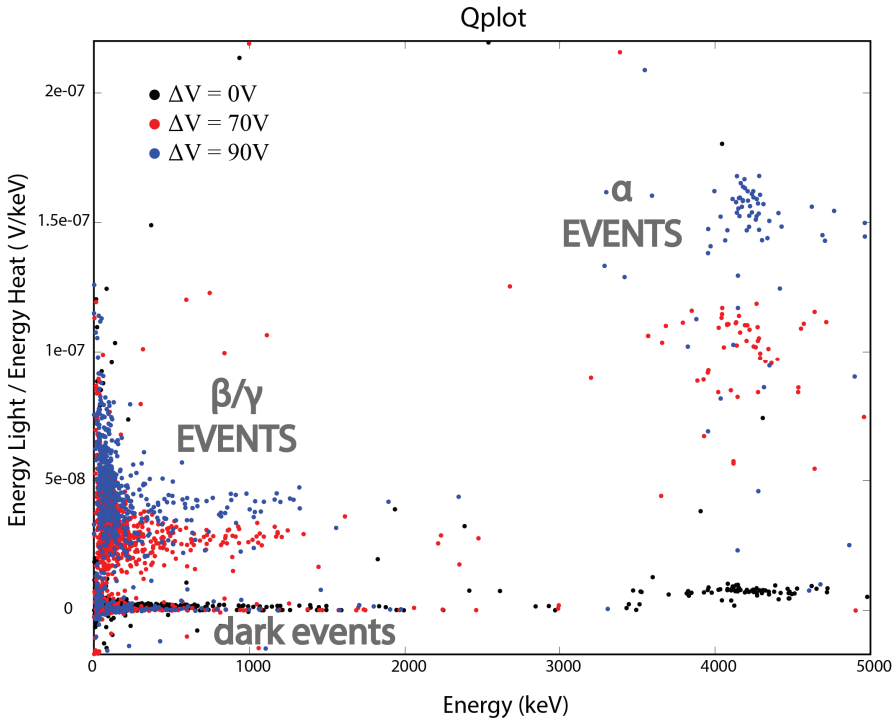

FIGURE 5.18: Comparison of three Q-plots with different V_{bias}. The light output is shown as a function of the voltage response of the detector.

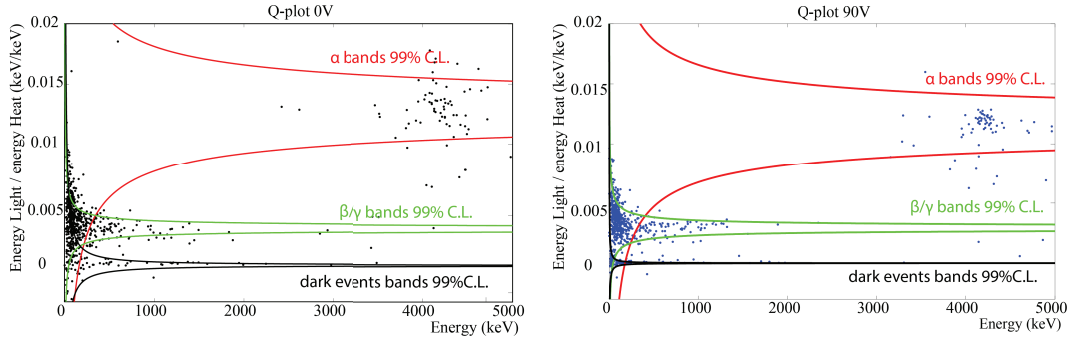

(A) (B)

FIGURE 5.19: (A) Q plot with V_{bias}=0 V. (B) Q plot with V_{bias}=90 V.

This setup had not a mechanical decoupling at the mixing chamber stage. The cooling machine provides a huge source of microphonics noise, which degrades the general performance of the detector becoming a perfect test workbench for the NL-effect.

Measurement 1: the absolute calibration this time is made with cosmic rays (fig:5.20a) because the huge microphonics noise and a lot of low energy background events (this set-up is not shielded) hid the 5.9 keV peak of ^{55}Fe. The energy spectrum of the cosmic muons at the minimum of ionization is described with the Landau function [68] which is

$$f(E) \approx \frac{1}{\sqrt{2\pi}\xi} e^{-\frac{1}{2}\left(\frac{(E-E_0)}{\xi} + e^{-\frac{(E-E_0)}{\xi}}\right)} \tag{5.9}$$

in the Moyal approximation [69]. E_0 is a location factor and ξ is a scale factor.
Fig:5.20 shows the energy spectrum with the fit of the cosmic muons bumps: the figure on the right reports the amplitude of the LED pulses as a function of the applied voltage; the curve is fitted with the LED power law assuming that the emitted light is proportional to the power dissipated in the device.
The resulting characteristics of this detector are reported in tab:5.10.

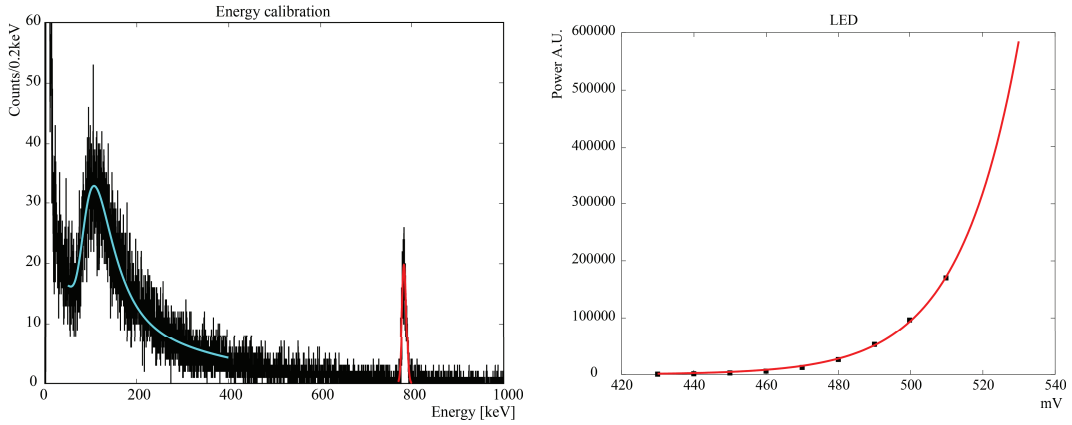

(A) (B)

FIGURE 5.20: (A) Detector calibration with the cosmic muons (blue line). (B) LED characterization.

Sensitivity	Baseline Energy resolution σ	^{55}Fe energy resolution σ	Rise time	Decay time
0.597 μV/keV	287 eV	-	1.5 ms	16 ms

TABLE 5.10: Performance of the Neganov-Luke LD #3 whithout the NL effect.

Measurement 2: it is an absolute calibration with photons using only the LED source. We provided different pulse amplitudes changing the width of the pulse wave function which drives the LED. For each amplitude we collected about 300 pulses. All the peaks were fitted with a gaussian function (fig:5.21a). The resolution of the peak is the squared sum of different contributions; without any voltage applied at the grids, the total σ of a peak is due to the baseline noise plus the statistical uncertainties of the photon collection:

$$\sigma^2_{tot}(x) = \sigma^2_0 + \sigma^2_{ph}(x); \tag{5.10}$$

σ_{ph} follows a poissonian statistics of counting, and for a large number of photons N

$$\sigma_{ph} = \sqrt{N}. \tag{5.11}$$

If x is the position of the peak with unknown energy, we can express the generic $\sigma_{ph}(x)$ as a function of a specific one (x_0):

$$\sigma_{ph}(x) = \sqrt{\frac{x}{x_0}}\sigma_{ph}(x_0) \tag{5.12}$$

Fig:5.21b shows a fit using eq.5.10 in which $\sigma_{ph}(x_0)$ and σ_0 were left as free parameters. Knowing the energy of the single photon, which is fixed by the LED characteristics, it

is possible to reconstruct the absolute energy of the pulses. With this information the sensitivity of the detector can be calculated and it is shown in tab:5.12.

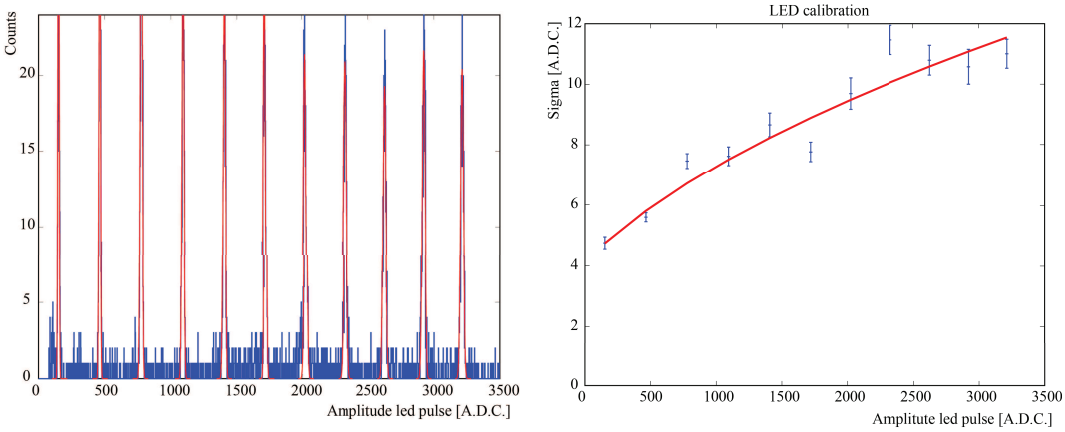

(A) (B)

FIGURE 5.21: (A) LED pulses peaks fitted with a gaussian function. (B) Fit of the sigma obtained with the LED pulse with eq:5.10.

Measurement 3: its purpose was to evaluate the NL effect with a stable light source. This time, for the lower energy light pulses the dominant source of noise is σ_0 (no systematic pattern is present unlike the cooled LED case) and the NL effect can play a role to improve the energy resolution for this light peak. The measurement is done as follows: for each voltage applied to the grids, 300 pulses of each amplitude were acquired. For each pulse amplitude, a fit is performed to get the energy of the pulse and the resolution.
In fig:5.22a, the amplitude for a selected pulse is plotted as a function of the voltage applied to the grids; from the slope of the linear fit we get ϵ =2.94 for a 950 nm wavelength.
The effect on the energy resolution of the NL effect is shown in fig:5.22b, where the noise-to-signal ratio is plotted versus the voltage applied to the grids; for the low energy pulses the gain on the energy resolution is clearly visible while for the high energy pulses, where σ_{ph} is dominant, there is no effect on the energy resolution. From the figure it is visible that V_{bias}=12 V applied to the grids is enough to reach the statistical limit of this measurement (straight line).

Measurement 4: With the optical fibre, we found another way to characterize and calibrate the detector using the properties of the NTD Ge thermistor.
The base temperature was raised up to 70 mK where the electron-phonon coupling is stronger.
The main idea was to power the LED continuously, changing the temperature of the detector from T_1 to T_3 heating it with the radiation power. The temperature was measured with the NTD resistance, which changed from R_1 to R_3. After this measurement, when the detector cooled down again to R_1, we changed the working point of the detector modifying the current bias till the NTD resistance R_2 was equal to R_3.
If R_2=R_3, the Joule power dissipation ΔP_{2-1} and the light radiation power ΔP_{3-1} are equal too. From this resistance measurement, the power Q provided by the LED can be calculated:

$$R_2 = R_3 \longrightarrow \Delta P_{2-1} = \Delta P_{3-1} \tag{5.13}$$

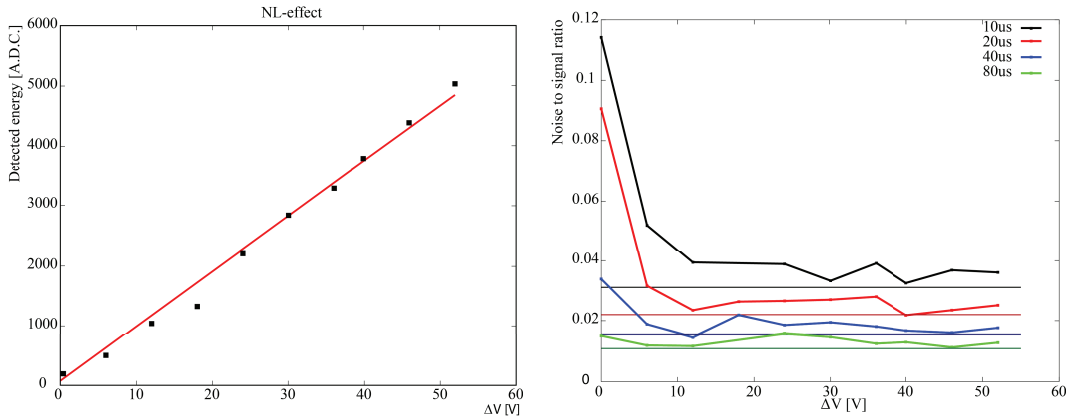

(A) (B)

FIGURE 5.22: (A) Fit of the amplitude versus V_{bias}. (B) Noise-to-signal ratio as a function of V_{bias}.

$$\Delta P_{2-1} = I_2V_2 - I_1V_1 \quad \text{and} \quad \Delta P_{3-1} = Q + I_1V_3 - I_1V_1 \tag{5.14}$$

Once we know the power Q injected by the LED at a certain V_{LED}, we can set a square

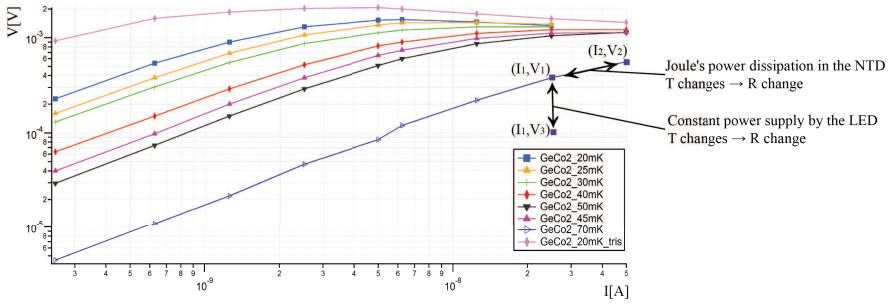

FIGURE 5.23: VI curve of the detector, the working point (I_1, V_1) was used as starting point for the measurement.

pulse with the same V_{LED} adjusting the duration (width) to inject the desired energy. For example: we used the LED with a $V_{LED} = 430$ mV amplitude and the corresponding power is Q=22 pW. This corresponds to an energy of E=5.7 keV for a 40 μs pulse width of 430 mV. Using these pulses for an energy calibration, the sensitivity of the detector is 636 μV/keV to be compared with the other calibration method (tab:5.12).

5.4.5 Conclusion

We successfully tested a few cryogenic LDs with Neganov-Luke amplification; the performance of the detector has clearly been improved. The results are very promising for future applications.
Our detectors can handle 80 V without observing any deterioration of the baseline noise; the grids are deposited on a polished surface, spaced of 4 mm and covered with SiO.
The NL effect was tested with three different light wavelengths for which the gain as a function of the voltage applied at the grids was linear; fits of the amplitude versus voltage were done and the found ϵ factors (see eq:5.8) are reported in tab:5.11.
An important technical point that we have highlighted is that the optic fibre provides

a stable light source as confirmed by the three independent calibration methods on detector #3 (tab:5.12).

Detector	LED wavelength [μm]	photon energy [eV]	ϵ
Detector #1	1.45	0.855	2.05
Detector #2	1.65	0.751	1.68
Detector #3	0.95	1.305	2.94

TABLE 5.11: Value of ϵ founded with three different light source.

Calibration method	Sensitivity [μV/keV]
Cosmic muons	0.597
Poissonian statistics of photon counting	0.603
LED power flux and Joule dissipation	0.636

TABLE 5.12: Sensitivity of the NL Detector #3 calculated with three different calibration methods.

This technology finds immediately place in two applications to solve problems which are hot topics at present:

- Concerning the pileup issue in rare event searches with massive scintillating bolometers, the use of the faster response of light detectors to recognise the pileup events would be advantageous. The smallness of the light signal does not allow to perform efficiently a pulse shape analysis, but thanks to the NL effect their signal-to-noise ratio can be substantially increased and therefore the light signal can be used to recognize pileup more efficiently.

- In case of bolometers made with a high-gap transparent but non scintillating material, Cherenkov light would be emitted after the interaction of fast enough particles. In this context, the NL Detector #1 was operated in the Hall-C facility at LNGS coupled to a non-scintillating TeO_2 crystal. A Cherenkov light emission was observed for electrons and gammas thanks to the high sensitivity provided by the NL effect induced by 90 V applied to the detector [70].
  The amplitude of the light signal at 90 V was a factor 9.7 larger with respect to the configuration with no applied field (0 V). The detector RMS baseline noise was reduced from 185 eV at 0 V to 19 eV at 90 V being able to measure the emitted Cherenkov light. We evaluated a discrimination power between α's and β/γ's in the ROI of 2.7 σ (fig:5.24).

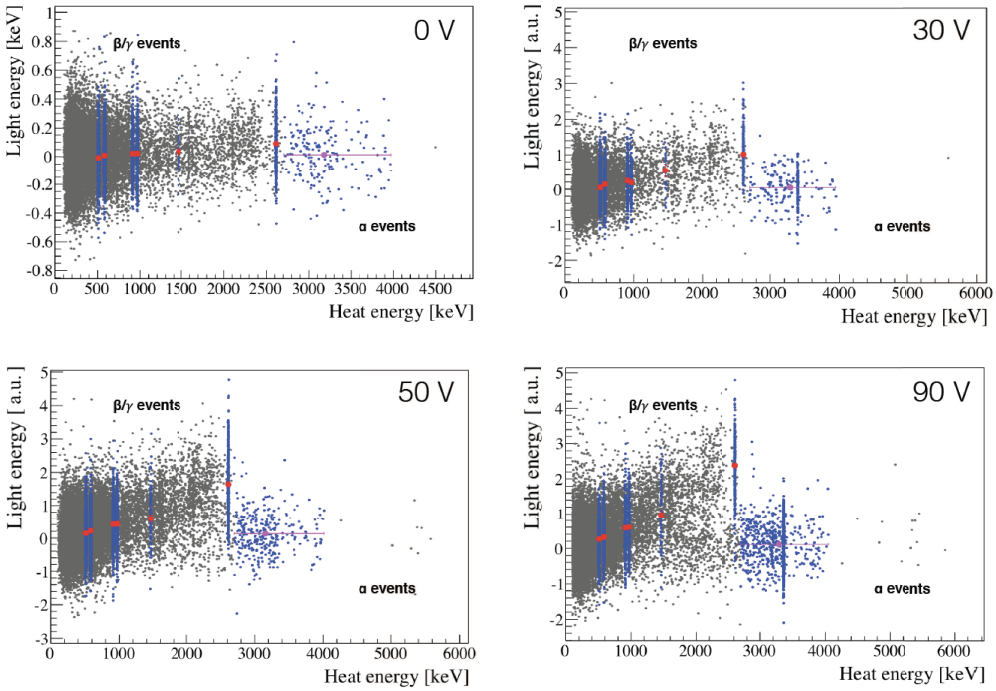

FIGURE 5.24: NL light detector #1 operated at the Hall-C cryostat coupled with a TeO_2 crystal. The DP increases as V_{bias} increases [70].

Chapter 6

LUMINEU $ZnMoO_4$ scintillating bolometers

This PhD activity started simultaneously with the LUMINEU project: I have therefore the chance and the pleasure to review the development and the achievements in this research framework, in which I have been deeply involved.
LUMINEU (Luminescent Underground Molybdenum Investigation for NEUtrino mass and nature) is a successful project that aims to develop a technology based on scintillating bolometers for high sensitivity searches for neutrinoless double beta decay. The project started in 2012 and in fall 2015 is about to end with the high sensitive measurement of two large scintillating bolometers made of $Zn^{100}MoO_4$ enriched crystals. The crystal production is a hard task as this compound is very difficult to crystallize; indeed the best results on the growth of this material were obtained by our collaborators from the NIIC institute in Novosibirsk.
The final goal of the LUMINEU project is to demonstrate that a ton scale experiment based on the same technique can be sensitive enough to explore the parameter space of the inverted hierarchy region of the neutrino mass pattern. In view of this ambitious goal we have to proof the possibility to obtain a specific background level of the order of 10^{-4} $\frac{\text{cts}}{\text{keV}\times\text{kg}\times\text{y}}$ in the region of interest.
The whole LUMINEU project involves the following items: the optimization of the crystal production process in terms of radio-purity and of the yield of the crystal boule; the development of prototype scintillating bolometers capable to fulfill the requirements of the final experiment (i.e. energy resolution and particle discrimination power); finally, a long measurement campaign in deep underground condition to precisely evaluate the internal residual contamination. The project involves also light detector optimization and the the development of the bolometer phonon sensors.
This chapter describes the development of the prototype detectors based on $ZnMoO_4$ and the results of the measurements, from the working tests to the radioactive contaminants measurements. To approach a hypothetical large scale final experiment, the characterization of side components and building tools was done and these parts are also described.

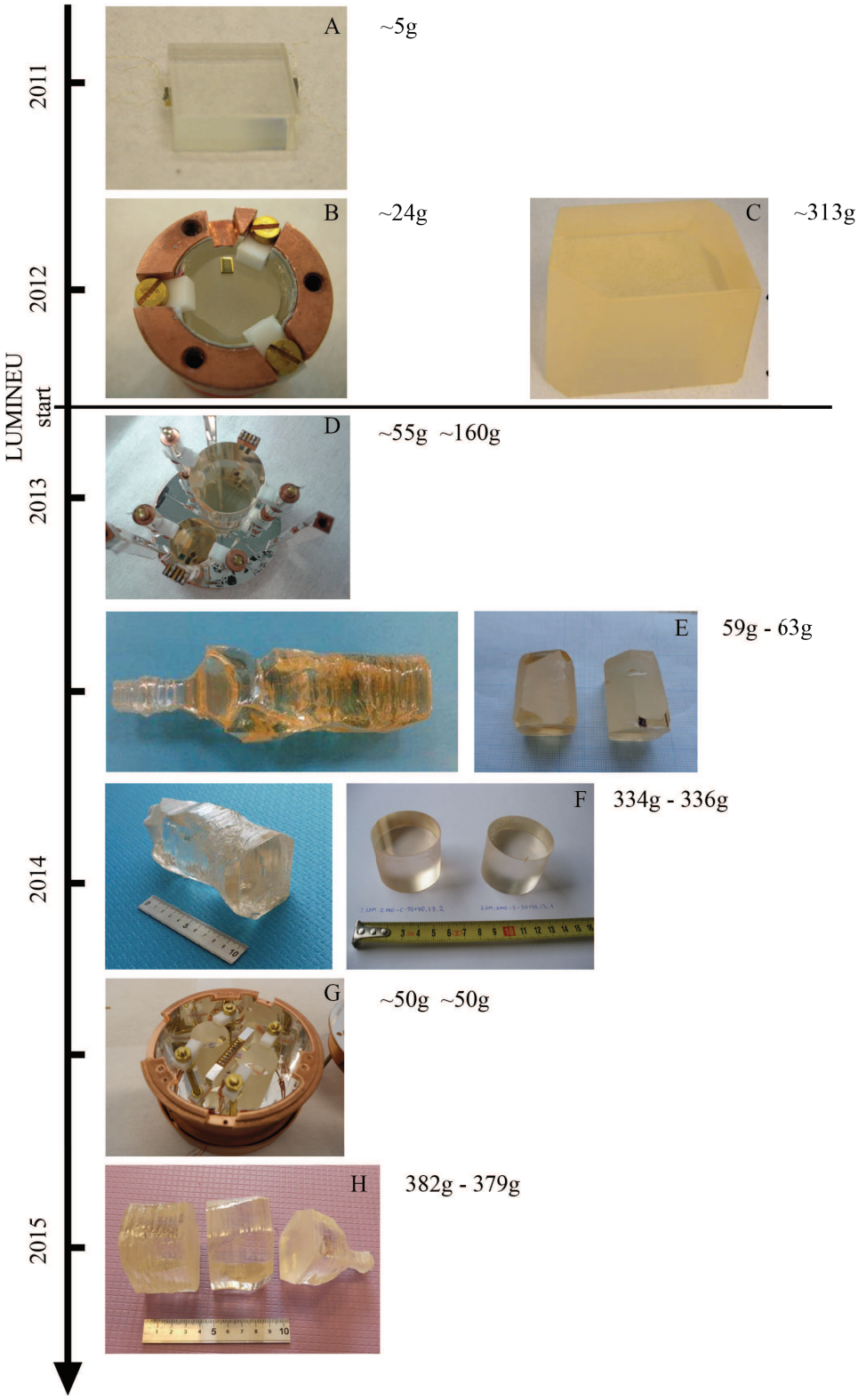

FIGURE 6.1: $ZnMoO_4$ crystals produced for bolometric tests and material characterization.

6.1 Before the LUMINEU project

In 2006 the $ZnMoO_4$ compound in form of poly-crystals was studied and proposed to be used as an appropriate detector material to search for neutrinoless double beta decay of ^{100}Mo [71]. After a few attempts to grow crystals out of this material [72, 73], in 2010 high-quality $ZnMoO_4$ crystals were produced for the first time in the Nikolaev Institute of Inorganic Chemistry (NIIC, Novosibirsk, Russia) by using the low-thermal-gradient Czochralski technique (LTG Cz) [74] in a platinum crucible. A significant improvement of the crystal quality was achieved thanks to the development of a dedicated purification technique consisting in a deep chemical purification of molybdenum (in the form of MoO_3), with the goal to get rid of the metal contamination which degrades the optical properties. Three $ZnMoO_4$ crystals up to 25 mm in diameter and 60 mm in length were grown.
Before we decided to investigate the $Zn^{100}MoO_4$ as a candidate compound for a bolometric experiment on $0\nu\beta\beta$, few detectors were produced tor test and validate the approach and the feasibility of a project based on this technology.
The first scintillating bolometer prototype was made of a small parallelepiped ($15\times15\times5$ mm^3) sample of $ZnMoO_4$ of about 5.07 g (fig:6.1.A), obtained from high quality crystals produced at NIIC and described in detail in [42]. After preliminary investigations on the optical quality of the crystal [75][76], a test of this bolometric detector has been performed aboveground in the cryogenic laboratory of the University of Insubria (Como, Italy) and in the Centre de Sciences Nucléaires et de Sciences de la Matière (Orsay, France).

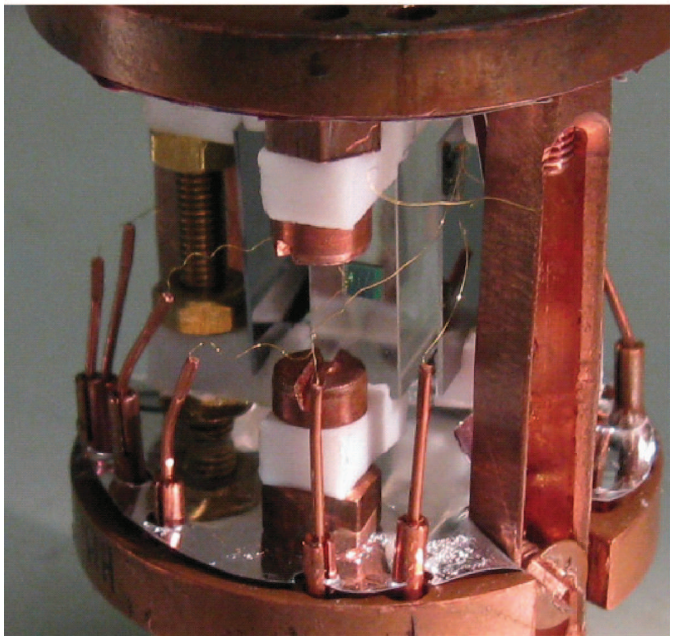

FIGURE 6.2: First prototype of a $ZnMoO_4$ scintillating bolometer. In the centre the crystal absorber is held by PTFE pieces, two Ge LDs face the two opposite squared sides.

The detector (Fig.6.2) consists of a $ZnMoO_4$ crystal faced by two light-detecting ultra-pure Ge thin slabs of 15×15×0.5 mm^3. The three bolometers were held in a copper holder by two PTFE elements each and surrounded by a highly reflective polymeric multilayer foil (Radiant Mirror Film VM2000/VM2002 from 3M). The thermal signals from the $ZnMoO_4$ crystal and the two Ge slabs were readout by three nominally identical neutron transmutation doped (NTD) Ge thermistors. In some runs, radioactive sources were placed in the proximity of the detector for calibration purposes. In particular, a collimated ^{241}Am source, characterized by a main α line at 5.48 MeV and an intense γ line at 59 keV, illuminated the $ZnMoO_4$ crystal at the centre of a 15×5 mm^2 face. Two weak ^{55}Fe sources irradiated the external side of each Ge slab. The detector was operated at various base temperatures – between 25 and 32 mK – in two dilution refrigerators.

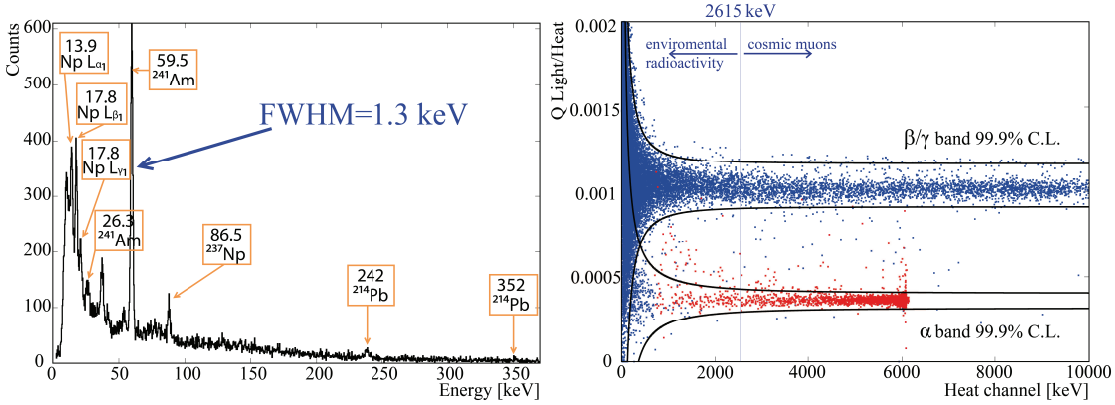

FIGURE 6.3: Left: Energy spectrum where can be appreciated the excellent energy resolution on the ^{241}Am X-rays. Right: A Q-plot.

The good performance obtained aboveground for this detector (fig:6.3) stimulated the R&D on this subject: a second sample larger than the previous one was obtained from another crystal among those mentioned above. The new device was tested in the Orsay apparatus; it was based on a 23.8 g $ZnMoO_4$ crystal with an almost cylindrical shape, with a height of 28 mm and a diameter of 16 mm (fig:6.1.B). Similarly to the smaller detector, the crystal was kept firmly in position by six PTFE elements clamping it at the two flat sides.

Two light detectors, consisting of square hyper-pure Ge crystal slabs with a size of 15×15×0.3 mm^3 were facing the $ZnMoO_4$ crystal flat sides. This time each Ge slab had an independent holder, in a configuration similar to that described in Sec.5.3.

The best performances in both detectors were obtained with typical NTD thermistor resistances of the order of 1 MΩ, with bias currents in the range 2–5 nA. The typical temporal structure of the pulses is characterised by rise times in the 1 ms range and decay times in the 10 ms range. The signals from the NTD thermistors were amplified by low noise voltage amplifiers (sec:4.1.1). The data acquisition system allowed the registration of the full waveforms of the signals; optimum filtering was applied offline in order to maximize the detector energy resolution (sec:4.3). The results on these detectors are reported in tab:6.1. A further step in the $ZnMoO_4$ production was the increase of the crystal volume. In 2011 a first large zinc molybdate crystal boule with a length of about 14 cm and a mass of ∼0.9 kg was grown at NIIC. The crystal growing and the purification techniques were the same as before, however the overall quality deteriorated. Two samples, with irregular shape in order to preserve a mass as large as possible, were cut from this boule. A $ZnMoO_4$ cristal with a mass of 329 g was used for low temperature tests at LNGS [77]; the second sample with a mass of 313 g (fig:6.1.C) was used to build

TABLE 6.1: Measured parameters of the 5.07g and 23.8g $ZnMoO_4$ detector

Parameter	5.07g	23.8g
Sensitivity μV/MeV	200	77
Energy resolution Bsl_{FWHM} keV	0.82	1.5
Light Yield keV/MeV	2.1	1.8
Quenching light α/β	0.17	0.19

a LUMINEU precursor scintillating bolometer shown in fig:6.4. The transparency of the

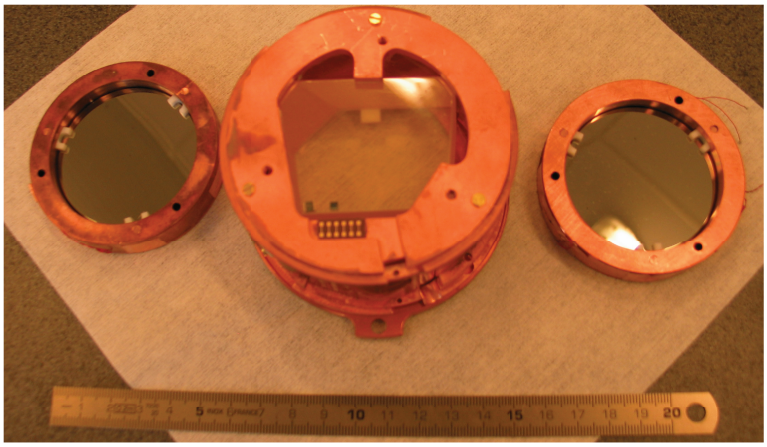

FIGURE 6.4: picture of the LUMINEU precursor bolometer detector. The crystal has a mass of 313 g.

crystal indicates a low concentration of metals but a precise investigation on dangerous radioactive contaminants was needed. for this reason, we developed a bolometric detector built with radio-pure materials following a procedure aiming at reducing the contact with possible contaminations. No special surface treatment was done except wiping with ultra-pure ethanol.
The crystal was instrumented with two temperature sensors consisting of NTD Ge thermistors and it was fixed inside a copper holder by using PTFE supporting elements. The NTD thermistors were glued by using six spots 25 μm thick of Araldite epoxy glue. Two light detectors, consisting of $\oslash 50 \times 0.25$ mm^3 Ge slabs instrumented with a NTD sensor, were mounted 5 mm far from the upper and lower surfaces of the crystal in order to collect the emitted scintillation light; these light detectors belong to th easy-assemblye family (sec:5.2.1).
After a working test in the Moulet-Modane facility, the crystal was moved underground at the LSM where it was tested in the EDELWEISS setup. The data were acquired during the EDELWEISS-III commissioning run with other 15 ultra-pure germanium detectors of 0.8 kg each. The data were recorded with a 2 kHz sampling rate and an online trigger was used. The overall background measurement lasted 290 h live time. The energy scale of the heat channels of the $ZnMoO_4$ absorber was determined mainly with the γ's provided by a ^{133}Ba calibration source, used in the standard EDELWEISS calibration procedure, which is performed periodically. In addition, one calibration measurement was performed with the γ's provided by a ^{232}Th source made of thoriated tungsten wires

with a total mass of 15.2 g containing 1% of thorium in weight. We removed a ^{55}Fe X-ray source from our light detectors, in order to avoid any possible radioactive contamination of the inner volume of the cryostat, which is normally used for dark matter searches. The registered data were then analysed with the optimal filter technique and the calibration spectra are shown in fig:6.5. The energy resolution FWHM, reported in tab:6.2, is good. The resolution degrades at the high energy γ's lines due to pileup effects caused by the considerably high activity of the ^{232}Th source.

A scatter plot of the ^{232}Th calibration over 51 h is shown in fig:6.6 which confirms the

TABLE 6.2: Measured energy resolution on several γ lines suring calibration

	0 keV BSLN	356 keV ^{133}Ba	911 keV ^{228}Ac	2615 keV ^{232}Th
Energy resolution FWHM keV	1.5	7	10	17

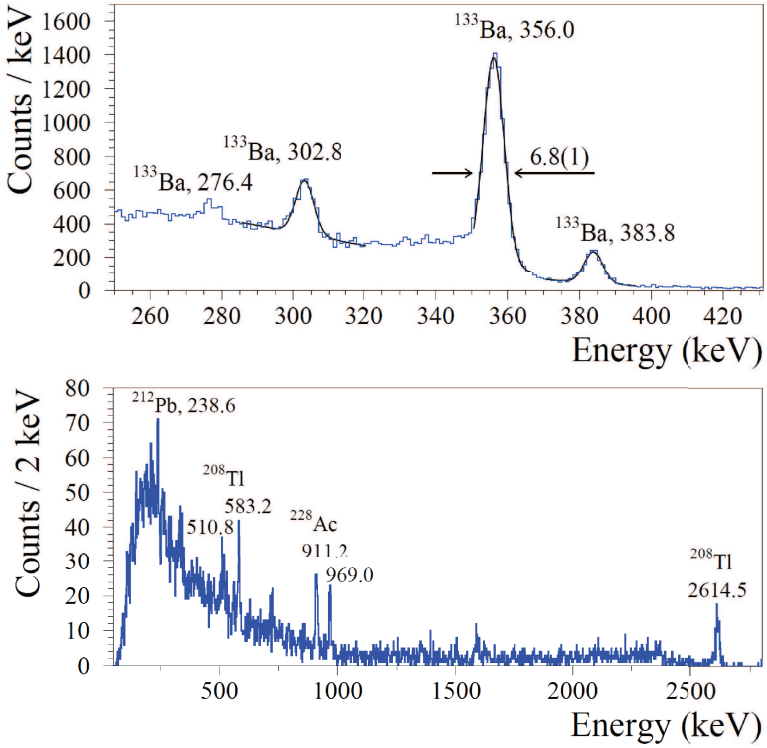

FIGURE 6.5: Calibration spectrum obtained during the underground calibration measurement of the LUMINEU precursor. Up: ^{133}Ba source. Down: ^{232}Th source.

powerful particle identification capability of the $ZnMoO_4$ scintillating bolometer.

The level of radio-purity was evaluated by using the data of the low background measurements plus the calibration runs in order to increase the statistics. To evaluate the contaminants we used the α's above 3 MeV; in fact, this energy region is mainly populated by α's emitted by the radionuclides of the U/Th chains. An α spectrum over 249 h is shown in fig:6.7. A clear peak due to internal and external activity of ^{210}Po at 5.4 MeV is visible. This sample was measured several times in different periods and the activity of ^{210}Po remained almost constant in time, showing that the ^{210}Po activity is mainly due to its progenitor ^{210}Pb (Qb = 63.5 keV, half life = 22.3 yr). We stress that neither ^{210}Po nor ^{210}Pb are harmful for the $0\nu\beta\beta$ decay search of ^{100}Mo, since they cannot populate the region of interest around 3034 keV thanks to the excellent α/β rejection power. Few other radioactive nuclides were found: a list of contaminants is

reported in tab:6.7.

The LUMINEU project started on the basis of the results achieved with this precursor

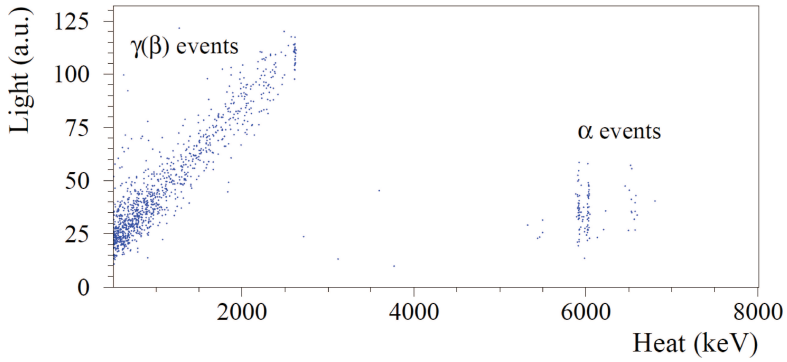

FIGURE 6.6: Scatter plot obtained with the 313 g detector (LUMINEU precursor). The excellent particle discrimination power is appreciable. Some α particles leak in the ROI and thanks to the lower LY are simply recognisable.

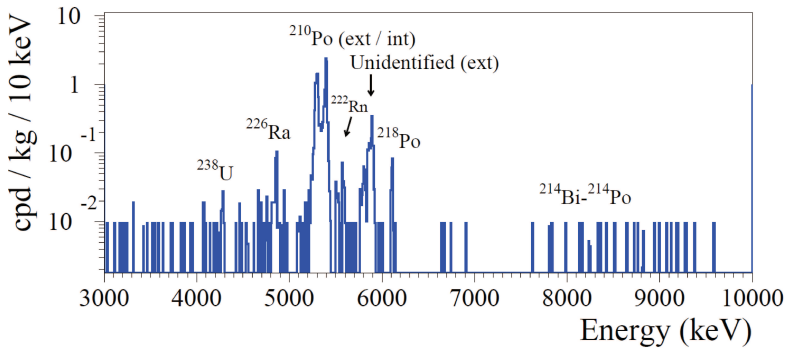

FIGURE 6.7: α spectrum of the LUMINEU precursor.

large detector.

6.2 $ZnMoO_4$ crystal purification, production and characterization

In the first year of the LUMINEU project, during the implementation of the dedicated aboveground cryogenic test facility, the first bunch of natural $ZnMoO_4$ crystals were produced and characterised in terms of luminescent, optical, thermal and magnetic properties.

The most dangerous nuclides for $0\nu\beta\beta$ searches are ^{226}Ra and most of all ^{228}Th: they should not exceed an activity of 0.01 mBq/kg [42]; in general, the overall α activity needs to be smaller than 1 mBq/kg. Since there are no commercially available molybdenum compounds that are produced with certified radiopurity, Mo should be additionally purified. The production of LUMINEU crystals follows a dedicated protocol for a deep chemical purification technique. The good results achieved in the purification of the material are shown by atomic emission spectroscopy [78] (tab:6.3). Residual contamination can be investigated only with high sensitivity radio-purity tests which can be only done after the crystal growth in the final detector. In addition, the development of efficient

purification methods with minimal losses of molybdenum is required for the enriched material that will be used in the final phase of the project.

6.2.1 Purification of MoO_3

In the molybdenum industry two stages are used in the purification process: sublimation of the molybdenum oxide under pressurized atmosphere and subsequent leaching in aqueous solution with ammonia. The dedicated purification process developed at NIIC is an upgrade of these processes, specifically designed to reduce the dangerous contaminants in terms of crystallization, optical quality and radio-purity [79]:

- **Purification of MoO_3 by sublimation:** the classical sublimation under vacuum was revised as the concentration of tungsten still exceeds the requirement of $ZnMoO_4$ crystal growth due to the chemical affinity of W and Mo. The revised sublimation approach prescribes to add up to 1% of high pure $ZnMoO_4$ to the MoO_3 so that W replaces Mo in the precipitate at high temperature by thefollowing exchange reaction

$$ZnMoO_4 + WO_3 \rightarrow ZnWO_4 + MoO_3 \uparrow; \tag{6.1}$$

  the sublimate was then annealed in the atmosphere to obtain stoichiometric MoO_3. In addition, the sublimation removes metal oxides, which have a high vapor pressure at temperatures up to thousands of degrees.
  Losses at this stage of purification are <1.4%.

- **Purification by double recrystallization from aqueous solution:** the molybdenum oxide was dissolved in solution of ammonia at room temperature. Depending on the mixing ratio of the components, mono-molybdates and various poly-compounds and hetero-poly compounds are formed, according to the process

$$MoO_3 + 2NH_4OH \rightarrow (NH_4)_2\, MoO_4 + (NH_4)_x\, H_{(6-x)}\, [Mo_7O_24] + H_2O. \tag{6.2}$$

  The poly-molybdates solutions at pH <6 could dissolve oxides and hydroxides of many metals like ZnO, $Fe(OH)_3$, $Ni(OH)_2$, $Cu(OH)_2$, so the recrystallization of ammonium para-molybdate is not effective enough for molybdenum purification. A small amount of ZnO of 1-2 g/l is dissolved at pH >6 in the solution to initiate the precipitation. To obtain a basic solution with pH ∼8-9, ammonia is added to the solution of ammonium para-molybdate. The obtained basic solution with pH ∼8-9 provides the most favourable conditions for thorium and uranium precipitation and leads to the precipitation of contaminants in the form of hydroxides. The $ZnMoO_4$ sediment absorbs impurities from the solution. The remaining solution, after the segregation of the precipitate, was evaporated up to 70%. Ammonium oxalate was then added to the solution to bind the residual Fe impurities.
  Losses at this stage of purification are <2%.

6.2.2 $ZnMoO_4$ crystal growth

$ZnMoO_4$ crystal boules were grown in air atmosphere from the purified input powder by the low-thermal-gradient Czochralski technique in platinum crucibles of Ø40 and

TABLE 6.3: Purity level of MoO_3 after the purification process

	Concentration of impurities ppm							
	Na	Mg	Si	K	Ca	Fe	Zn	W
Starting MoO_3 powder	60	1	60	50	60	8	10	200
Recrystallization from aqueous solution	30	<1	30	20	40	6	1000	220
Sublimation and recrystallization from aqueous solution	-	<1	30	10	12	5	500	130
Double sublimation and recrystallization from aqueous solution	-	<1	-	<10	<10	<5	70	<50

Ø80 mm with an iron content that does not exceed 40 ppm. The temperature gradient was kept below 1 K/cm, the rotational speed was in the range of 5-20 rotations per minute with the crystallization rate of 0.8-1.2 mm/h. A low crystallization rate was kept during the growing of upper cone of the crystal boules. The rotational speed was decreased from the start to the end of the growth process by 1.5-2 times. The yield of the produced boules was on the level of >80%, which is an important result when enriched ^{100}Mo is used for the crystal production. Taking into account the residual material which remains in the seed and in the crucible, the losses at this stage can be estimated as ∼0.6%.

TABLE 6.4: Irrecoverable losses of purification and crystal production processes.

Stage	material loss %
Double sublimation	1.4
Recrystallization from aqueous solution	2
Crystal growth	0.6
Total	4

6.2.3 Luminescence under X-ray excitation

The luminescence of the $ZnMoO_4$ crystal was studied in the 1.4-300 K temperature range under X-ray excitation performed at the Institut d'Astrophysique Spatiale in Orsay. A $ZnMoO_4$ sample of Ø20×6 mm was irradiated through a beryllium window and an aluminium thin foil using an X-ray micro-tube (Bullet type from Moxtek; HV = 40 kV; I = 100 μA). The sample was cooled in a reflecting cavity in a cryostat and the light was transmitted by an optical fibre outside, up to an AVANTES 2048 spectrometer. The emission spectra were accumulated over 20 s; the data were taken after a long enough stabilization of the light emission level after switching the X-ray tube off.
In the resulting emission spectrum one main broad emission band is distinguishable with a maximum at 520-610 nm depending on the temperature; a near infrared emission at ∼700 nm is also observed at low temperature (fig:6.8.up). The most intensive luminescence was observed at the liquid nitrogen temperature with a maximum at a wavelength of ∼610 nm.

A rather slow phosphorescence is observed after the irradiation of the sample at the temperature of 8 K, 85 K and 295 K, which indicates the presence of shallow traps due to imperfections and defects in the crystal (fig:6.8.bottom).

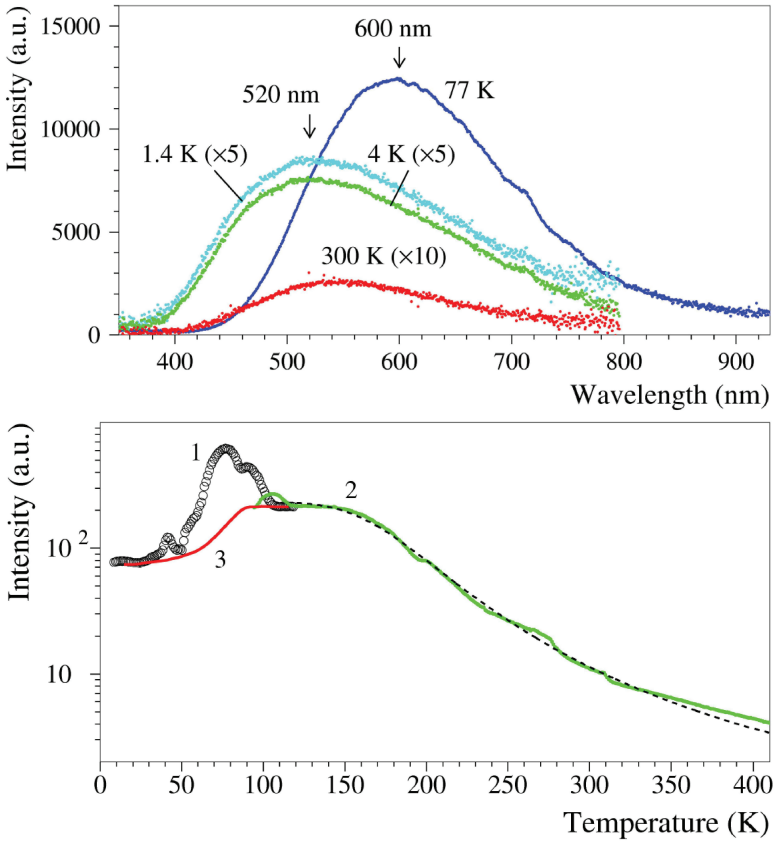

FIGURE 6.8: X-ray excitation measurement of the $ZnMoO_4$ crystal. (TOP) Emission spectra; one main emission band is observed with the emission wavelength is in 520-600 nm range depending on the temperature. (BOTTOM) Emission intensity as a function of the temperature

6.2.4 Optical absorption

Visible and near infrared absorption spectra of the $ZnMoO_4$ crystal were recorded with a Varian Cary 5000 spectrophotometer. The measurement was performed on 2 mm thick $ZnMoO_4$ crystal sample. The measured transmission coefficient T was used to calculate the absorption coefficient α using the following formula:

$$\alpha = -\frac{\mathrm{Log}(T) \cdot \ln 10}{t} \tag{6.3}$$

where t is the thickness of the sample. The result is shown in fig:6.9; the absorption coefficient decreases from 1.47 to 0.89 cm^{-1} in the wavelength region from 400 nm to 2 μm. This value does not take into account the reflections in the sample. Solving the following equation:

$$R = \left(1 + e^{-\alpha \cdot t}\right) \cdot \left(\frac{(n-1)}{(n+1)}\right)^2 \qquad \alpha = -\frac{\mathrm{Log}\,(T+R) \cdot \ln 10}{t} \tag{6.4}$$

it is possible to compute the good value of α. R is the reflection coefficient and n the refractive index. With a value of n(589 nm)=1.91 (determined with a Na lamp) a value of α=0.023 cm^{-1} is found, which corresponds to an attenuation length of 43 cm at 589 nm.

Finally, the absence of a broad absorption band of Fe^{2+}/Fe^{3+} impurities around 440 nm reflects the remarkable purity of the crystal.

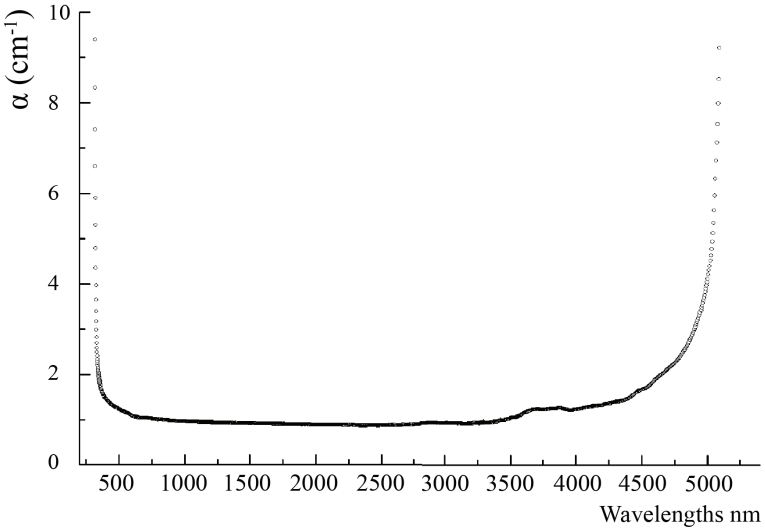

FIGURE 6.9: Absorption coefficient of the $ZnMoO_4$ crystalline sample.

6.2.5 Magnetic susceptibility

Magnetic susceptibility was measured using a Quantum Design SQUID MPMS XL magnetometer operating in the 4.2–350 K temperature range and in the 0-5 T magnetic field range. The crystal mass was 210 mg and its mass density is assumed to be 4.19 g/cm^3. The $ZnMoO_4$ proved to be weakly diamagnetic with a MKSA $\chi = -(8.0 \pm 0.2) \cdot 10^{-6}$ over the 20-320 K temperature range. Under high magnetic field applied, up to 0.2 T, there is no evidence of paramagnetic impurities, such as Fe^{2+}/Fe^{3+}.

6.2.6 Specific heat measurement

Specific heat measurements were made in a Quantum Design PPMS equipment interfaced to operate with a 2-τ pulse-step method corrected for the grease baseline. The 3×3×2 mm^3 sample was fixed on a sapphire holder with vacuum grease. The phononic contributions can be approximated with High-Temperature Series (HTS) (eq:6.5) for a temperature larger than ∼23 K.

$$C_{p,ph} \propto 1 + \sum_{i=1}^{4} B_i \left[1 + \left(2\pi \frac{T}{\theta_D} \right)^2 \right]^{-i} \tag{6.5}$$

where B_i are the so called Bernoulli numbers and θ_D the Debye temperature. From the fit of the specific heat as a function of the temperature (fig:6.10) we obtained for the first time the Debye temperature of $ZnMoO_4$ equal to θ_D ≈625 K with the following Bernoulli numbers: B_1 =1.9091, B_2 =1.86714, B_3 =-0:96009, B_4 =-0.00907.

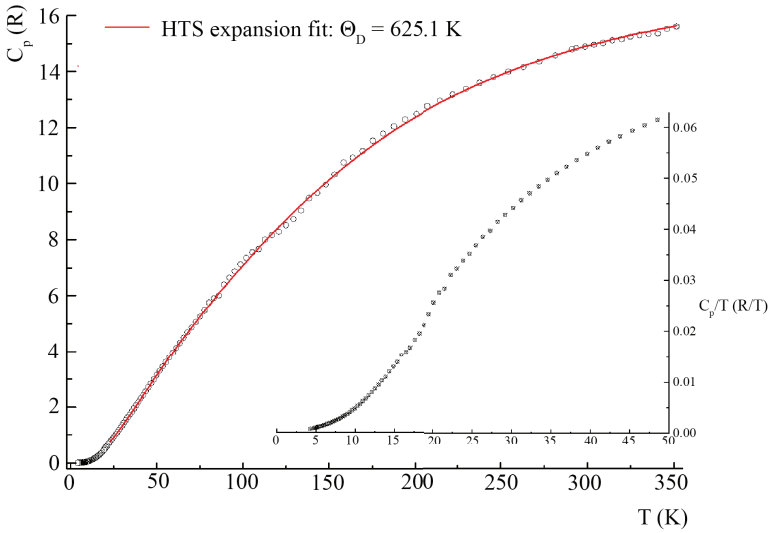

FIGURE 6.10: Specific heat measurement; the fit (red line) is performed with the HTS above 23 K. The inset shows a detail at low temperature.

6.3 Bolometers production

The construction of a prototype of a scintillating bolometer is hand made. The basic scheme is fixed but starting from crystals which have a different shape and dimension each time some specific design is needed. As a consequence, the resulting detector is unique in this R&D phase. The basic components are:

- The holder
- The thermal sensor
- Mechanical coupling pieces
- Cabling
- The heater elements
- The light detector
- The reflecting cavity

Holder preparation

The holder provides the mechanical support to hold the crystal in position inside the reflecting cavity and acts as a heat sink (during the measurement it is connected to the coldest point of the cryostat). It consists of a copper structure designed on the absorber shape and dimensions. The internal surfaces are covered by a scintillating foil (VM2000, VM2002 by 3M) or coated with silver deposited by electrolysis and polished. Once a first housing test has validated the geometry (fig:6.11), the thermal sensor and the heater can be glued on the crystal. In the meanwhile the holder can be cleaned and covered with the reflecting material. Based on the relative position of the thermal sensor and heater, contact pads for the bonding wire have to be prepared on the holder. We often use a kapton foil with gold contact pads where the wires connected to the sensor or heater at the other extremity are bonded.

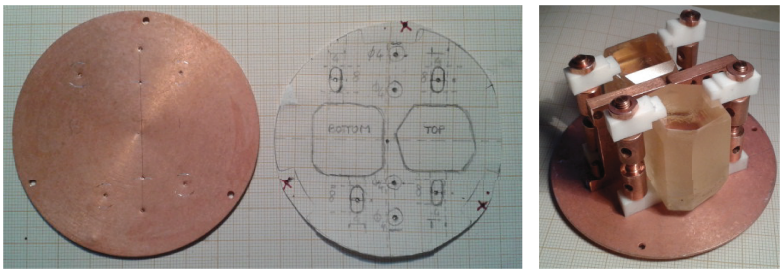

FIGURE 6.11: Bolometer holder preparation, as an example of mounting design.

Gluing procedure

The sensors are glued at the crystal using a bi-component glue known as Araldite rapid. This glue, after mixing the components, leaves 3 min times to put the sensor in position before the polymerization process takes place. It is mandatory not to wait longer than 3 minutes and not to move the sensor during the polymerization time, else the glue will never get completely polymerized and the physical parameters of the thermal coupling will be not reproducible. The glue is deposited on the crystal surface in a matrix of spots made with smoothed needles. A mask of Mylar with the desired thickness – normally in the range of 25-50 μm – is placed as a spacer and has to be removed after gluing. The sensor is then placed on the spots and pressed with a force of about several tens of grams.

If the operator is not satisfied by the result, for several minutes after the glue deposit it is still possible to remove the glued element and clean the surfaces with acetone.

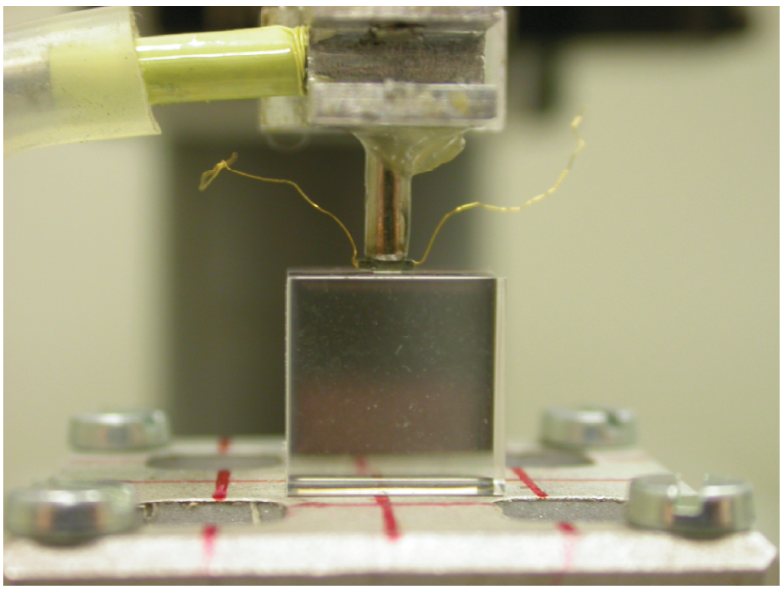

FIGURE 6.12: The picture shows the gluing procedure: the thermistor is held in position on the mobile structure above using vacuum. This tool is used for the alignment.

Assembly

When the crystal is instrumented and the holder is ready, the absorber is fixed inside the cavity by means of some PTFE elements which are soft enough to compensate the differential thermal contraction. Bonding wires are then placed to provide the electrical and thermal contacts (fig:6.13). Finally, the light detector is fixed onto the holder in correspondance of a holder side left open by purpose.

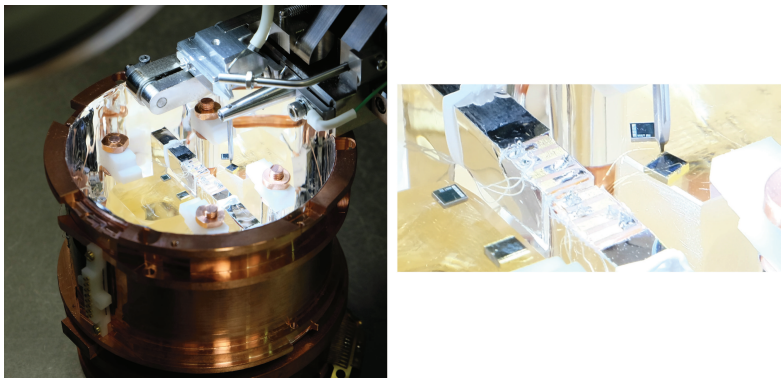

FIGURE 6.13: Details of the thermistor bonding.

6.4 Aboveground low temperature tests

The dedicated LUMINEU cryogenic test facility (described in sec:3.2.1) was ready to test the first crystals at the end of summer 2013. The goal of testing the crystals aboveground is the validation of the detector construction, as a working test before further measurements underground. A characterization of the detector prototypes in terms of sensitivity, light collection, light quenching factors for alpha particles, bolometric and spectrometric properties can be performed.

6.4.1 Macrobolometer operation

To operate a macrobolometer aboveground it is very important to choose the working point carefully. In our system it is fixed by the choice of the bias current in the NTD thermistor. The electronics of to the bias circuit sets the values up to a maximum fixed by the load resistor and the operator can choose the best bias to perform the measurement.
The best approach to select the working point is to evaluate the response of the bolometer as a funtion of the bias current; the parameters of interest for this optimization are the sensitivity, the noise and the pulse time constants. With the heater element we deliver a fixed amount of energy with the desired frequency rate; the pulse provided by the heater simulates perfectly a particle interaction. In this condition it is easy to find the optimal bias current. Two factors can be easily deduced from the generated pulses: the signal-to-noise ratio and the decay time constants. As reported in fig:6.14, the bias corresponding to the maximum sensitivity of the detector often does not match the best signal to noise ratio: a higher bias current value is usually better. In fact, the electrothermal feedback with higher bias values could provide better signal-to-noise ratio and faster signals in spite of a small decrease in sensitivity.

In concrete terms, the first step consists in finding the highest signal-to-noise ratio achievable within the available bias range. Then, if it is possible, one can try higher bias current values and find a good compromise between the decay time and the signal-to-noise ratio. In fact even a pulse twice faster can improve the pileup effect of a non negligible factor. For a series of randomly distributed events in time with an average frequency N_0, the probability P that no pileup events occur within the characteristic

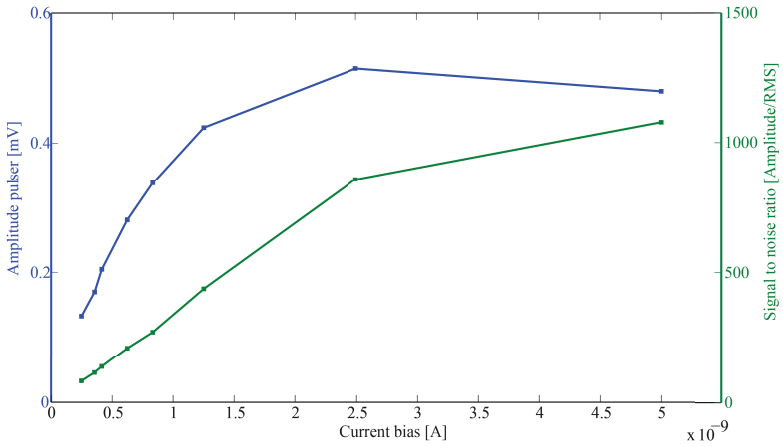

FIGURE 6.14: The sensitivity curve (blue line) and the associated signal to noise ratio (green line). The dots correspond to the available bias, the point with bias equal to 2.5 nA shows the best sensitivity and the working point at 5 nA provides the best signal-to-noise ratio. 5 nA is the correct bias option.

decay time τ_d after a given event can be expressed as

$$P(> \tau_d) = e^{-N_0 \tau_d} \tag{6.6}$$

When the sample is larger than 20-30 g, the rate of interaction could be large even with a lead shield. The pileup is a well known problem in spectrometric measurement; it can be partially treated in the offline analysis, but the final result is better if the working point is well chosen. Another important factor which can degrades the energy resolution is related to the digitalization. It is important to record the noise of the bolometer without being limited by the ADC range.
A clear example of the improvement achievable taking care of these optimization procedures is shown by the comparison of the two spectra shown in fig:6.16.TOP and fig:6.20.LEFT. These two measurements were made with similar size crystals in the same set-up. In the second case the acquisition parameters are well selected while in the first one they are not.

6.4.2 First cryogenic test on LUMINEU crystals

Two $ZnMoO_4$ samples were obtained from the first bunch of natural LUMINEU $ZnMoO_4$ crystals, the same used for the material characterization. The two crystals, with size of Ø2 cm×4 cm and Ø3.5 cm×4 cm and mass of 55 g and 160 g respectively, were mounted in a single copper holder and fixed with 4 PTFE elements each (fig:6.15). The two $ZnMoO_4$ absorbers were instrumented with a NTD Ge thermistor as a temperature sensor and a heater element to provide a response stabilization under measurement. The thermal coupling was provided by Ø25 μm gold bonding wires. A single photo-detector, consisting of a 50 mm Ge disk instrumented with a temperature sensor identical to those attached to the $ZnMoO_4$ crystals, collected the scintillation light emitted by both samples. The mixing chamber temperature was stabilized at 18 mK. Both samples and light detector performed well with an excellent signal-to-noise ratio. Fig:6.16 shows the ^{232}Th calibration spectra.

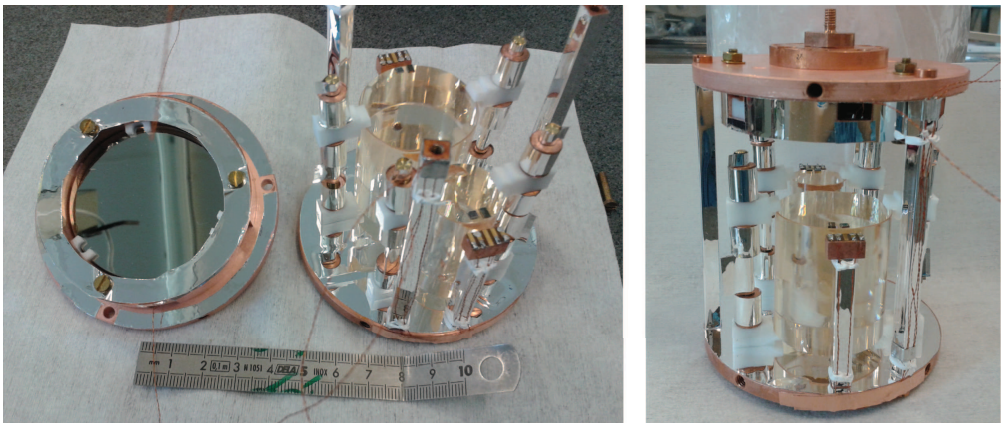

FIGURE 6.15: Detector with two absorber $ZnMoO_4$ crystal, both detector face the same light detector. The internal surface is covered by reflecting foil.

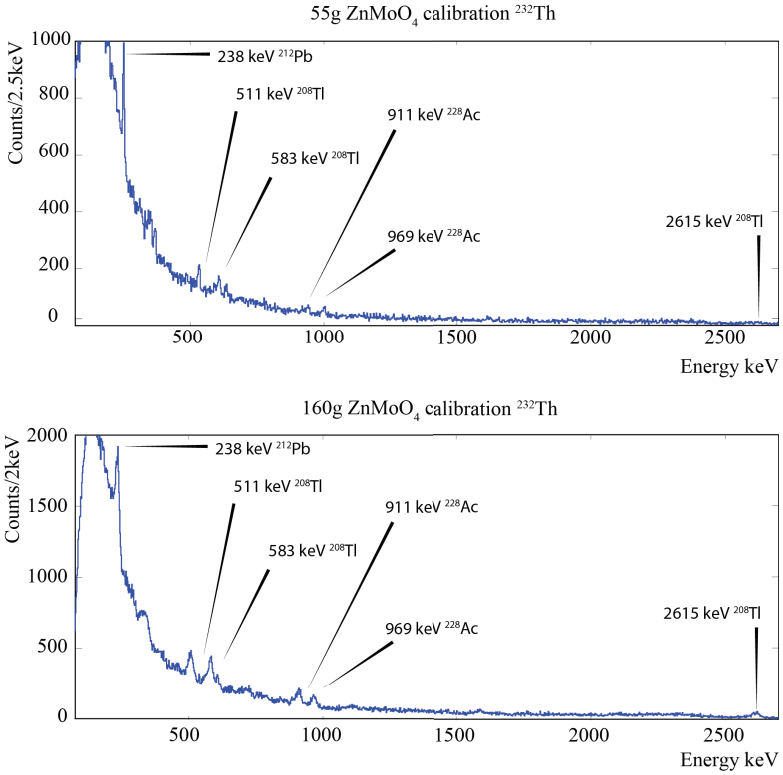

FIGURE 6.16: Calibration energy spectra. The energy resolution on the peaks is strongly deteriorated by pileup. The main lines of the ^{232}Th source are visible.

Unfortunately, aboveground operation is marginally compatible with such large crystals. In the 160 g detector the counting rate was 2.36 Hz; in practice every time window containing a full pulse contains also a second pulses at least. To lower the signal at the 30% of the amplitude τ_d=0.17 sec is needed, while lowering to its 10% of its amplitude takes τ_d=0.5sec. From eq:6.6 the fraction of events not affected by pileup is only P=0.67 and P=0.31 for the 30% and 10% respectively. Due to the pileup effect even a good detector, like this one, cannot show its best energy resolution. A data set of 4 second data accumulated with a weak ^{232}Th gamma source is shown in fig:6.17.
nevertheless, a preliminary useful characterization can be performed in terms of signal amplitude, light yield and light quenching factors for alpha particles. The results for

the two crystals are summarized in tab:6.5. The difference in thermal response is due to the intrinsic irreproducibility of the thermal coupling in this type of detectors. Fig:6.18 presents a light-heat scatter plot accumulated with the large 160 g $ZnMoO_4$ crystal with a weak ^{232}Th gamma source. With the exception of the ^{210}Po line at 5.41 MeV, no internal alpha line appeared in the energy spectrum after about two weeks of data taking. Even if it is not conclusive, this is an encouraging result in terms of radiopurity.

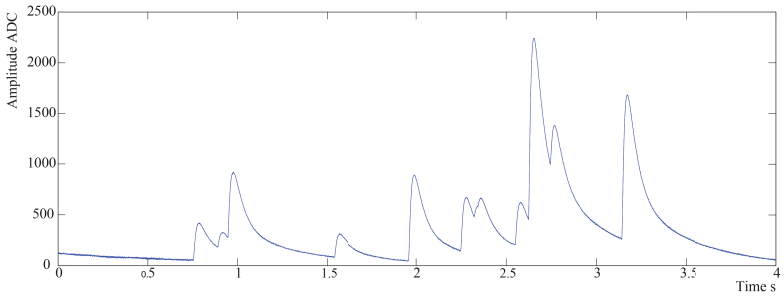

FIGURE 6.17: A dataset of four second with a 160 g $ZnMoO_4$ detector aboveground. A large pileup can be observed.

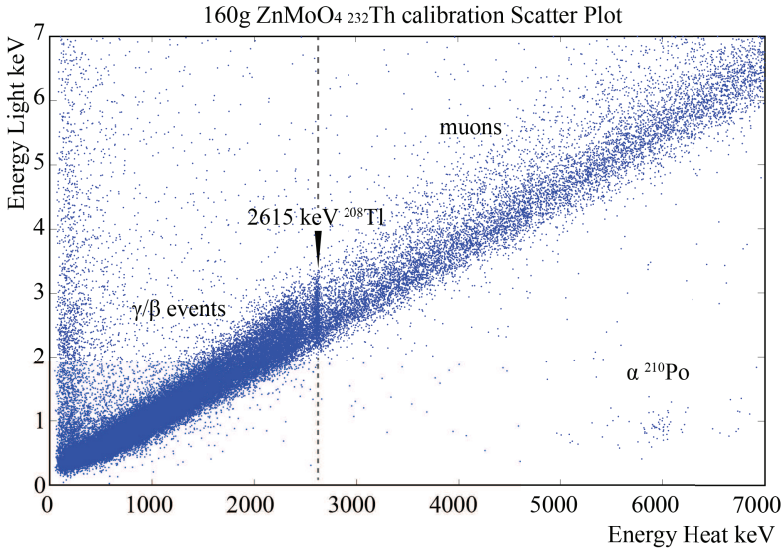

FIGURE 6.18: Scatter plot of the 160 g $ZnMoO_4$ detector during a ^{232}Th calibration. The line at 2615 keV sets the end of the natural γ radioactivity.

TABLE 6.5: Performance obtained with two $ZnMoO_4$ crystals working as scintillating bolometers.

Parameter	55 g	160 g
Temperature mK	17.5	15.4
Sensitivity μV/MeV	31	40
Baseline FWHM keV	14.6	5.5
$LY_{\gamma/\beta}$	0.98	0.96
τ_r ms	17.2	15.2
τ_d ms	130	104

6.4.3 First cryogenic test on enriched $ZnMoO_4$ crystals

A zinc molybdate crystal boule enriched in ^{100}Mo to 99.5% with a mass of 171 g was grown for the first time (fig:6.1.E). Two samples with a similar size were produced from the $Zn^{100}MoO_4$ boule – $Zn^{100}MoO_4$ top and $Zn^{100}MoO_4$ bottom referring to their position along the boule with respect to the growth axis– with masses of 59.2 g and 62.9 g, respectively. The $Zn^{100}MoO_4$ top sample, corresponds to the top part of the boule, close to its ingot, and is characterized by a less intense orange color due to the segregation of impurities in the lower part. Their irregular shape is due to the decision of keeping their mass as large as possible in order to make the bolometric tests more significant. Only two flat parallel bases are polished in order to facilitate the holding of the crystals by PTFE elements.
The two $Zn^{100}MoO_4$ crystals were used to assemble an array of scintillating bolometers (fig:6.19). Each sample was equipped with a NTD Ge thermistor for the readout of the thermal signals. It was attached at the crystal surface by using six epoxy glue spots and a 25 μm thick Mylar spacer (which was removed after the gluing procedure). In addition, as usual, each crystal was provided with a heating element glued by means of one epoxy spot. The purpose of this heater is to provide periodically a fixed amount of thermal energy in order to control and stabilize the thermal response of the $Zn^{100}MoO_4$ bolometers. The samples were fixed inside a single copper holder using PTFE elements. A light detector made of a Ø50 mm×0.25 mm high-purity Ge disk, instrumented with a NTD Ge thermistor was mounted ≈5 mm from the top face plane of the $Zn^{100}MoO_4$ crystals to collect the scintillation light. The inner surface of the copper holder was covered by a reflecting foil (VM2000, VM2002 by 3M) to improve light collection. The

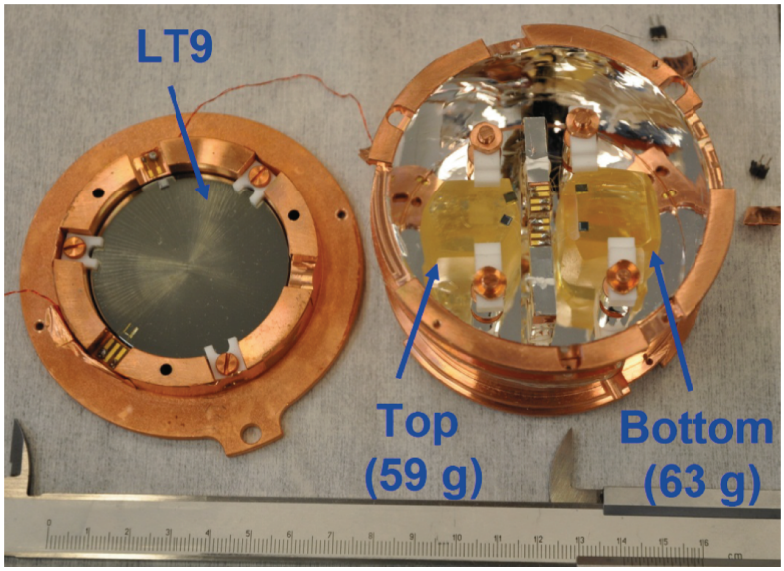

FIGURE 6.19: The detector made with the first $Zn^{100}MoO_4$ crystal ever grown. the two samples are instrumented as bolometers and face to the same LD.

test [80] was performed at three temperatures: 13.7 mK (for 18.3 h), 15 mK(for 4.8 h), and 19 mK(for 24.2 h) in the aboveground Ulisse test facility. The last working point was chosen to simulate the typical temperature conditions expected in the EDELWEISS set-up for the deep underground test in the Modane underground laboratory. Several experimental parameters were evaluated for each set of measurements: the sensitivity, the full width at half maximum baseline width (FWHMbsl), and the pulse rise (τ_r) and

decay (τ_d) times in order to extract information as regards the bolometric performance. An overview of the detector performance at 13.7 (best measurement condition) and 19 mK in terms of the mentioned parameters is provided in tab:6.6. The calibration of the LD was performed using a weak ^{55}Fe source. The energy resolution (FWHM) of the LD at the 5.9 keV line of ^{55}Fe was 0.42(2) keV at 13.7 mK and 0.57(4) keV at 19 mK. A low-activity ^{232}Th source and γ from natural radioactivity mainly due to ^{214}Bi of the ^{222}Rn chain was used to determine the energy scale of the $Zn^{100}MoO_4$ bolometers.

TABLE 6.6: Performance obtained with two $Zn^{100}MoO_4$ crystals working as scintillating bolometers.

	13 mK		19 mK	
Parameter	Top	Bottom	Top	Bottom
Sensitivity μV/MeV	86.8	95.8	65.0	84.2
Baseline FWHM	1.4	1.8	1.8	2.4
609keV FWHM	5.0±0.5	10±1		
2516keV FWHM	11±3	15±3		
$LY_{\gamma/\beta}$	1.01±0.11	0.93±0.11	1.02±0.11	0.99±0.12
τ_r	9.0	5.5	8.9	5.8
τ_d	46.3	26.2	48.4	30.7

The energy spectrum accumulated by the $Zn^{100}MoO_4$ top detector operated at 13.7 mK is shown in fig:6.20. The energy resolution for the detectors at 2614.5 keV of ^{208}Tl was FWHM = 11(3) keV for the $Zn^{100}MoO_4$-top, and FWHM = 15(3) keV for the Z $^{100}MoO_4$-bottom, in the measurements at 13.7 mK. As one can see from fig:6.20, the 2614.5 keV peaks have quite a low statistics due to the small mass of the crystals and the short duration of the measurements. Therefore, it is reasonable to estimate the resolution of the detectors for the more intensive γ lines presented in the spectra below 1 MeV. For example, the FWHM at the 609.3 keV peak of ^{214}Bi was 5.0(5) and 10(1) keV for the $Zn^{100}MoO_4$ top and bottom, respectively. Experience with large-mass slow bolometric detectors, as argued before, shows that the energy resolution on the γ lines is significantly affected by the pulse pileup.

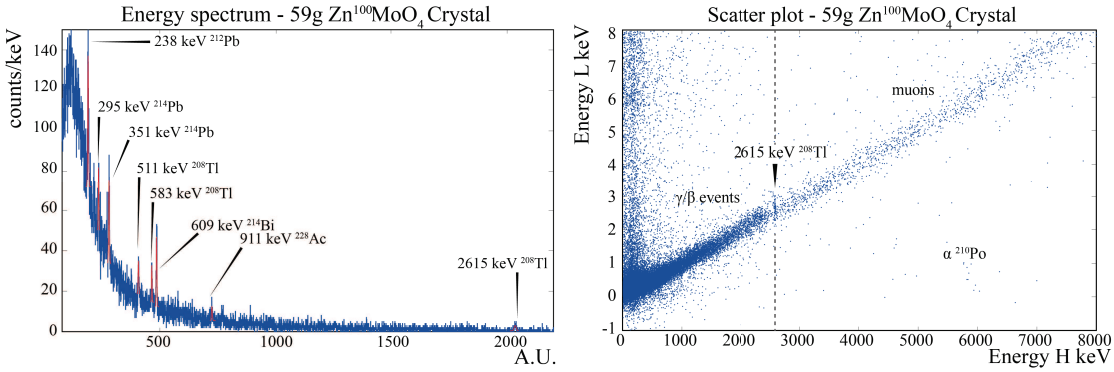

FIGURE 6.20: (LEFT) ^{232}Th calibration spectrum. (RIGHT) Scatter plot. The figures are obtained with the data acquired with the $Zn^{100}MoO_4$ top crystal.

The Q-plots reporting the light-to-heat signal amplitude ratio as a function of the heat signal amplitude of the data accumulated for 18.3 h with the enriched $Zn^{100}MoO_4$ crystals are presented in fig:6.21. The data allow us to estimate the light yield related to γ/β particles whit a fit in the 600-2700 keV interval. They are summarised in tab:6.6. In spite of the short duration of the measurements and the aboveground conditions, the

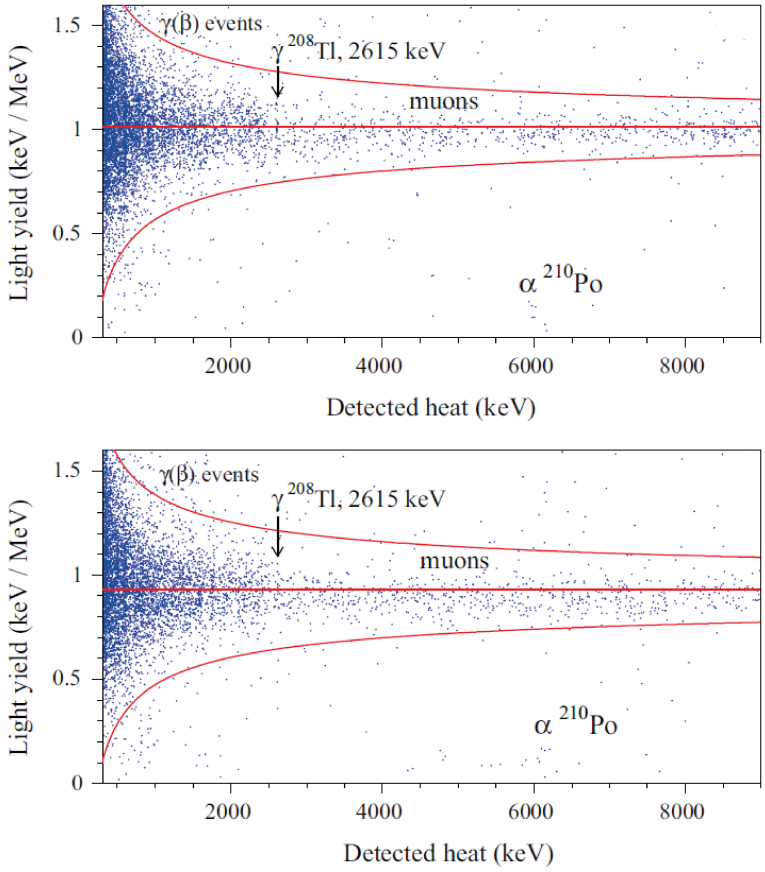

FIGURE 6.21: Q-plots. (TOP) $Zn^{100}MoO_4$-top crystal. (BOTTOM) $Zn^{100}MoO_4$-bottom crystal.

data presented in fig:6.21 show an encouraging internal radio-purity level of these crystals: the absence of significant α peaks indicates that the contamination of the harmful ^{228}Th and ^{214}Bi nuclei does not exceed the level of a few mBq/kg. Only a weak event accumulation probably related to ^{210}Po is detectable. Considering a 200 keV interval around the α events cluster the analysis of the data accumulated at 13.7 and 19 mK together gives an activity of ^{210}Po in the crystals at the level of 1.1(3) for the top and 1.2(3) mBq/kg for the bottom.
The radiopurity analysis of the $Zn^{100}MoO_4$ crystals was performed also in measurements in underground conditions (sec:6.5.2). The bottom detector demonstrated to have worse worse performance probably because the quality of the lower part of the crystal boule is worse with respect to the upper part, as highlighted by the optical quality too.

6.4.4 Bolometric effects on a tungsten doped $ZnMoO_4$ crystal

We made comparative studies of the $ZnMoO_4$ crystal scintillators produced from the melt with excess of molybdenum and doped with tungsten. The properties of the crystals important for the application in a cryogenic $0\nu\beta\beta$ experiment were measured [81].
Two cylindrical crystalline samples, one of them based on pure stoichiometric $ZnMoO_4$ and the other one on $ZnMoO_4$ doped with tungsten at the level of 0.5 % – with a size of ⌀20 mm×40 mm and mass of approximately ∼50 g each – were used to assemble a scintillating bolometer array. The goal was to use this setup to test if the bolometric

properties and the light emission of the doped compound are preserved in comparison with the pure one. This test is particularly important since the addition of W seems to facilitate the growth procedure.
The assembled scintillating bolometers are shown in fig:6.22. Each crystal is fixed at the copper holder with the help of four PTFE elements. The two samples are placed symmetrically with respect to the holder and to the light detector in order to avoid systematic effects in the evaluation of the collected light. The internal surface of the copper holder is covered by a reflecting foil (VM2000, VM2002 by 3M) to improve light collection. Both crystals are equipped with a identically neutron transmutation doped Ge thermistor used for the readout of the thermal signals delivered by the impinging particles. In addition, a heating element is glued on each crystal for stabilization. A light detector – made of a ⌀50 mm×0.25 mm high-purity Ge disk and instrumented with a NTD Ge thermistor and a heating element as well – is mounted ∼5 mm above the top surfaces of the crystals.

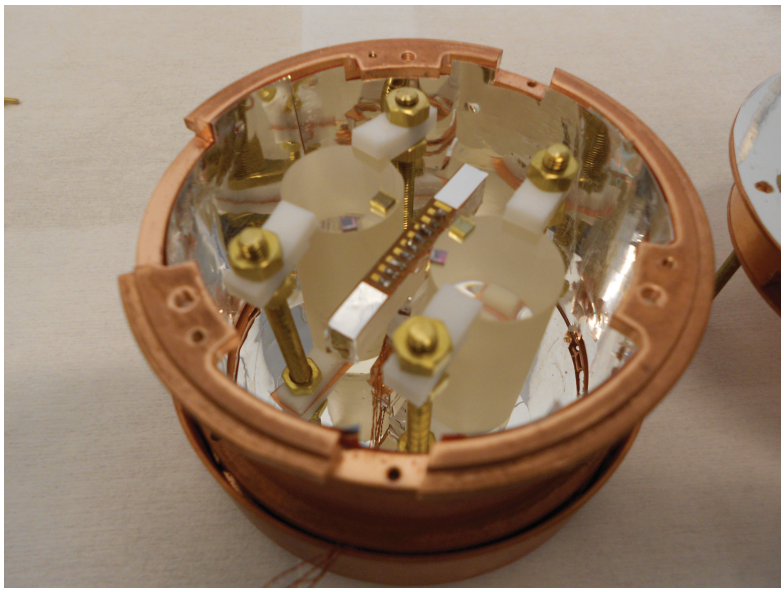

FIGURE 6.22: Picture of the detector. The two crystals are placed symmetrically with respect the holder structure in order to avoid systematics in the light collection. One $ZnMoO_4$ crystal is doped with W, the other is not.

The scintillating bolometer array was tested at low temperatures using a pulse-tube cryostat housing a high-power dilution refrigerator installed at CSNSM (sec:3.2.1). The test was performed at a temperature of 23 mK.
The working resistance of the NTD thermistors was quite different for the two $ZnMoO_4$ bolometers: in particular the one coupled to the $ZnMoO_4$(W) doped crystal showed a smaller value. This kind of behavior is often observed in nominally identical detectors. It is due to different levels of parasitic powers induced by vibrations, which determine differences in base temperatures. Thus we were obliged to set different working points. In this condition, the sensitivities of the two bolometers were quite different (the colder bolometer was of course more sensitive), but in spite of that both detectors worked well in terms of spectrometric properties. They were calibrated by means of a ^{232}Th source and of the γ peaks induced by the environmental radioactivity. The light detector was calibrated with a X-ray line at 5.9 keV provided by a ^{55}Fe source located on the opposite side of the Ge disk.

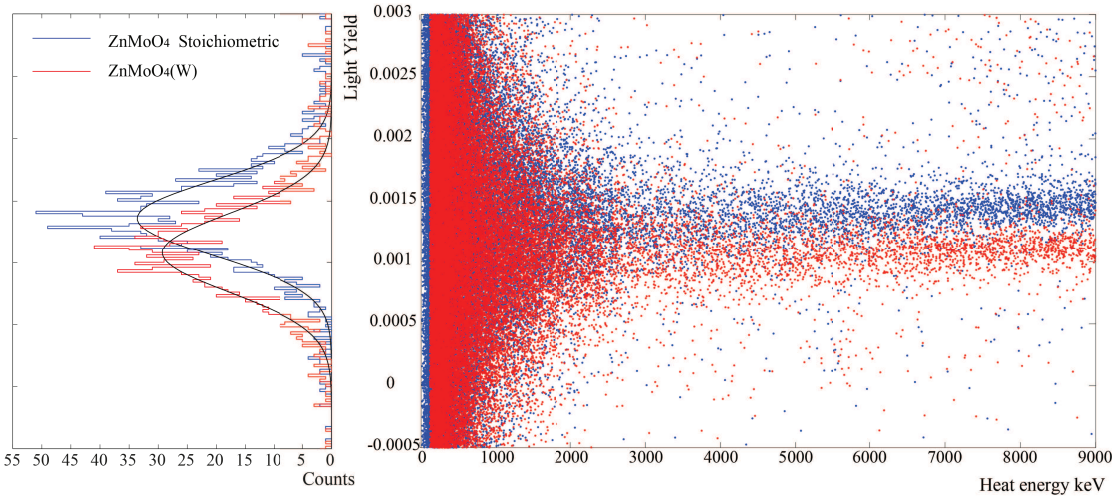

FIGURE 6.23: Q-plot comparison. The red points correspond to the W doped $ZnMoO_4$ crystal, the blue points correspond to the stoichiometric $ZnMoO_4$ crystal. The light yield is in the 3-4 MeV range is projected on the left picture.

Once the response of both the detectors was calibrated, we analysed the events occurred in coincidence between the $ZnMoO_4$ or the $ZnMoO_4$(W) bolometer and the LD. Two main classes of coincident events can be distinguished: those induced by the the cosmic rays (mainly muons) crossing both the $ZnMoO_4$ crystal and the LD, and the scintillation events, which are selected in order to evaluate the light yield (LY). A Q-plot of these signals is shown in fig:6.23. The two bands, populated by β/γ and cosmic muons, show different slopes corresponding to different LYs. These parameters are evaluated in the high energy region, considering the 2-3 MeV interval for the calibrated heat signals (fig:6.23), close to the characteristic energy of $0\nu\beta\beta$ of ^{100}Mo. The LY is 1.34 ± 0.01 keV/MeV for $ZnMoO_4$ and 1.08 ± 0.01 keV/MeV for $ZnMoO_4$(W). The difference in the collected light for the two bolometers is very small for an equal deposited energy in the scintillators. Assuming a symmetric setup for the light collection, this could be due to the difference of the scintillation efficiency and optical transmittance of the samples. However, in the framework of the LUMINEU experiment, the LY of the doped compound is by far large enough for a complete separation of β/γ and α events.
This measurement allowed us to include safely a W doping at the $\sim$0.5% level in the growth protocol of $ZnMoO_4$ crystals.

6.5 Underground low temperature measurement

After this preliminary results, it was important to perform underground measurement to investigate the presence of radionuclides which contribute to the background. In addition to this test, the detectors measure the environmental radioactivity in the set-up and give important information about its bolometric operation. these tests are in practice a fasibility tests of the final experiment; all the tools developed in this phase should be compatible or extendible to the final approach.

6.5.1 Advanced $ZnMoO_4$ scintillating bolometers

A colourless large mass $ZnMoO_4$ crystal boule was grown in air atmosphere by directional solidification along the [001] crystalline axis with the purification and growing technique described in sec:6.2.1. The boule was melted and then crystallized again. From this crystal two large volume scintillation elements with a size of Ø50 mm×40 mm (fig:6.1.F) with masses of 336 g and 334 g were cut and used to build two scintillating bolometers to be measured [82] in the EDELWEISS set-up at the LSM laboratory (sec:3.2.5). The sizes of the scintillation elements are already compatible with the LUMINEU requirements and in general with a large-scale $0\nu\beta\beta$ decay experiment.
The two large natural zinc molybdate crystals were placed in a individual cylindrical copper holder with three L-shapes PTFE feet on the bottom and three S-shaped PTFE pushing the crystal downwards and tightened on the copper holder. The internal surface of the copper holder was covered by a reflecting foil (VM2000, VM2002 by 3M) to improve light collection. Each crystal is equipped with two identical neutron transmutation doped Ge thermistors for the readout of the thermal signals. As usual, a heating element is glued in order to control and stabilize the thermal response. The upper side of the holder is covered with the light detector equipped with a NTD thermistor too. No calibration sources were placed inside the holder to avoid contamination of the set-up.
The measurement was performed at the temperature of 18 mK and 19 mK; the NTDs used for these detectors show a high resistivity of the order of 10-100 MΩ which is not optimised for the standard EDELWEISS acquisition chain, based on an AC polarization bias (sec:4.1.2). The issue found in the EDELWEISS setup is the fact that this setup is not optimised in terms of vibrations and bolometers are very sensitive to microphonics noise, especially the optical ones.

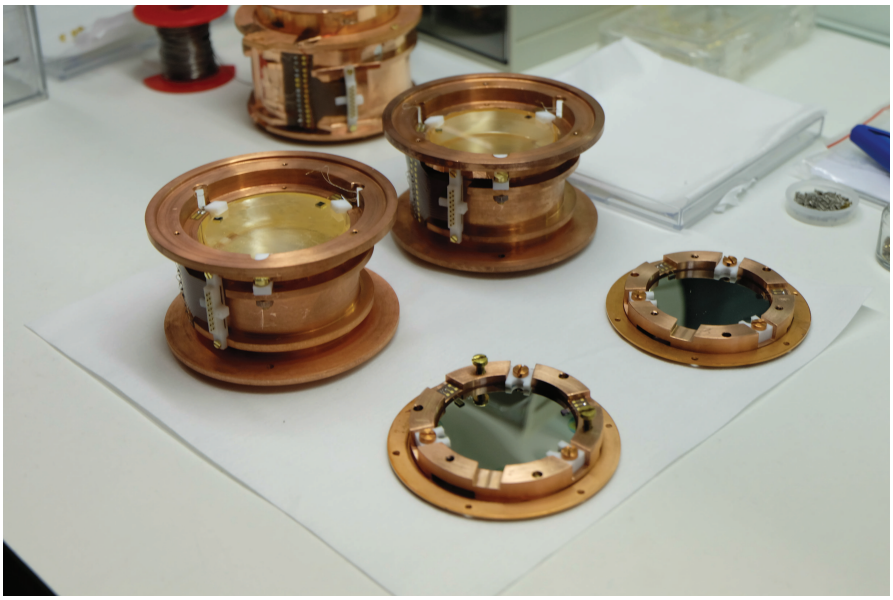

FIGURE 6.24: $ZnMoO_4$ detectors with their LDs on the side.

The overall accumulated data correspond to a 3075 h exposure. The energy scale of the heat channels of the $ZnMoO_4$ bolometers was determined mainly with a ^{133}Ba reference calibration source, used periodically in the EDELWEISS calibration procedure. One calibration measurement for each detector was performed with a ^{232}Th source made of thoriated tungsten wires containing 1% of thorium in weight. The energy resolution

on the 356 keV ^{133}Ba line was in the range of 3-5 keV for the best detector (fig:6.25) depending on operation settings; the other detector, which is more affected by microphonics noise, shows an energy resolution in the 5-20 keV range. The ^{232}Th calibration was performed for 37 h and is useful to evaluate the energy resolution on the γ peak of ^{208}Tl at 2615 keV, the closest peak to the energy of the $0\nu\beta\beta$. The spectrum collected by the best bolometer, reported in fig:6.26, shows a FWHM resolution of 5.0(4) keV at 969 keV of ^{228}Ac γ line and 10(1) keV at the ^{208}Tl line. For the second detector the FWHM energy resolution are evaluated to be 9(1) keV and 26(3) keV respectively [83].

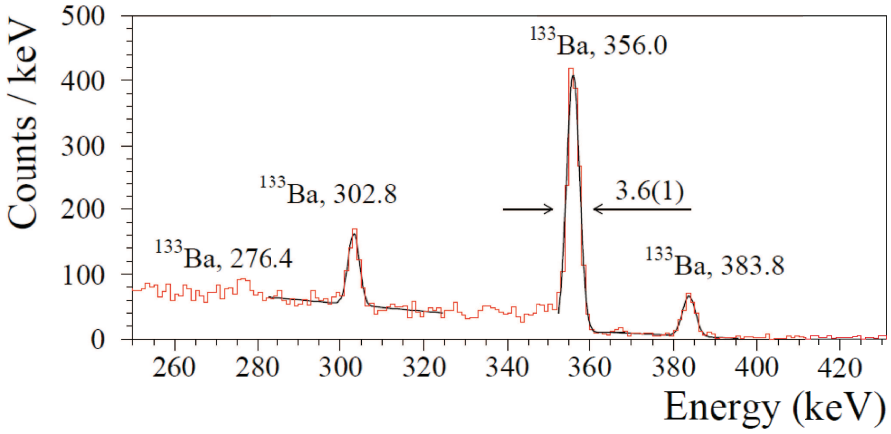

FIGURE 6.25: 334 g $ZnMoO_4$ crystal ^{133}Ba calibration spectrum.

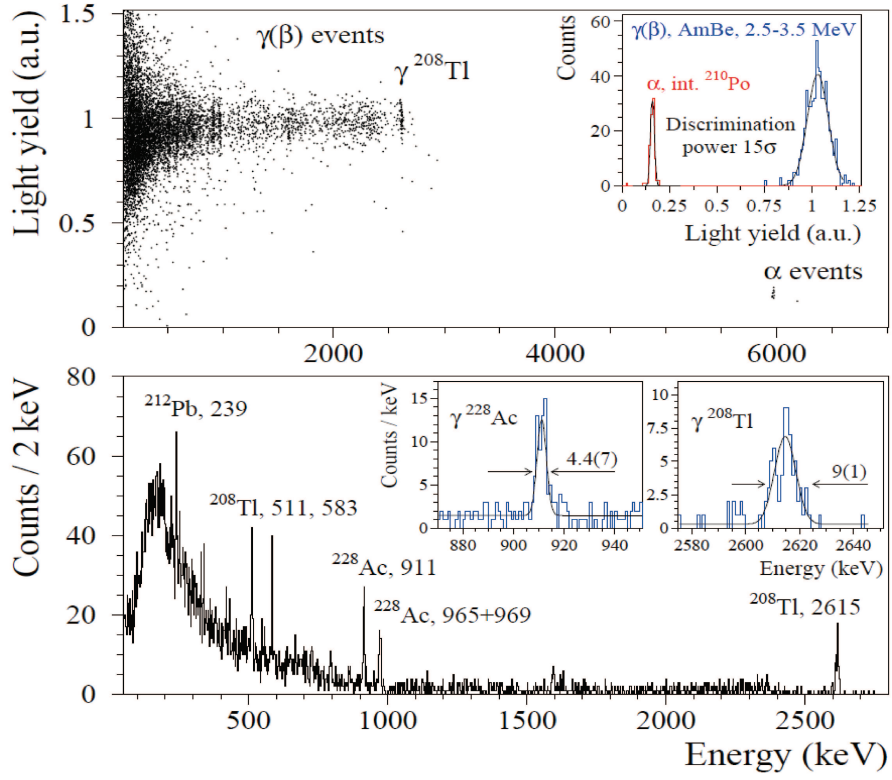

FIGURE 6.26: 334 g $ZnMoO_4$ crystal ^{232}Th calibration. (TOP) Q-plot. (BOTTOM) Energy spectrum.

with the Th calibration we can also define the discrimination power using the γ's provided by the source in the 2.5-3.5 MeV range and the α particles of the internal ^{210}Po contamination. The result is shown in the insert of fig:6.26 and the discrimination power is evaluated at the level of 15 σ according to:

$$DP(E) = \frac{\left|\mu_\alpha(E) - \mu_{\gamma/\beta}(E)\right|}{\sqrt{\sigma^2_\alpha(E) + \sigma^2_{\gamma/\beta}(E)}} \tag{6.7}$$

An evaluation of the internal radio-purity was performed from the underground measurement described above. The EDELWEISS set-up has not been optimized yet for LUMINEU-like detectors, especially the control of the vibration induced noise. As a result, the light channel of the advanced $ZnMoO_4$-based bolometer was affected in several data sets by a severe microphonic noise which deteriorated the performance enough. Therefore, in spite of the excellent α/γ discrimination achieved with the $ZnMoO_4$ bolometers in selected runs, this technique was not applied over the full data set. Taking into account that the dominant part of the γ/β background is located below 2.6 MeV, we used the data of the heat channels above 3 MeV for radio-purity analysis. In fact, this energy region is populated mainly by the α's emitted by the radionuclides of the U/Th chains. The heavy shield and the underground condition guarantee a negligible background of neutrons and muons. The spectra measured by both the $ZnMoO_4$ bolometers – normalized on the live time of the measurements and the mass of the crystals – are shown in fig:6.27. A few α peaks caused by trace internal radioactivity are visible. The major contribution is due to ^{210}Po internal and external contaminations. As already discussed this nuclide is not dangerous and furthermore was welcome at that level for the thermal response stabilization. In fact the electronics to drive the heater was available only in the last part of the run.
It is evident from the comparison of fig:6.27 and fig:6.7 that the advanced crystal has significantly higher purity with respect to the precursor. Obviously, ^{210}Pb and ^{210}Po inclusion leads to a broken equilibrium in the ^{238}U chain, which is observed in the spectra. It is worth noting that broken equilibrium in the U/Th radioactive chains occurs in general in scintillating crystals, because some radionuclides can be separated during crystal production due to different chemical properties and this is the case for the tested $ZnMoO_4$ crystals.
The estimated contamination levels are reported in tab:6.7; we want to stress that they show a remarkable radiopurity especially in ^{228}Th, which was under the detectable level and so much better than the final requirements for the LUMINEU project.

6.5.2 Enriched $Zn^{100}MoO_4$ scintillating bolometers at Modane

The $Zn^{100}MoO_4$ bolometers array tested abovebround (sec:6.4.3) were moved underground in the EDELWEISS set-up at the LSM laboratory (sec:3.2.5).
In contrast with the good performance obtained in the aboveground tests, the detectors were strongly affected by microphonic noise during the underground measurement; the maintenance to fix this problem was unfortunately not compatible with the EDELWEISS III schedule. In many cases the baseline fluctuates at the level of hundred keV within the pulse time constants. This unfavorable condition led us to reject approximately half of the data, resulting in a measurement life time of about 1650 h for each sample, bottom and top.
The scatter plots acquired during the selected background measurement are reported

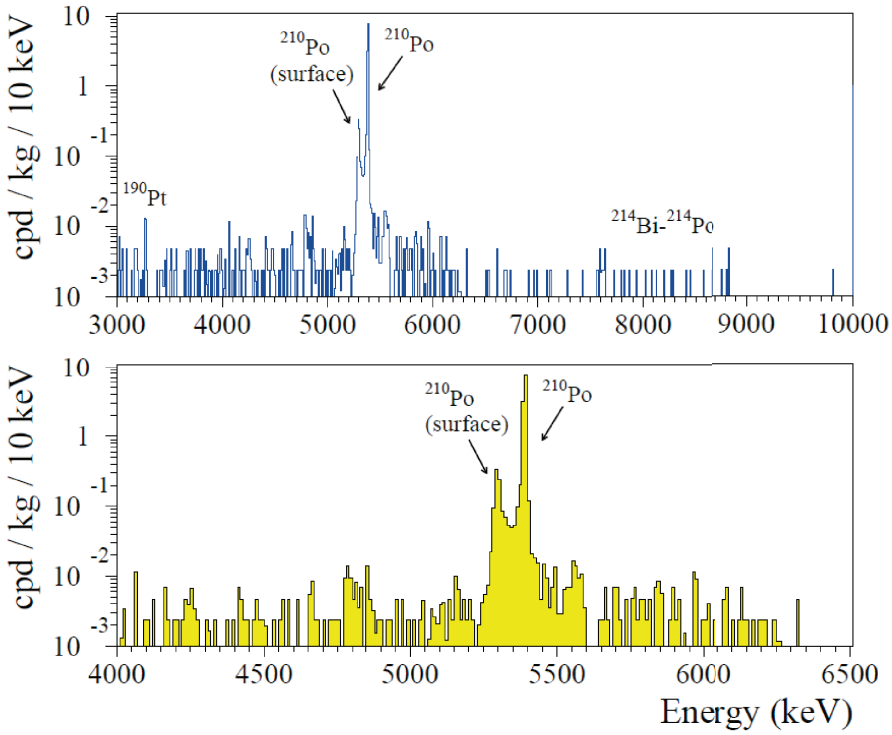

FIGURE 6.27: α spectrum of the 334 g $ZnMoO_4$ detector internal contamination. The bottom figure is a detail of the ^{210}Po energy range.

TABLE 6.7: Summary of the internal activity measured underground for the 334 g $ZnMoO_4$ detector, 336 g $ZnMoO_4$ detector and LUMINEU precursor detector. The contamination levels obtained from the crystals adopting the improved purification process are smaller.

			Activity [mBq/kg]		
			LUMINEU crystal		Precursor crystal
Nuclide	Q_α-value [keV]	Half life	334 g 3075 h	336 g 1540 h	313 g 803 h
^{232}Th	4081.6±1.4	1.405×10^{10} yrs	⩽0.002	⩽0.007	⩽0.006
^{228}Th	5520.08±0.22	1.9116 yrs	⩽0.004	⩽0.026	0.012±0.004
^{238}U	4269.7±2.9	4.468×10^{9} yrs	⩽0.002	⩽0.026	0.008±0.003
^{234}U	4857.7±0.7	2.455×10^{5} yrs	⩽0.002	⩽0.020	⩽0.008
^{230}Th	4769.8±1.5	7.538×10^{4} yrs	⩽0.002	⩽0.028	⩽0.008
^{226}Ra	4870.62±0.25	1.6×10^{3} yrs	⩽0.004	⩽0.026	0.022±0.005
^{210}Po	5407.45±0.07	138.376 d	1.3±0.2	0.58±0.02	0.7±0.3
^{235}U	4678.2±0.7	7.038×10^{8} yrs	⩽0.003	⩽0.019	⩽0.007
^{190}Pt	3252±6	6.5×10^{11} yrs	⩽0.004	0.004±0.001	⩽0.007

in fig:6.28. In spite of the bad performance of the detector a separation of γ/β and α particles is evident, and a new population of events is recognizable: a fraction of α particles, mainly belonging to ^{210}Po produces zero light signal and has a larger thermal signal. A part of these events are mixed and produce less light and a larger heat giving a continuum from the alpha population to this zero light events. This peculiarity is also observed in the big $Zn^{100}MoO_4$ scintillating bolometers tested at LNGS and described below (sec:6.5.3).

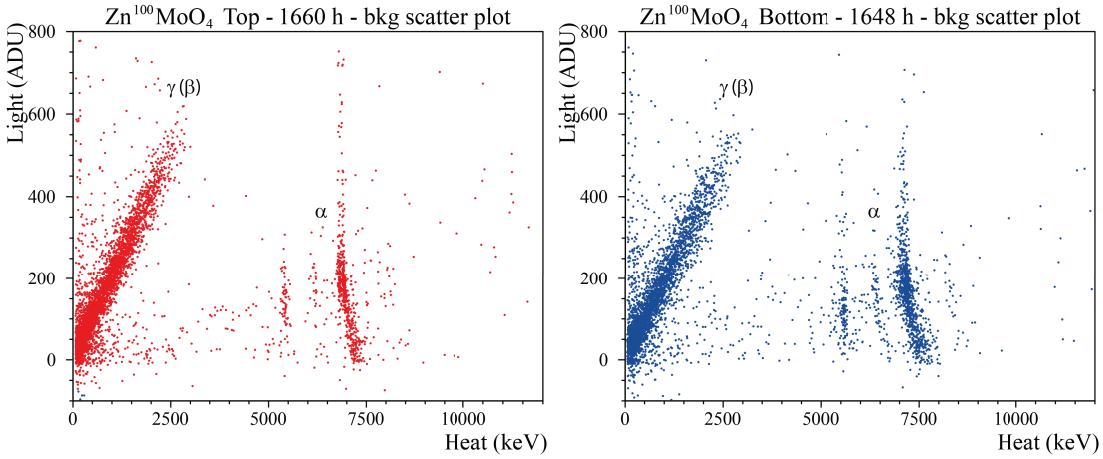

(A) (B)

FIGURE 6.28: (A) Scatter plot for the $Zn^{100}MoO_4$ top enriched crystal. (B) Scatter plot for the $Zn^{100}MoO_4$ bottom enriched crystal.

The detectors are calibrated using the standard EDELWEISS proceedure with the ^{133}Ba source; the calibration spectra are shown in fig:6.29a and fig:6.29b. In this measurement conditions the energy resolution is quite modest as expected. The parameters that should be taken into account to characterize these detectors performance are the ones measured aboveground (tab:6.6).

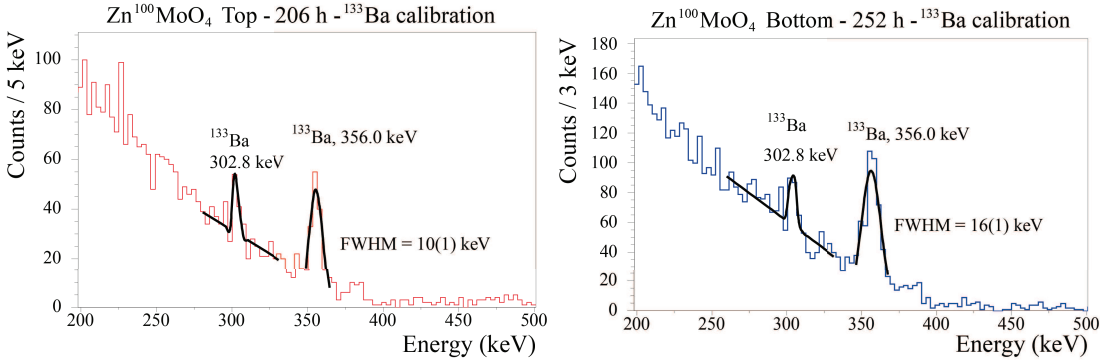

(A) (B)

FIGURE 6.29: (A) ^{133}Ba calibration $Zn^{100}MoO_4$ Top. (B) ^{133}Ba calibration $Zn^{100}MoO_4$ bottom.

An evaluation of the contaminant nuclei is performed using the energy spectra above 3 MeV, in underground condition, with the small detector; the probability of high energy γ contributing to this high energy range is small and the α's contamination level is large enough to consider it negligible. The α energy spectrum is shown in fig:6.30a for $Zn^{100}MoO_4$ top and in fig:6.30b for $Zn^{100}MoO_4$ bottom. In tab:6.8 a summary of the evaluated activity is reported.

The poor energy resolution on the α peaks obliged us to consider a wide energy range to estimate the radioactive contamination so that the found limits are less stringent than the natural crystal estimation. Anyway, we considered this first attempt to grow $ZnMoO_4$

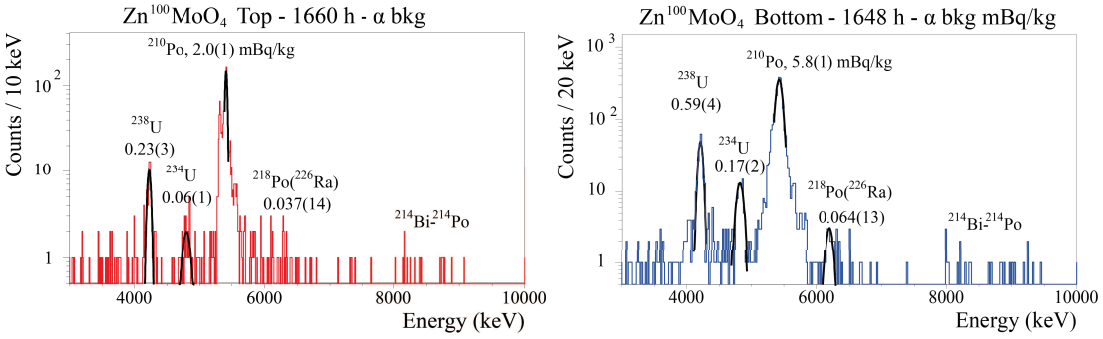

(A) (B)

FIGURE 6.30: (A) Alpha background in the $Zn^{100}MoO_4$ top. (B) Alpha background in the $Zn^{100}MoO_4$ bottom.

TABLE 6.8: Radio-purity measured for the $Zn^{100}MoO_4$ top and bottom crystals.

detector	Activity [mBq/kg]							
	^{232}Th	^{228}Th	^{238}U	^{234}U	^{230}Th	^{226}Ra	^{210}Po	^{235}U
$Zn^{100}MoO_4$ top	$\leqslant$0.04	$\leqslant$0.26	0.23±0.03	0.06±0.01	$\leqslant$0.12	0.04±0.01	2.0±0.1	$\leqslant$0.10
$Zn^{100}MoO_4$ bottom	$\leqslant$0.06	$\leqslant$0.29	0.59±0.04	0.17±0.02	$\leqslant$0.06	0.06±0.01	5.8±0.1	$\leqslant$0.05

with enriched material a success. Taking into account that the enriched $^{100}MoO_3$ powder has different source the higher contamination can be addressed to a higher contamination of the starting materials, to improve it we can use the segregation of the impurities which occurs during the crystallization process. In fact, the lower part of the boule shows higher contamination level and worse crystal quality. In many cases, after the a first crystallization, the boule is melt again and recrystallize for purification purpose.

6.5.3 Enriched $Zn^{100}MoO_4$ scintillating bolometers at LNGS

Finally, one boule made of $Zn^{100}MoO_4$ with a mass of ∼1.4 kg was grown (fig:6.1.H), from which two big crystals of about ∼380 g each were cut and instrumented as bolometers for a measurement in the Hall-C cryostat at the LNGS underground laboratories (sec:3.2.4). The material purification and crystallization follow the procedure described in sec:6.2. In analogy with the previous samples we will call these two crystals $Zn^{100}MoO_4$ top and bottom with respect to their position along the growth axis. The crystals have a hexagonal shape with a mass of 379 g and 382 g for top and bottom respectively.
The two samples were instrumented with NTD Ge thermistors for the readout and a heater element for stabilization. Each detector had its own LD made by an utrapure Ge disk adopting the easy-assembly configuration. Near the detector, a smeared alpha source was placed to evaluate the DP in the ROI energy range.
Two calibration runs with ^{232}Th and ^{40}K sources and a long background measurement, of about 600 h, were performed. The cumulative background scatter plots are shown in fig:6.31; the light detector associated with the bottom crystal worked better but both scintillating bolometers had remarkable DPs, which are 7.8(4) and 11.4(5) for top and bottom respectively.

The α population without light emission is visible in fig:6.31 for both detectors. The external α's do not show such a behavior so they must be the α's related with the impurities. We are not able to give a satisfactory explanation to this phenomenon: in

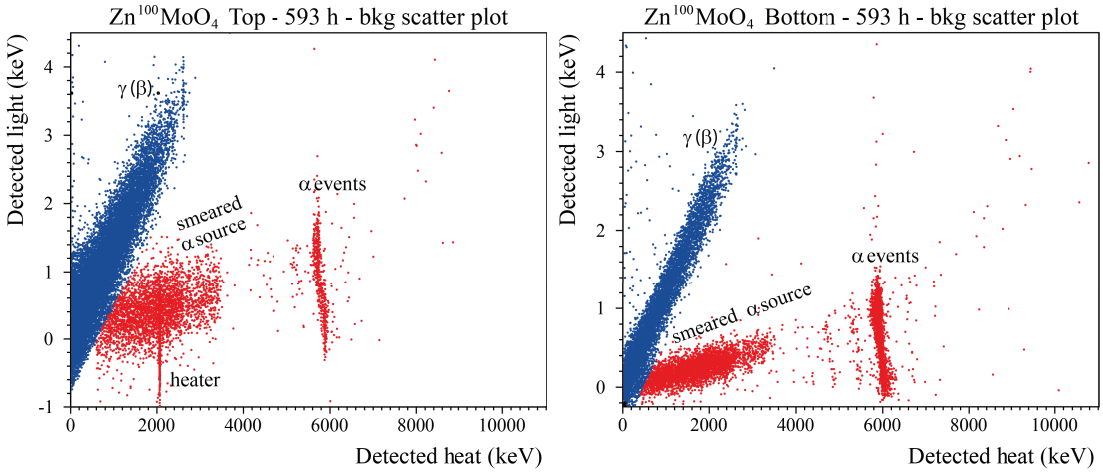

(A) (B)

FIGURE 6.31: (A) Scatter plot for the $Zn^{100}MoO_4$ top enriched detector. (B) Scatter plot for the $Zn^{100}MoO_4$ bottom enriched detector.

our interpretation there are regions in the crystals in which the α light yield is strongly quenched. Since this phenomenon is not observed in β/γ, we suspect that these regions are small, with a size of the typical α particle range which is much smaller than a β particle range for the β energies typical of natural radioactivity (fraction of mm or few mms). This behaviour may be related to the larger impurities concentration in enriched crystals.

However, this phenomenon is not worrying because it is observed only with alpha particles and does not affect the working principle of the detector. The favourable measurement condition and the remarkable quality of the crystals are reflected in the good energy resolution measured in the calibration run (fig:6.32 and fig:6.33). The main characteristics of the detector are reported in tab:6.10.

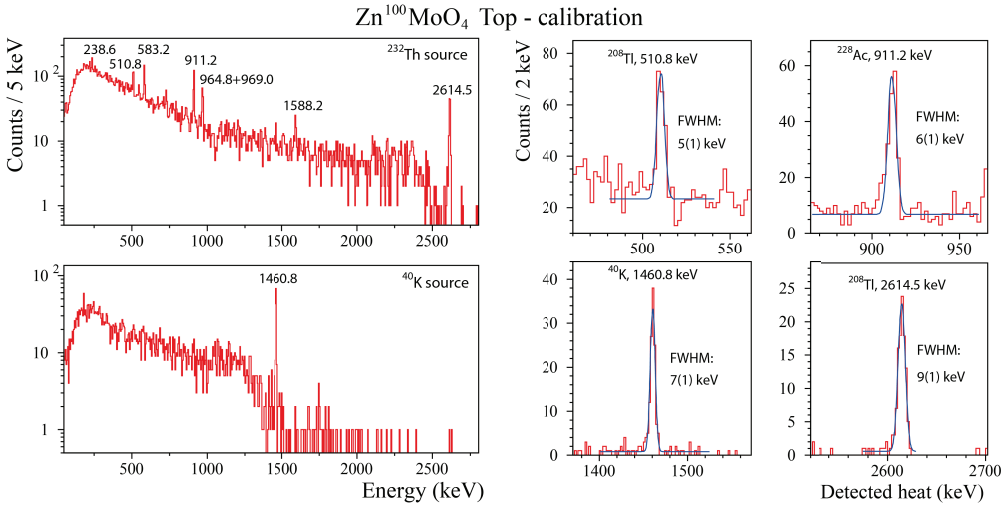

FIGURE 6.32: (TOP) ^{232}Th calibration for $Zn^{100}MoO_4$ top. (BOTTOM) ^{40}K calibration for $Zn^{100}MoO_4$ top.

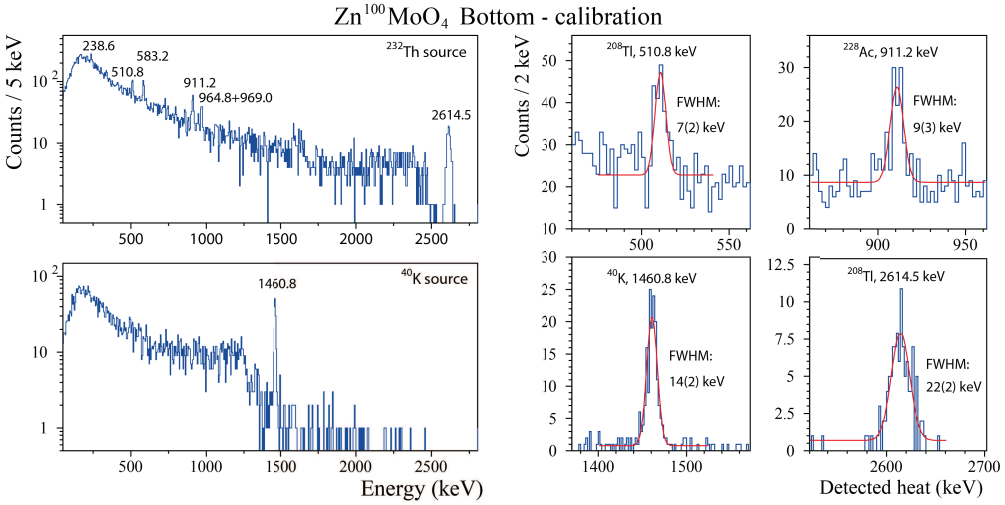

FIGURE 6.33: (TOP) ^{232}Th calibration for $Zn^{100}MoO_4$ bottom. (BOTTOM) ^{40}K calibration for $Zn^{100}MoO_4$ bottom.

Performing a simple cut on the LY we were able to isolate the α particles obtaining the α spectra (fig:6.34) used to evaluate the contamination in the crystals. The activity of the contaminants is reported in tab:6.9.

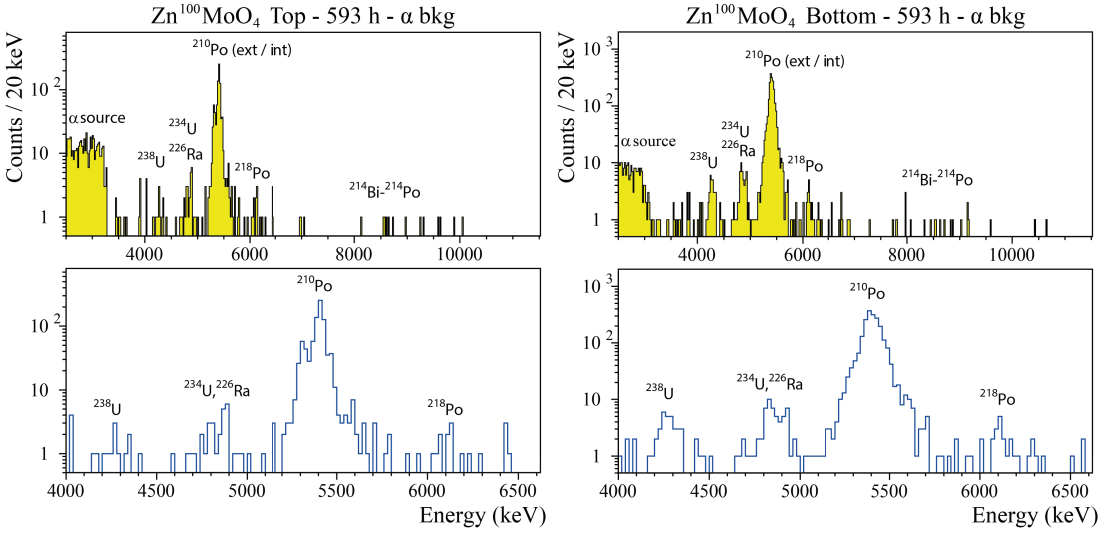

(A) (B)

FIGURE 6.34: (A) Alpha background for $Zn^{100}MoO_4$ top. (B) Alpha background for $Zn^{100}MoO_4$ bottom..

The energy resolution and the radioactive contaminants are worse in the bottom crystal; this evidence confirms our hypothesis of segregation of the impurities during the crystallization process. In fact this behavior has already been observed in $CdWO_4$ crystal scintillators [84].

TABLE 6.9: Summary of the activity of radionuclides measured for the $Zn^{100}MoO_4$ top and bottom crystals.

detector	Activity [mBq/kg]			
	^{232}Th	^{228}Th	^{238}U	^{234}U
$Zn^{100}MoO_4$ top	$\leqslant$0.008	$\leqslant$0.008	0.010±0.004	0.011±0.006
$Zn^{100}MoO_4$ bottom	$\leqslant$0.009	$\leqslant$0.021	0.039±0.007	0.04±0.01
detector	Activity [mBq/kg]			
	^{230}Th	^{226}Ra	^{210}Po	^{235}U
$Zn^{100}MoO_4$ top	$\leqslant$0.017	0.014±0.003	0.81±0.03	$\leqslant$0.013
$Zn^{100}MoO_4$ bottom	$\leqslant$0.024	0.023±0.004	2.39±0.05	$\leqslant$0.019

TABLE 6.10: Performance obtained with two big $Zn^{100}MoO_4$ crystals working as scintillating bolometers.

	13mK	
Parameter	Top 379 g	Bottom 382 g
Sensitivity μV/MeV	73	39
Baseline FWHM	1.7	0.9
1461 keV FWHM	7±1	15±2
2516 keV FWHM	10±2	13±5
$LY_{\gamma/\beta}$ kev/MeV	1.32	1.2
τ_r	6.4	9.6
τ_d	18	37

6.5.4 Conclusion

We have demonstrated that the scintillating bolometers made by $Zn^{100}MoO_4$ have an impressive energy resolution and exhibit a full α particle identification, which is the dominant source of background in present bolometric experiments for $0\nu\beta\beta$. However, as discussed in sec:6.34b, there exist a few nuclei which are β emitter with a Q-value higher than 3034 keV; these decays can potentially contribute to the background, therefore they have to be kept at a low level. To estimate the background level in the ROI we have performed a Monte Carlo simulation with the internal contamination level found in the measurements described before [85]. We used the geometry and the detector size adopted in the EDELWEISS setup: a cylindrical shape crystals with a mass of 495 g and a size ofØ60 mm×40 mm. The simulation takes into account the contamination of the nearest material by the ^{238}U and ^{228}Th chain; the considered α rejection factor is 99.9%. A suppression of high energy β's with delayed coincidence by a factor 10^3 is assumed, this is possible silencing the detector for a time corresponding to ten half lifes after an alpha particle interaction. The result of the simulation is reported in tab:6.11.

The final background index due to radioactive contamination of the crystal and the surrounding material is $b \approx 4 \times 10^{-4} \frac{\text{cts}}{\text{keV}\times\text{kg}\times\text{y}}$. This background value is at the same level as the one considered in sec:1.5, which confirms the hypothesis considered in the first chapter.

6.6 The LUMINEU follow-up

Based on the successful results obtained within the LUMINEU project, we can now imagine a LUMINEU follow-up where a medium size experiment is realized as an intermediate step before a final next generation neutrinoless double beta decay experiment. As we did in chapter one (sec:1.5), we can estimate the sensitivity of this middle-size

Element	Radionuclide	Activity [μBq/kg]	background $\left[\frac{\text{cts}}{\text{keV}\times\text{kg}\times\text{y}}\right]$
$Zn^{100}MoO_4$	^{228}Th	10	8.6×10^{-6}
crystal	^{226}Ra	10	3.1×10^{-8}
bulk	^{56}Co	0.06	6.2×10^{-5}
	^{88}Y	0.3	6.3×10^{-7}
$Zn^{100}MoO_4$	^{232}Th	0.5	1.2×10^{-5}
surface	^{238}U	2.4	1.5×10^{-4}
Cu holder	^{228}Th	20	1.3×10^{-6}
	^{226}Ra	70	1.5×10^{-7}
	^{56}Co	0.2	6.6×10^{-5}
PTFE elements	^{228}Th	100	9.6×10^{-6}
	^{226}Ra	60	7.5×10^{-7}
Reflective	^{228}Th	100	7.5×10^{-5}
foil	^{226}Ra	60	2.1×10^{-5}
Total			$\sim4\times10^{-4}$

TABLE 6.11: Background estimation due to internal and external radioactivity in the ROI for an experiment based on $ZnMoO_4$ scintillating bolometers. The estimation is performed with a MC simulation using as inputs the results obtained with the measurement.

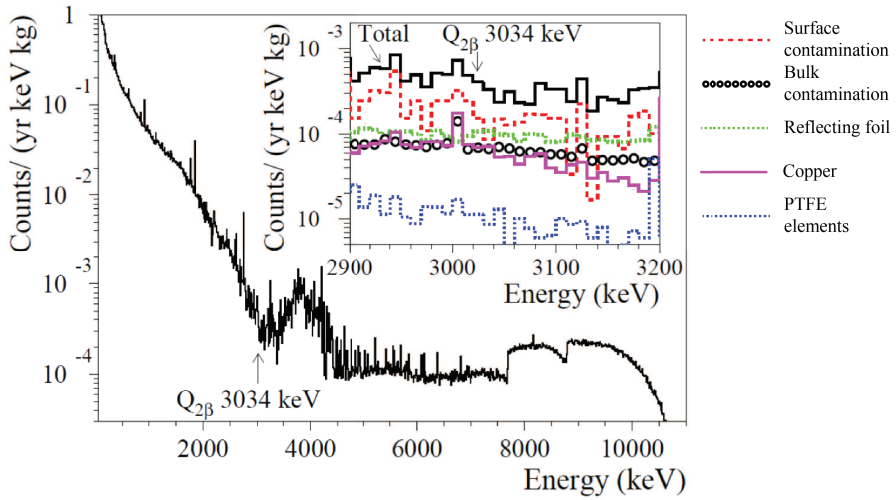

FIGURE 6.35: Background spectrum estimated with a MC simulation using as inputs the results obtained with the measurement.

experiment. Based on the obtained results we have to estimate the background. We will use the same assumptions considered in the MC simulation reported above: a cylindrical shape crystal with a mass 495 g and size Ø60 mm×40 mm. Let us assume a detector made by 20 scintillating bolometers based on the $Zn^{100}MoO_4$ crystal scintillator enriched in ^{100}Mo at 99%.
The total background will be:

- **Radioactive contamination:** the background due to internal and external contamination is estimated at the level of $\sim4\times10^{-4}$ $\frac{\text{cts}}{\text{keV}\times\text{kg}\times\text{y}}$. With this crystal size

the background index is:

$$b_p = 2 \times 10^{-4} \ \frac{\text{cts}}{\text{keV} \times \text{y} \times \text{crystal}} \tag{6.8}$$

- **Pileup of the $2\nu\beta\beta$:** it is demonstrated that the rejection of the pileup due to the $2\nu\beta\beta$ mode can be suppressed of a factor of 99.3% [51]. This value depends on the time response and the signal-to-noise ratio of the detector; the suppression factor is found with the underground data acquired during the tests at LSM. Anyway, let us be conservative and use the same consideration of sec:1.6. This time we will assume that a light detector with NL effect is used for this discrimination which lowers τ to 1 ms:

$$b_p = \left(\frac{ln(2) V \rho a N_A}{T^{2\nu}_{\frac{1}{2}} m_{mol}} \right)^2 \epsilon\tau = 1.8 \times 10^{-4} \ \frac{\text{cts}}{\text{keV} \times \text{y} \times \text{crystal}} \tag{6.9}$$

Using the procedure of the Neyman construction of confidence belts (appendix:A) with this background index the obtained sensitivity at 90% C.L. for the middle scale experiment is reported in tab:6.12. The middle scale experiment in this condition reaches the ∼0 background level so a lower background index will not improve substantially the sensitivity; the large experiment on the other hand can be improved decreasing the background rate by 1 order of magnitude; in this case it will be able to fully explore the inverted hierarchy region of the neutrino mass pattern.
During the next years an experiment based on a detector with 20 $Zn^{100}MoO_4$ scintillating bolometers would be one of the most sensitive experiments to the $0\nu\beta\beta$ half life.

Number of cristals	mass of ^{100}Mo kg	$T^{0\nu}_{\frac{1}{2}}$ Discovery [10^{25}y]	$m_{\beta\beta}$ Discovery [meV]	$T^{0\nu}_{\frac{1}{2}}$ Sensitivity [10^{25}y]	$m_{\beta\beta}$ Sensitivity [meV]
20	4.21	1.85	78–215	3.58	55–124
1000	210.1	23.65	21–60	47.77	15–42

TABLE 6.12: Sensitivity at 90% C.L. of experiments based on $ZnMoO_4$ scintillating bolometers searching for $0\nu\beta\beta$ of ^{100}Mo. The assumed background is discussed in the text. The live time is 5 y and the energy window is 10 keV.

Chapter 7

Li_2MoO_4: an alternative compound for scintillating bolometers

During the development of the LUMINEU technology in the crystal production chain, some tests to attempt to grow other molybdate compounds were performed. There are several inorganic crystal scintillators containing molybdenum (molybdates) that can be used in principle as a basic element for a scintillating bolometer embedding ^{100}Mo. In addition to $ZnMoO_4$ the most promising compounds – till now – are $CaMoO_4$, $CdMoO_4$ and $PbMoO_4$ but all of them are β emitters or even $\beta\beta$ emitters such as ^{116}Cd and ^{48}Ca. The Q-value of these processes is such that they populate with background counts the ROI for ^{100}Mo. We attempted then the Li_2MoO_4 option. During a test, large Li_2MoO_4 crystal boules were produced using the low thermal gradient Czochralski growth technique at NIIC. A deep purified powder of MoO_3 was used and it turned out that Li_2MoO_4 is relatively easy to grow and at the first attempt a big, beautiful and transparent crystal boule came out (fig:7.1). At present, only $CaMoO_4$ in the AMoRE experiment and $ZnMoO_4$ in the LUMINEU experiment have been proposed for a next generation $0\nu\beta\beta$ experiment. We believe that Li_2MoO_4 can be a a promising compound too and in the framework of LUMINEU we used the same facilities to test a scintillating bolometer based on lithium molybdate. Important advantages of Li_2MoO_4 in comparison to other molybdate crystal scintillators are the highest concentration of molybdenum (55.2% in weight), the absence of natural long-living radioactive isotopes, and the comparative easy crystalline growth. In addition Li_2MoO_4 scintillating bolometers are excellent instruments for neutron detection thanks to the exothermic ^{6}Li(n,t)α reaction (Q = 4.78 MeV).
In this chapter the characterization of the material in terms of optical and bolometric properties are presented; in particular the bolometric tests were made on three different large mass samples.

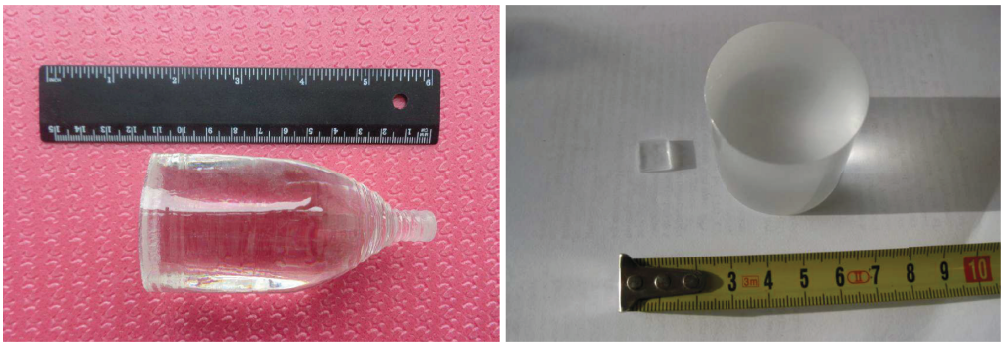

FIGURE 7.1: (LEFT) Li_2MoO_4 crystal boule. (RIGHT) Two elements were cut from the boule; one for luminescence measurements with a size of 10×10×2 mm^3, and one for bolometric tests with a size of Ø40 mm×40 mm

7.1 Li_2MoO_4 crystal production and characterization

The first test of Li_2MoO_4 as a scintillating bolometer was done on a small sample of 1.3 g in 2010 [86] and a bigger crystal of about 33 g was investigated later in an underground measurement [87]. The first measurement reports a contamination of the ^{40}K radioactive element at the level of ∼150 mBq/kg; a potassium contamination in this compound is expected due to the chemical affinity with lithium; this radioactive element is not so dangerous itself for the $0\nu\beta\beta$ searches. Anyway, if the rate is too large the probability of pileup with other energetic events becomes not negligible at the scale of 10^{-4} $\frac{\text{cts}}{\text{keV}\times\text{kg}\times\text{y}}$ and it should be kept under control. After the first crystal growth, other two large mass crystals were made and tested to evaluate the radio-purity of the various Li powder sources. In any case it was already proved that Li_2MoO_4 compounds are intrinsic radio-pure material [88].
The three high purity lithium carbonate (Li_2CO_3, 99.99%) powders used to synthesize the powder for the three samples, comes from different purification process not described here. The different samples are indicated as LMO1, LMO2 and LMO3. All the samples are been grown using the deep purified molybdenum oxide (MoO_3) and the low temperature gradient Czochralski method at NIIC. This prevents an intensive evaporation of molybdenum oxide from the melt; the losses of the initial material did not exceed the 0.5% level. Keeping the losses at the level of a few % is crucially important in view of the use of a costly enriched material. Optically clear defect-free Li_2MoO_4 crystals 25-55 mm in diameter and 70-100 mm in length with mass of 0.1-0.37 kg were grown. Two elements were cut from one of the boules (Fig:7.1.left); one, for luminescence measurements of 10×10×2 mm^3, and one for bolometric tests of Ø40 mm×40 mm (LMO1)[56], (Fig:7.1.right).

7.1.1 Optical measurements

A luminescent X-ray measurement on the sample with a size of 10×10×2 mm^3 was performed for scintillating characterization in the 8-290 K temperature range. The sample was irradiated by X-rays from a tube with a rhenium anode (20 kV, 20 mA). Light from the crystal was detected in the visible region by a FEU-106 photomultiplier (sensitive in the wide wavelength region of 350-820 nm) and in the near infrared region by a FEU-83

photomultiplier (with enhanced sensitivity in the near infrared wavelength region of 600-1200 nm, with cooled photocathode). The measurements were performed using a high transmission monochromator MDR-2 (with a diffraction grating 600 mm^{-1}). Emission spectra measured at temperatures of 8 K and 85 K, corrected for the spectral sensitivity of the registration system, are shown in fig:7.2.left. The most intensive emission band was observed in the spectra with maximum at ∼600 nm at the temperatures of 8 K and 85 K. The band at ∼400 nm is also observed at 8 K.

The dependence of the Li_2MoO_4 luminescence intensity on temperature was studied in the 8-290 K temperature interval. There is a large contribution of thermo-stimulated luminescence (TSL) to the X-ray stimulated luminescence, in spite of a relatively low heating rate. To avoid the effect of TSL, we have subtracted the TSL contribution assuming a linear dependence of the luminescence on temperature. The obtained curve is presented in fig:7.2.right. The luminescence intensity increases by a factor 2 at 8 K in comparison with that at 85 K, and by a factor of 5 in comparison with that at room temperature. The TSL curves obtained with the Li_2MoO_4 sample after irradiation at 8 K and at 85 K are presented in the inset of fig:7.2.right.

The long-term phosphorescence was measured at room temperature (293 K), at 8 K

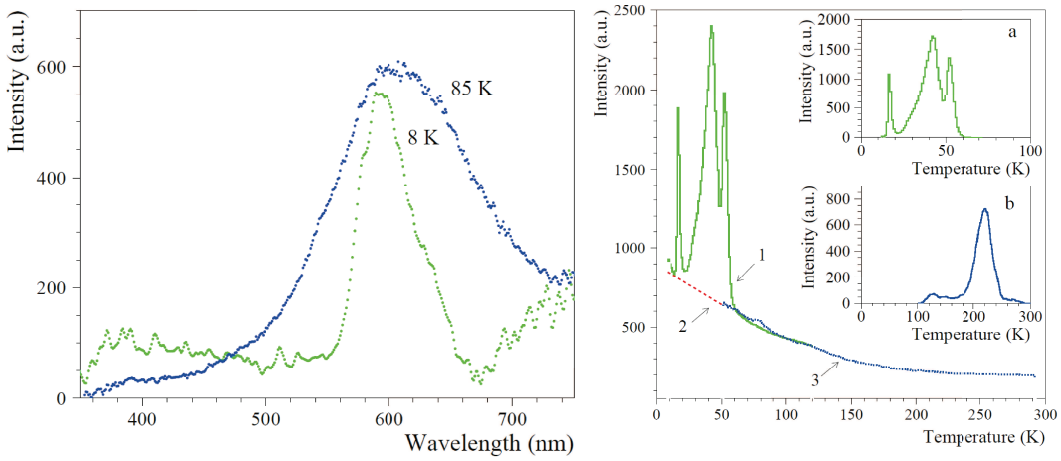

FIGURE 7.2: X-ray excitation luminescence measurement. (LEFT) Emission spectra at 85 K (blue dots) and 8 K (green dots). (RIGHT) Light emission intensity as a function of the temperature.

and 85 K. The phosphorescence decay curves can be approximated by the following hyperbolic function:

$$I = \frac{I_0}{(1+at)^{\alpha}} \tag{7.1}$$

where I is the phosphorescence intensity, I_0 is the phosphorescence intensity after the irradiation, a is a coefficient which depends on the nature and properties of the traps in the samples, α is the degree of the hyperbolic function. A fit of the decay curves with a hyperbolic function gives α=0.5, α=0.35 and α=0.23 for the phosphorescence after X-ray excitation at the temperatures of 8 K, 85 K and 293 K, respectively. We didn't perform a measurement on the optical absorption but the main wavelength contribution of scintillation light is around 600 nm, which corresponds to the orange colour; if an absorption at a specific wavelength range occurred the resulting medium would become coloured which is not the case. A confirmation of this hypothesis is given in [89] where a flat transmittance from UV to deep infrared light is shown.

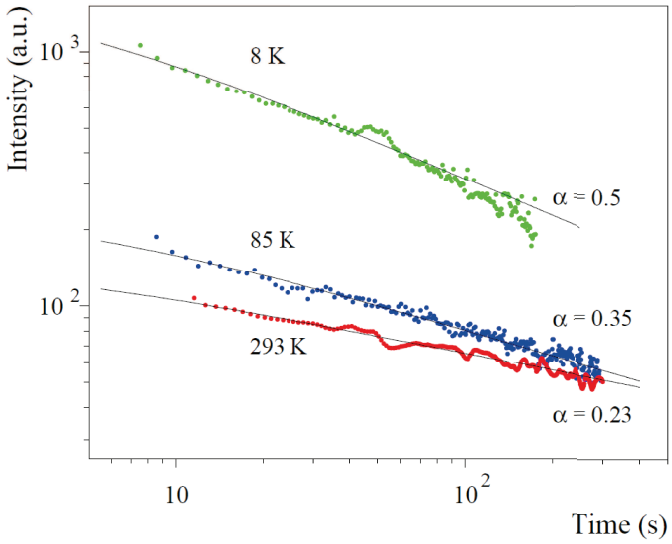

FIGURE 7.3: Long term phosphorescence light emission. The plot shows the intensity emission as a function of time for three different temperatures: 8 K (green); 85 K (blue); 293 K (red).

7.1.2 Aboveground bolometric characterization

The cylindrical crystal shown in fig:7.1, with a size of Ø40 mm×40 mm and a mass of approximately ∼150 g, was used to assemble a scintillating bolometer (fig:7.4). The crystal is held in a copper frame with six PTFE mechanical coupling pieces, and it is instrumented with a NTD Ge thermistor for the temperature read-out and a heater element for the signal-response stabilization. The choice of the light detector is very

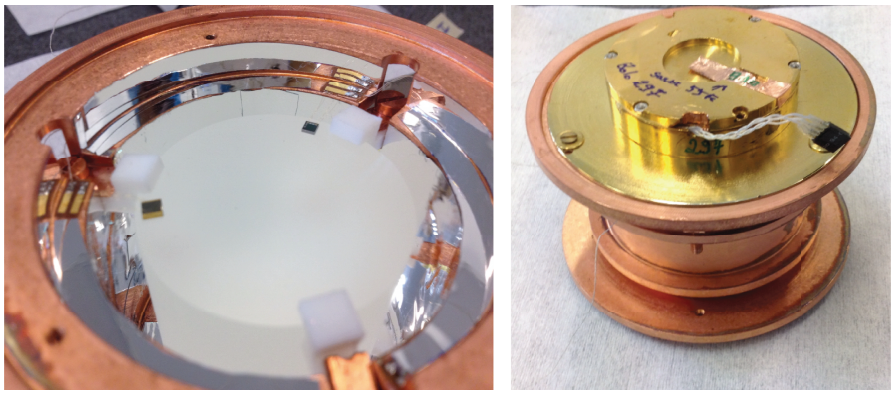

FIGURE 7.4: The Li_2MoO_4 scintillating bolometer detector. (LEFT) The Li_2MoO_4 crystal instrumented and fixed in the cavity. (RIGHT) The LD placed on the holder open side.

important, since the light yield of Li_2MoO_4 was expected to be extremely small [87]. We chose therefore a light detector with an advanced design, described in sec:5.2.2, exhibiting a remarkable signal-to-noise ratio.
The detector operated at three different temperatures with the copper holder stabilized at 15.2 mK, 15.5 mK and 16.5mK in the Ulisse cryostat at CSNSM. The data of the measurement at 15.2 and 16.5 mK were used in the data analysis corresponding to a total time of 118 h. The signals are processed with the optimum filter technique to optimize the signal-to-noise ratio. Given the excellent performances of this detector,

reported in tab:7.1, a very clear scatter plot and high quality energy spectra (fig:7.5 and fig:7.6) are produced even with such a large detector operating aboveground.

In the scatter plot three main structures appear with a clear band with a light yield of

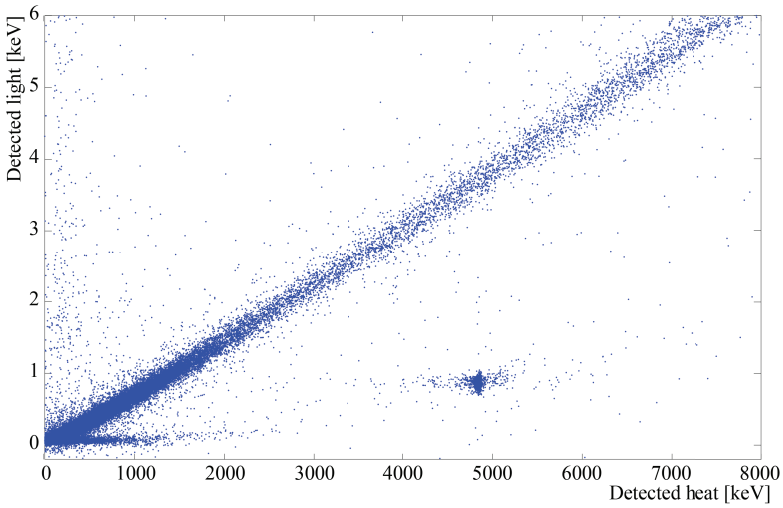

FIGURE 7.5: Scatter plot of the aboveground measurement whith LMO1

Parameter	Measured value
sensitivity	310μV/MeV
τ_r	10 ms
τ_d	75 ms
Bsl_{FWHM}	2.0±0.1 keV
FWHM ^{295}Pb @ 295 keV	4.4±0.4 keV
FWHM ^{214}Bi @ 609 keV	5.2±0.3 keV

TABLE 7.1: Performance obtained aboveground with LMO1 detector.

0.7 keV/MeV, which crosses, the plot and represents the β, γ and cosmic muons. This structure will be called β band. The LY is evaluated in an energy region around 3 MeV close to the energy of interest for the $0\nu\beta\beta$ decay; our measured LY – which does not take into account the light collection efficiency – is almost twice larger than the one reported in literature [87]. The second feature is a cluster of events with less emitted light with an energy close to 5 MeV. These events are due to neutron capture by ^{6}Li which has a large cross section for thermal neutrons (around 940 barns) and an isotopic abundance of 7.5%. The neutron capture is immediately followed by the disintegration of ^{7}Li in a α particle and a tritium nuclide (^{3}H) with a total energy of 4.78 MeV. Some α-triton events appear 0.24 MeV above the main peak: this effect is well known since a resonance absorption is possible on an excited level of ^{7}Li*. A spectum with these events is shown in fig:7.6.right. A less evident third structure appears as a low populated band till 2 MeV which has a much lower slope with respect to the β band. These events are due to nuclear recoils induced by fast neutrons. Finally, there are probably some alpha events below the β band; given the high interaction rate and the intrinsic radio-purity it is difficult to ascertain this but a hint of energy degraded α appears between $\sim$2 and $\sim$5 MeV.

Measurements on the internal contamination had to be performed in underground conditions. Not to increase more the interaction rate, no sources were placed for calibrations;

all the neutrons and γ's are due to the environmental radioactivity; the γ energy scale is calibrated with the ^{222}Rn radioactivity present in our laboratory.

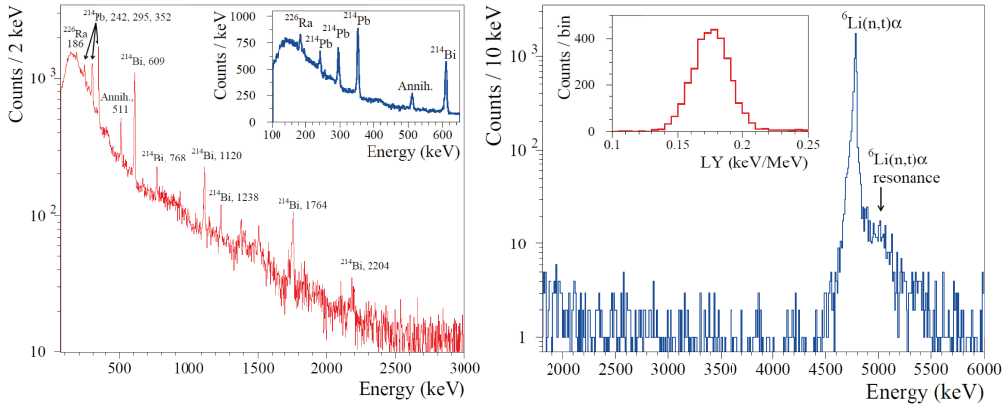

FIGURE 7.6: LMO1 energy spectra. (LEFT) The γ spectrum measured aboveground. (RIGHT) The spectrum of the α-triton reactions induced by the environmental neutrons.

7.2 Underground measurement

The LMO1 detector was the first moved underground in July 2014; the other two were mounted in winter and tested directly in the underground set-up in 2015. The bolometric performances of these detectors are very promising (sec:7.2.1-7.2.2-7.2.3). All of them were measured at the LNGS in the hall-C facility. All the data were acquired with a very narrow bandwidth, applying the Bessel filter with a cut-off frequency for the heat channel of 63 Hz for LMO1 and LMO2 and 16 Hz for LMO3, and for the light channel of 120 Hz for LMO2 and LMO3 and 200 Hz for LMO1. The $\gamma(\beta)$ energy calibration is made with a ^{232}Th source. From fig:7.7-fig:7.11-fig:7.13 one can appreciate an energy resolution below 10 keV FWHM at 2516 keV of the ^{208}Tl line for all the samples. These three cryogenic measurements demonstrate that the interest in Li_2MoO_4 as a compound for a bolometric research on $0\nu\beta\beta$ is well justified and further investigations are strongly recommended.

7.2.1 LMO1

The detector described in sec:7.1.2 was measured at a temperature of the order of ∼20 mK. A thorium calibration of 70 h to fix the $\gamma(\beta)$ energy scale was performed, and a neutron calibration of 20.5 h with a AmBe source was performed too. The result of the ^{232}Th calibration run is shown in fig:7.7: the good spectrometric performances are evident; all the γ peaks are recognisable and the energy resolution is ΔE_{FWHM} ≤3.5 keV even at high energy.

A long background measurement of 237 h was performed. From this measurement, the contamination of ^{40}K is evaluated from the gamma spectrum and the other contaminants from the α spectrum. The two bands were selected with the help of the light detector with a cut performed on the LY. An important contamination of ^{40}K is visible (fig:7.8.TOP) and a few counts in the α region are also visible (fig:7.8.BOTTOM),

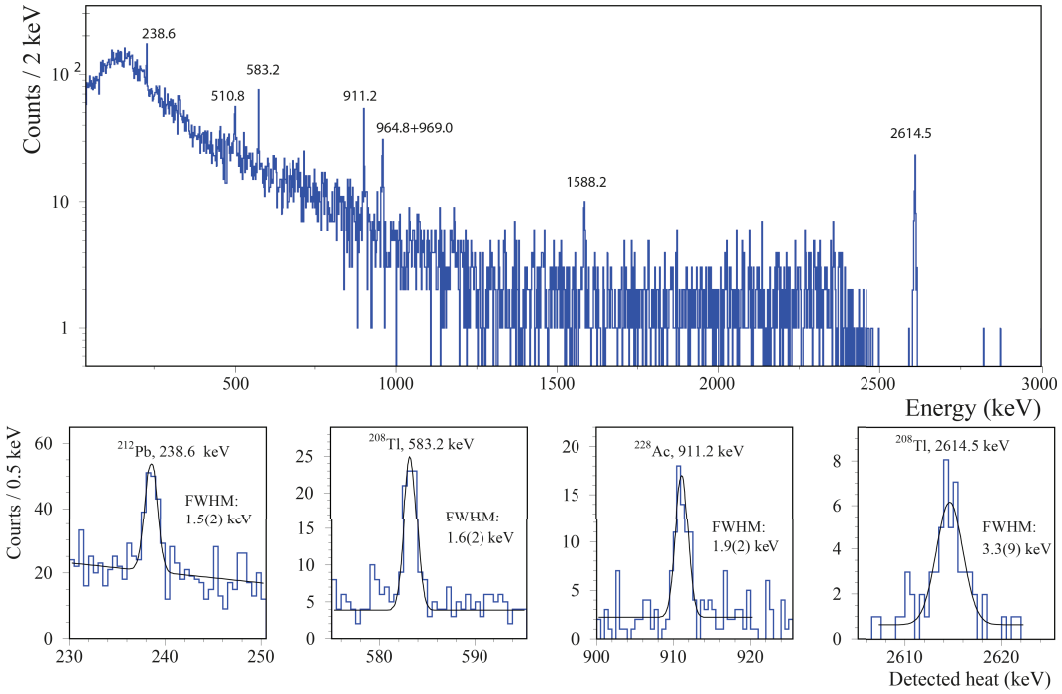

FIGURE 7.7: ^{232}Th calibration of LMO1. The insets below are detail of the measured γ's photo-peaks.

The contamination level is reported in tab:7.3. With the help of a high performance

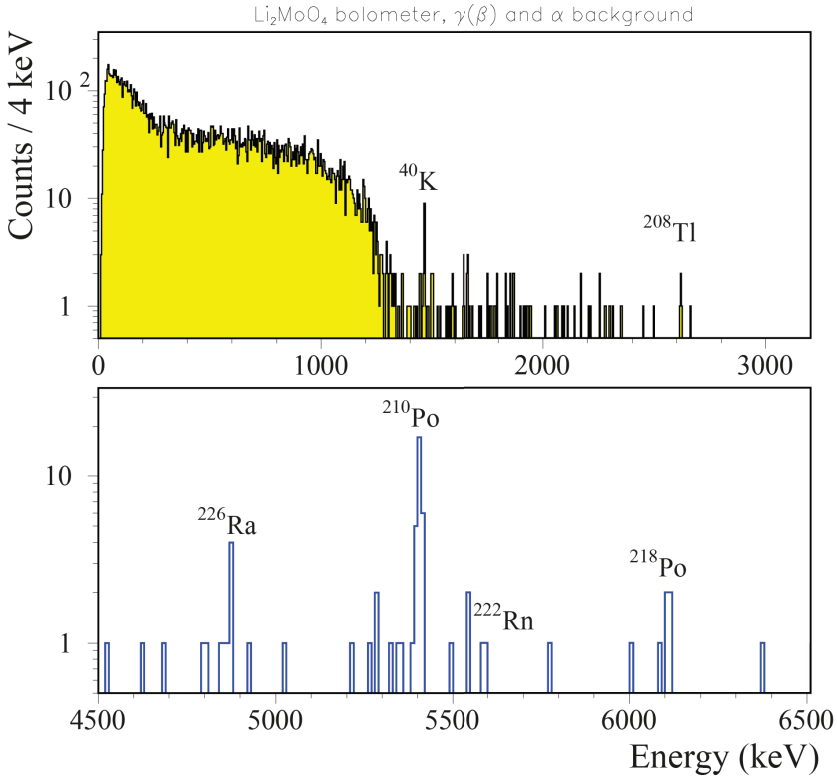

FIGURE 7.8: Background spectra of the LMO1 acquired underground during 237 h. (TOP) γ spectrum. (BOTTOM) α spectrum.

light detector, the different LYs are evaluated (tab:7.2): the discrimination power in the

ROI corresponds to DP=19±2σ, which is large enough for the complete separation of α events from the β band (fig:7.9). The measured QF for $\alpha/\gamma(\beta)$ is 0.21±0.01.

Band	Light Yield [keV/MeV]
$\gamma - \beta$	0.656±0.001
α-tritium	0.165±0.001
α	0.137±0.003
nuclear recoils	0.069±0.003

TABLE 7.2: Summary of LYs measured underground.

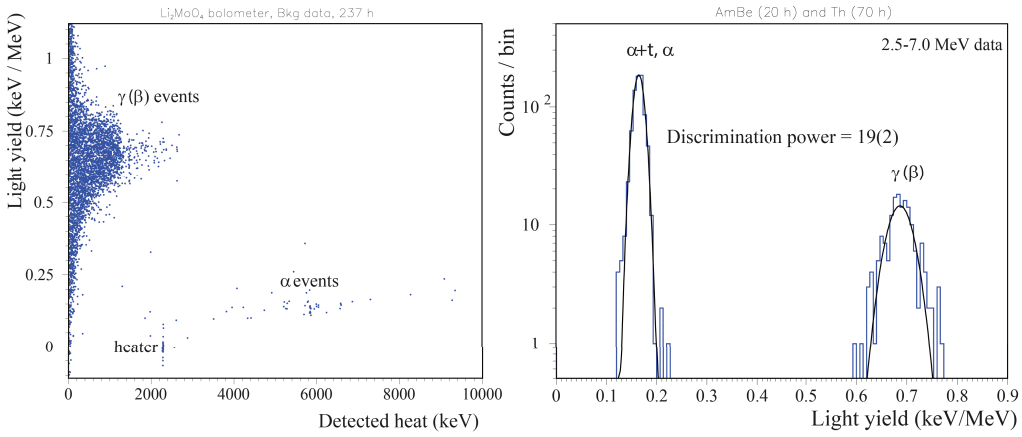

FIGURE 7.9: (LEFT) Q-Plot. (RIGHT) Histogram of the LY in the 2.5-7 MeV energy range.

7.2.2 LMO2

The Li_2MoO_4 crystal absorber has a size of Ø50×40 mm^3 and a mass of ∼241 g. This detector has the same structure of LMO1; the only difference is the reflector in the cavity. This time the internal surface was silver coated; the reflective film was deposited by electrolysis and subsequently polished. The light channel of LMO2 was an advanced light detector like the one described in sec:5.2.2 but with half the diameter. It was erroneously acquired with a 1 kHz sampling rate and a heavy Bessel filter with a frequency cut-off 120 Hz, while this detector shows fast signals of the order of τ_r ∼1ms; obviously its performances are deteriorated by the not optimized acquisition conditions. Nevertheless, the detector worked well and we got the information of interest. The detector was measured at ∼20 mK in the Hall-C facility at LNGS in summer 2015. A $\gamma(\beta)$ calibration measurement, with the ^{232}Th source, was done in periods which for a total time of ∼30 h. This second sample shows an energy resolution slightly lower than LMO1 but still remarkable: ΔE_{FWHM} ≤5 keV. Taking into account the larger mass and the not optimized working point, this detector appears very promising. Finally a long background measurement was performed for 135 h. Performing a cut on the light yield, the α and $\gamma(\beta)$ spectra have been separated for the radio-purity analysis. The background $\gamma(\beta)$ energy spectrum, reported in fig:7.12.LEFT, shows an internal contamination of ^{40}K much lower than the previous sample. On the other hand, from the α spectrum a major contamination in ^{226}Ra and other α emitters is clearly visible from fig:7.12.RIGHT. In the scatter plot the red dots correspond to α particles; in the energy range from ∼5

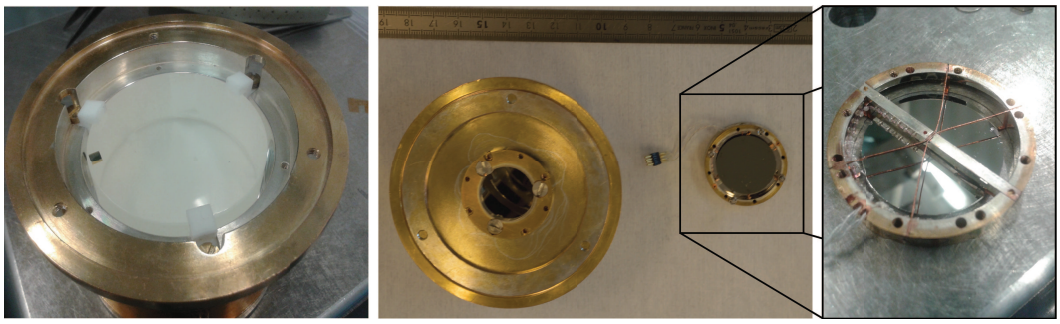

FIGURE 7.10: LMO2 detector. (LEFT) The Li_2MoO_4 crystal absorber. (RIGHT) The light detector.

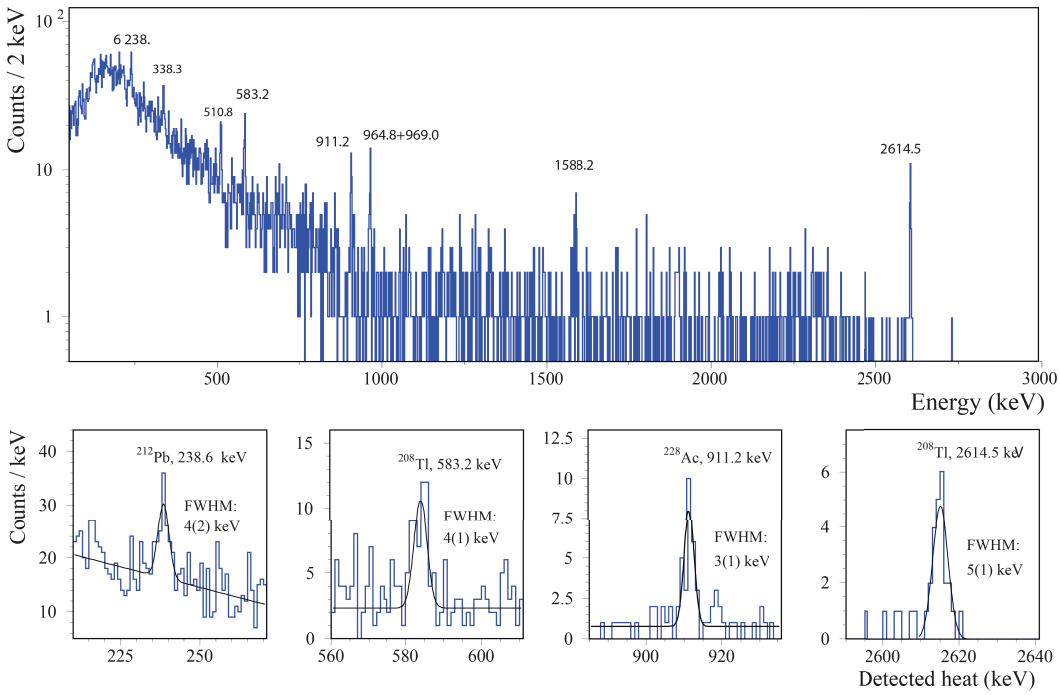

FIGURE 7.11: ^{232}Th calibration of LMO2. The insets below show details of the measured γ photo-peaks.

to ∼7 MeV a few characteristic lines are well visible. An evaluation of the activity of these contaminants is reported in tab:7.3. It is interesting to notice that the measured LYs are very small (fig:7.12.right), in fact, the light absorption is reduced by the smaller surface of the LD. Anyway, the good performance of this advanced light detector allows a full particle discrimination in spite of the small light collection efficiency.

7.2.3 LMO3

LMO3 detector was assembled in the usual way with an ordinary light detector. This time a smeared alpha source was placed in front of the absorber to populate the whole α band down to low energies and so demonstrate the effective discrimination power in all the energy range. A cut on the LY is then performed in the ^{232}Th calibration run. The $\gamma(\beta)$ calibration was collected in 30 h and the result is shown in fig:7.13. The energy resolution was equal to 7 keV at 2615 keV and less for the other γ lines. The energy

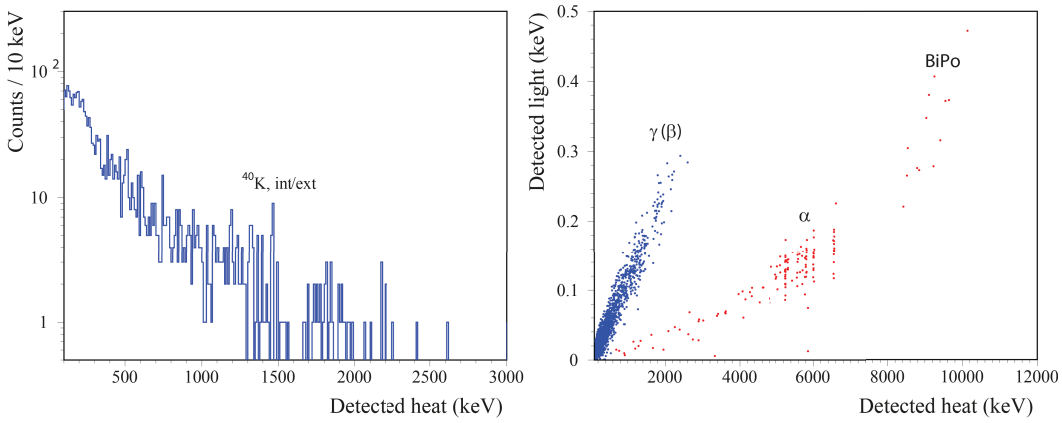

FIGURE 7.12: (LEFT) Background γ energy spectrum collected in ∼135 h. (RIGHT) Scatter plot.

resolution is the worst compared with the other two samples, LMO1 and LMO2, but still at the desired level for a large experiment.

The light detector facing the Li_2MoO_4 in this case was not an advanced one, so